Effect of Aggregate Type on Change in Properties of Concrete under Drying

（乾燥下にあるコンクリートの物性変化に及ぼす骨材種類の影響）

LIN, Mao

（林　懋）

Doctor of Engineering

Graduate school of Environmental Studies, Nagoya University

（名古屋大学大学院環境学研究科　博士（工学））

2018

Table of Contents

Chapter 1 Introduction

1.1 Background and motivation

The durability is gaining increasingly concern for the requirement of long service life in the design of concrete structures. The establishment of predictive performance assessment methods is essential to enable the long-term use of concrete structures. A new phenomenon of change of structure performance against earthquake has gained fresh attention recently. It has been reported that many reinforced concrete structures showed decrease of natural frequency after construction even in the case of nuclear plant which consists of thick concrete walls [1-3]. The reduction of natural frequency is attributed to the stiffness reduction of concrete structure.

All concrete structures are inevitable under drying in ambient environment. Due to the different volume change of aggregate and harden cement paste under drying, the shrinkage of harden cement paste is restrained by aggregate, and micro-cracking is produced. Micro-cracking could lead to the reduction of Young's modulus of concrete. It is reported that Young's modulus of concrete generally decreased during drying [4]. The Young's modulus of concrete using limestone as coarse aggregate which was dried to equilibrium state under the humidity of 40%RH at room temperature was decreased to 65% that of saturated state. Of course, the reduction of Young's modulus of concrete could result in the stiffness reduction of concrete structure.

As component of reinforced concrete members, concrete is always restrained by rebar or outer member. When the shrinkage of concrete due to drying is restrained, stress occurs. Because the cracking strength of mortar is only several MPa, crack is easily produced. These cracks could be visible and localized sometimes. The shrinkage induced cracks could reduce the stiffness of reinforced concrete member. Therefore, it should be properly predicted for aging management of concrete structures.

In the present durability design [10], action of carbonation, chloride, frost, alkali-silica action, and chemical corrosion are mainly focused on, but the effect of drying is not focused on. The deterioration of concrete structures includes: 1) Rebar corrosion caused by carbonation and chloride; 2) Cracking and strength decline caused by frost, alkali-silica action, and chemical corrosion.

In 'Recommendations for practice of crack control in reinforced concrete buildings (design and construction)' [11], the allowable crack width for different purpose is proposed. For example, less than 0.3mm for resistance of yield of rebar, and less than 0.1mm for water leak.

The guideline considers the humidity and type of aggregate in the prediction of shrinkage strain. Concrete using limestone as coarse aggregate has less shrinkage strain. But the guideline does not consider the impact of drying condition on Young's modulus, compressive strength and tensile strength.

For prediction of concrete properties, the Young's modulus is function of compressive strength.

$$E(t) = 3.35 \times 10^4 \times k_1 \times k_2 \times \left(\frac{\gamma}{2.4}\right) \times \left(\frac{f_c(t)}{60}\right)^{1/3} \quad (1.1)$$

The equation incorporates the effect of aggregate. For limestone, k_1=1.2, for sandstone, k_1=1.0.

Splitting tensile strength is also expressed as a function of compressive strength:

$$f_t(t) = 0.291 f_c(t)^{0.637} \quad (1.2)$$

And the cracking strength is:

$$f_{cr}(t) = f_t(t) \times \kappa \quad (1.3)$$

where κ is reduction coefficient.

But such cracking is used only for evaluation of risk of durability whose deterioration mechanisms are specified above.

According to 'Standard for Seismic Evaluation of Existing Reinforced Concrete Buildings' [12], structural cracking and aging is considered by the way of Time index *T*. The time index *T* evaluates the effects of the structural defects on the seismic performance of a structure, and it implicitly indicates the performance of construction, shrinkage-induced deterioration (rebar corrosion and reduction of rebar section), and apparent concrete strength change due to cracking. But there is no clear background data to evaluate the index *T* as a function of material deterioration.

In the calculation of strength index *C*, specified design strength of concrete *Fc* is used as compressive strength of concrete. Compressive strength of concrete is also a key parameter in the calculation of ductility index.

As used for seismic evaluation, compressive strength can be obtained by core sampling. Principally, the core samples are obtained from main structural elements, such as wall, beam, and floor. The concrete core tests proposed by three different guidelines [12] [13] [14] are summarized Table 1.1.

Generally, Young's modulus of concrete of target structure is calculated based on Eq. (1.1). As previously reported [4], compressive strength of concrete does not decrease uniformly with drying, and it is influenced by the physical properties of the cement paste and the damage caused by volumetric change during drying of the paste and aggregate. In contrast, the Young's modulus shows a monotonic decrease under drying. Therefore, Young's modulus should be determined separately.

Table 1.1 Concrete core test

	The Japan Building Disaster Prevention Association [12]	Tokyo association of architectural firms [13]	Japan Association for Building Research promotion [14]
Number of core sampling for compressive strength	Three or more samples for each story at each construction stage	Three or more samples for each story at each construction stage	Three or more samples for each story at each construction stage
Testing method	JIS A1107	JIS A1107	JIS A 1107
Compressive test site	Public institution・university lab		
Diameter	100 mm (minimum 50 mm)	100 mm （minimum 50 mm）	100 mm （minimum 50 mm）
Height	200mm （minimum 100mm）	200mm （minimum 100mm）	In case of diameter of core < 75mm, length is more than twice of diameter
Calculation method of compressive strength	Average：$X_{mean} = (X_1 + X1\cdots+Xn/n$ Standard deviation： σ $= \sqrt{\left(\sum (X_i - X_{mean})^2 /(n-1)\right)}$ Estimated strength： $\sigma_B = X_{mean} - (\sigma/2)$	Estimated strength： $\sigma_B = X_{mean} - \sigma/2$ X_{mean}：Average of test results from 3 core samples and above σ：Standard deviation of test results from 3 core samples and above	In case of $\sigma_{B2} \geqq F_c$：$\sigma_{BD}=\sigma_{B2}$ In case of $\sigma_{B1} \geqq F_c > \sigma_{B2}$: $\sigma_{BD}=F_c$ In case of $\sigma_{B1} < F_c$: $\sigma_{BD}=\sigma_{B1}$ F_c: Specified design strength of concrete (N/mm^2) σ_{BD}: concrete strength for diagnosis (N/mm^2) $\sigma_{B1}=X_{mean}-\sigma/2$ $\sigma_{B2}=X_{mean}-\sigma$ X_{mean}: Average of compressive strength of concrete core at each story (N/mm^2) σ: Standard deviation （$\sigma \geqq 2.5$N/mm^2）
Limit of compressive strength	$\sigma_{BD}=X_{mean}-\sigma/2$ 13.5 N/mm$^2 \leqq \sigma_B \leqq 1.25F_c$ and 30 N/mm^2 $\sigma_{BD}=X_{mean}-\sigma$ 13.5 N/mm^2 and $0.75F_c \leqq X_{mean}$	$\sigma_B \leqq 1.25F_c$ （In the case of one sample per story, $1.0F_c$）	$\sigma_{BD} \leqq 1.5F_c$ and $\sigma_{BD} \leqq$ 36N/mm^2 $\sigma_{BD} \geqq$ 9 N/mm^2
Compressive strength of lightweight concrete		Reduction of ultimate shear strength Q_{su} $Q_{su} = \alpha \cdot Q_{su}'$ α＝0.9 (1・2 type), α＝0.8 (3・4 type）	
Over limit of compressive strength	Re-investigation・not applicable	Re-investigation・not applicable	Re-investigation・not applicable
Number of core sampling in carbonation test	Three or more samples for each story at each construction stage	Three or more samples for each story at each construction stage	Three or more samples for each story at each construction stage
Carbonation Test approach	Cutting of core sample Maximum size of Specimens	Cutting surface of compressive test specimen	Cutting surface of compressive test specimen

For the prediction of the performance of concrete structures, tensile strength as cracking strength is also a key parameter. And it is assessed by splitting tensile test. Previous studies had pointed out that the splitting tensile strength also changes under drying [5-7]. As a design strength,

splitting tensile strength is often expressed as a function of compressive strength [11]. This relationship is valid at saturated state but not after drying. In addition, as the determination mechanism of strength has multi factors, it is unlikely that there is strong correlation between compressive strength and tensile strength. Therefore, tensile strength should be evaluated separately, too.

Because the behavior of moisture transport determines the shrinkage strain in concrete, it is one of the key parameters for the time-dependent prediction of performance of concrete structure.

As the strength is affected by damage caused by volumetric change during drying of the paste and aggregate, so the aggregate property is a key parameter, which is not considered in the present guideline [11]. Furthermore, it has been reported that different coarse aggregate leads to different numbers of through cracks and surface cracking in concrete under restraint condition [8][9]. Through cracking has much impact on durability [10]. The cracking pattern of concrete is important. Therefore, the knowledge of aggregate properties is needed for predicting structural performance change under drying.

1.2 Objectives and scope

To predict the structural performance change due to drying for the long-term use of concrete structures, the behavior of moisture transfer, splitting tensile strength change due to drying, and shrinkage induced cracking under restraint condition should be investigated. In this study, the influence of aggregate properties is focused on. The main work of this study consists of the following three parts.

1) Moisture transport

Shrinkage strain is directly determined by moisture transport. In this study, the effects of temperature and aggregate size on water diffusion coefficient are focused on, and the reproduction and comparison of the existing research are discussed. Drying experiments of both mortar and concrete specimens have been conducted to evaluate moisture transport behavior in cement based material. Boltzmann-Matano method is applied to the experimental data to calculate the water diffusion coefficient. Temperature dependency of water diffusion coefficient and effect of aggregate size on water diffusion coefficient are experimentally evaluated. This research is necessary for time-dependent structural change, because the rate of deterioration is a function of moisture transport. For the long-term use of concrete, understanding of moisture transport is required.

2) Splitting tensile strength

The influence of drying on splitting tensile strength is investigated. This study aim to clarify the mechanism through experiments using control mortar specimen and concrete specimens with two types of coarse aggregate of different shrinkage behavior mixed with the control mortar. Limestone, which is characterized by little shrinkage, and sandstone, which is characterized by

large shrinkage, is used as coarse aggregate to assess the impact of micro-damage around aggregate during drying. Specimens were shaped in a thin plate for a faster equilibrium with the ambient drying conditions. The specimens were dried at the constant temperature of 20 ℃ and various humidity of 95% RH ~ 20% RH, and were also heated up to 90 ℃. Drying was maintained till the mass of specimens become constant. Then changes in length and mass from the saturated state and splitting tensile strength were determined.

3) Shrinkage-induced cracking development in restrained concrete

For the purpose of better understanding material characteristics, in addition to through-cracking, the initiation of cracking and the propagation process at the meso-scale (scale from micrometer to millimeter) is studied. Concrete specimens were prepared with the same mix proportion except for their constituent coarse aggregates, namely limestone and sandstone of which inherent drying shrinkage values are different from each other. Studying aggregate-dependent crack initiation can lead to a better understanding of cracking behavior and contribute to formulating mechanisms to control cracking. The strain at a cross section perpendicular to the drying direction under both unrestrained and restrained conditions was observed by a digital image correlation method (DICM). Because comparing the results of numerical simulations with experimental data is quite informative, rigid-body-spring networks (RBSN) is applied to reproduce trends of crack initiation and propagation in order to understand the impact of aggregate properties on these processes.

1.3 Organization of the thesis

This dissertation consists of six chapters; the contents of each chapter are listed as follows:

Chapter 1 introduces the background of performance change of concrete structures due to drying, clarifies the importance of this research, and illuminates the objectives and scope of this study.

Chapter 2 provides literature review on moisture transport phenomena in cement based material, concrete properties change under drying, experimental and numerical study regarding shrinkage induced cracking.

Chapter 3 provides experimental study on water diffusion coefficient of cement based material.

Chapter 4 provides the study of change in splitting tensile strength of concrete during drying or heating up to 90 ℃, and discusses the mechanism of that.

Chapter 5 provides both experimental and numerical studies on the shrinkage-induced cracking development in concrete under unrestrained and restrained conditions, and the role of aggregate properties is focused on.

Chapter 6 provides the general conclusions of this study.

References

1. T. Kashima, Y. Kitagawa, ‘Dynamic characteristics of building estimated from strong motion records using evolution strategy.’, Journal of structural and construction engineering, 602 (2006), 145-152 (in Japanese)
2. R. Toyobe, H. Kojima, J. Tobita, N. Fukuwa, ‘Long-term seismic response observation for evaluation of dynamic properties of low and medium-rise buildings.’, Tokai-shibu Kenkyu Houkokusyu, 51 (2013), 177-180 (in Japanese)
3. Nuclear and Industrial Safety Agency, ‘Numerical simulation of seismic response of buildings.’, Tohoku Electric Power Co., Inc. Onagawa Nuclear Plant 2 and 3., Building/Structure, 2011, Tokyo, 4-3-1
4. I. Maruyama, H. Sasano, Y. Nishioka and G. Igarashi, “Strength and Young's modulus change in concrete due to long-term drying and heating up to 90 ℃.” Cement and Concrete Research, 66 (2014), 48-63.
5. J.A. Hansen, “Effects of curing and drying environments on splitting tensile strength of concrete.” Journal of the American Concrete Institute 65 (1968), 535-543.
6. K. Kishitani, H. Kasami, F. Oshida and t. Okuno. “Properties of concrete exposed to 20～300℃, Part 1 and 2.” Summaries of technical papers of Annual Meeting Architectural Institute of Japan, Structure 57 (1982), 317-320 (in Japanese)
7. T. Kanda, Y. Ichikawa, O. Kontani, M. Takeda and K. Otsuka. “Experimental investigation of concrete damaged by exposuring to high temperature and low humidity environment.” Journal of structural and construction engineering (615), 2007, 15-22 (in Japanese)
8. Y. Mitani, M. Tanimura, I. Maruyama, Shrinkage cracking characteristics of concrete using shrinkage reducing agent, in: AIJ (Ed.) Summaries of technical papers of annual meeting, Sapporo, Japan, 2013, pp. 41-42 (in Japanese)
9. Y. Mitani, Y. Ishii, M. Tanimura, I. Maruyama, Quantitative evaluation on reduction effect of drying shrinkage cracks by expansive additive, in: AIJ (Ed.) Summaries of technical papers of annual meeting, Nagoya, Japan, 2012, pp. 747-748 (in Japanese)
10. ‘Recommendations for durability design and construction practice of reinforced concrete’, Architecture Institute of Japan, 2004.3
11. ‘Recommendations for practice of crack control in reinforced concrete buildings (design and construction)’, Architecture Institute of Japan, 2006.2
12. ‘Standard for Seismic Evaluation of Existing Reinforced Concrete Buildings’, The Japan Building Disaster Prevention Association, 2017
13. ‘Technical manual for seismic evaluation of seismic resistance of buildings along the emergency transport route in Tokyo’, Tokyo association of architectural firms, 2017

14. ‘Technical Manual for Seismic Evaluation and Seismic Retrofit of Existing Reinforced Concrete Buildings’, Japan association for building research promotion, 2012

Chapter 1

Chapter 2 Literature Review

2.1 Water movement phenomena in cement based material

Water movement in concrete has been studied relating to drying shrinkage and creep [1]. Volume change of concrete, e.g. drying shrinkage and autogenous shrinkage arising from water evaporation and hydration, induces cracking. Accordingly, quantitative evaluation of water movement is vital to assess autogenous shrinkage and drying shrinkage.

Experimental study of water movement is firstly developed by Sakata [2], with Boltzmann-Matano method adopted to obtain the relation between water diffusion coefficient and water content. The water movement phenomenon in concrete is difficult as it consumes much time to realize equilibrium than those of other porous materials. Accordingly, Boltzmann-Matano method, compared with other methods, has a benefit regarding to cement based material research. The flow of Boltzmann-Matano method is explained in Section 2.1.2. The diffusion coefficient of water is indicated to be dependent on the water content with Bazant's numerical approach [3].

Followed by Sakata's research, comprehensive research was performed by Akita and Fujiwara on water movement [4] [5] [6]. They applied different approaches to attain the relationship between water diffusion coefficient and water content (or relative water content), and obtained results consistent to those by Sakata. In addition to the foregoing results, they found the temperature dependency of water diffusion coefficient, water diffusion coefficient in very low water content region, and water diffusion coefficient of desorption and adsorption processes.

2.1.1 Water distribution in one-dimensional drying

Fig. 2.1 presents the water content variation related to time in concrete specimens from Sakata [2]. The experiments were performed at 20℃ and of 60% RH as humidity constantly. The Water cement ratio was 50%. Following this figure, water content is drastically varied at x=2cm approaching to the drying surface, whereas it varies slowly deeper inside. Drying experiments of concrete were performed by Akita [7] with the identical W/C=50% under the identical drying atmosphere of 20℃ and 60% RH to Sakata, and they attained the similar tendency as presented in Fig. 2.2.

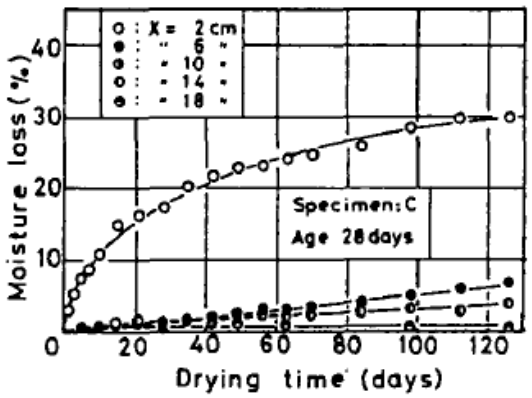

Fig. 2.1 Moisture loss at depth x from the drying surface of concrete specimens (Sakata [2])

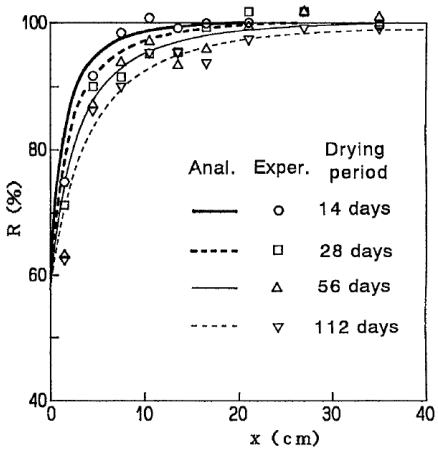

Fig. 2.2 Profiles of relative water content for one-face drying of concrete specimens (Akita [7])

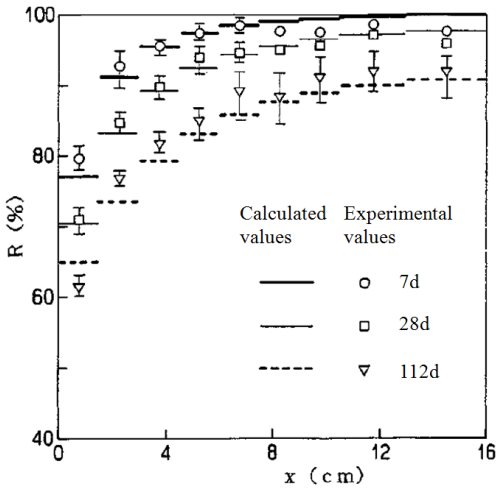

Fig. 2.3 Relative water content distribution of mortar specimens. Error bars of 1-sigma of measured variation are shown. (Akita [4])

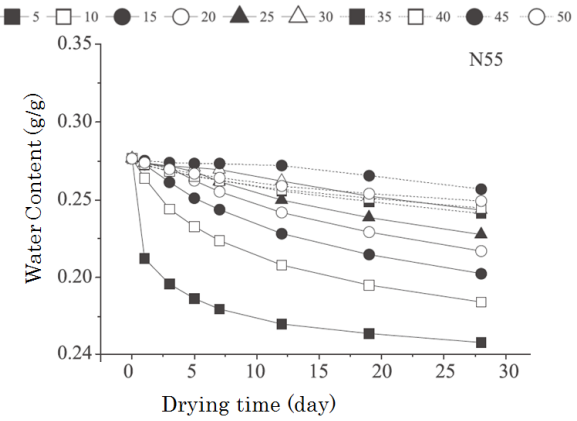

Fig. 2.4 Water content change at different depth from drying surface of cement paste (Maruyama [8])

The drying experiment was also performed by Akita on mortar specimens [4]. The water cement ratio was 53%, and the mortar specimens were dried at 20℃ and 60% RH as humidity constantly. The relative water content distribution is presented in Fig. 2.3. Evidently, the drying process is fast near the drying surface and slows down as the distance increases from the drying surface.

The drying test was performed by Maruyama et al. [8] on cement paste specimens. The drying condition refers to the constant temperature of 20℃ and humidity of 60% RH. Fig. 2.4 presents the water content variations of specimens with W/C=55%. The water distribution tendency is similar to concrete and mortar experiments by Sakata and Akita [2, 4, 7]. The water loss is most drastic at the depth

of 5mm from the drying surface, and gradually slow down to the depth of 50mm.

2.1.2 Calculation of water diffusion coefficient

The diffusion coefficient of water can be attained from experimental data of moisture content by Boltzmann's transformation, as indicated by Sakata [2]. The one-dimensional drying is considered abiding by the one-dimensional diffusion equation.

The one-dimensional diffusion equation is presented below:

$$\frac{\partial w}{\partial \mathrm{t}} = \frac{\partial}{\partial x}\left(D\frac{\partial w}{\partial x} \right) \tag{2.1}$$

After Boltzmann transformation:

$$\lambda = \frac{x}{\sqrt{t}} \tag{2.2}$$

Eq. (2.1) turns:

$$D(w) = -\frac{1}{2}\int_{w_0}^{w} \lambda dw / \frac{\partial w}{\partial \lambda} \tag{2.3}$$

where λ : Boltzmann variable ($m/s^{1/2}$)

x : distance from drying surface (m)

t : drying time (s)

w_0 : saturated water content (g/m^3)

w : water content at any time (g/m^3)

The relationship between relative water content ($R=w/w_0$) and Boltzmann variable λ is presented in Figs. 2.5~2.7 from Sakata [2], Akita [4] and Park [9], respectively. Such relationship is determined by Sakata following the mass changes of specimens with various lengths, while Akita and Park determine it by cutting the specimens after drying. Accordingly, they adopt different fitting functions as follows:

$$\text{Sakata：}\quad R = 100 \cdot \left\{ 1 - \left(\frac{a-\lambda}{b} \right)^n \right\} \tag{2.4}$$

$$\text{Akita：}\quad R = 100 \cdot \left\{ 1 + f - \frac{a}{(\lambda/2+b)^2} \right\} \tag{2.5}$$

$$\text{Park：}\quad R = 100 \cdot \left\{ 1 - \frac{a}{(\lambda+b)^2} \right\} \tag{2.6}$$

where a, b, and f are constants determined by the fitting curves.

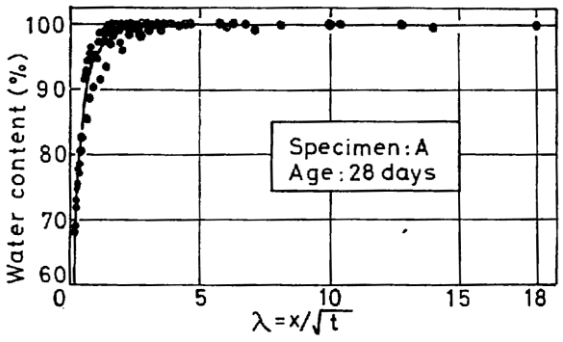

Fig. 2.5 Relationship between Relative water content (R) and λ (Sakata [2])

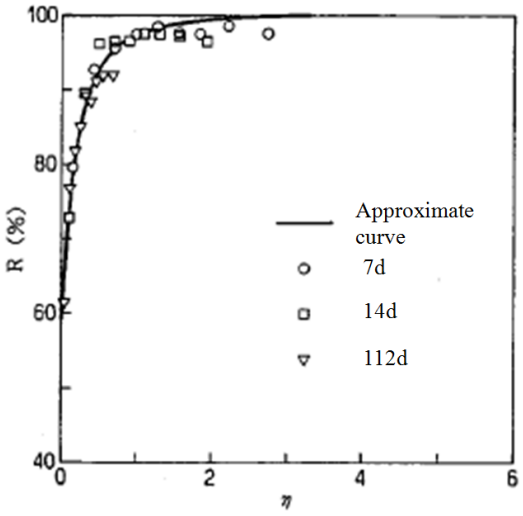

Fig. 2.6 Relationship between R and 0.5λ (Akita [4])

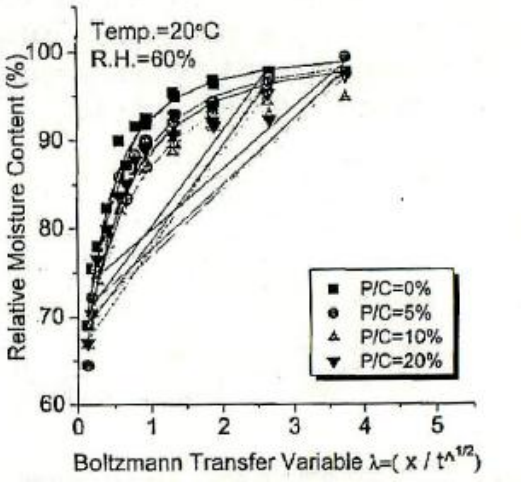

Fig. 2.7 Relationship between R and λ (Park [9])

After the constants in the fitting functions are determined, the above equations are substituted into Eq. (2.3), and diffusion coefficient of water D is calculated. Figs. 2.8~2.10 show the relationship between D and relative water content (R). They all regard water content as the potential of water movement. As those figures indicate, moisture diffusion inside concrete is strongly related to the water content of the concrete. More precisely, the water diffusion coefficient in the range of high water content declines drastically as moisture content decreases, whereas in the range of water content below 80%, the rate of decline of diffusion coefficient slow down. The relationship between D and R is Non-linear.

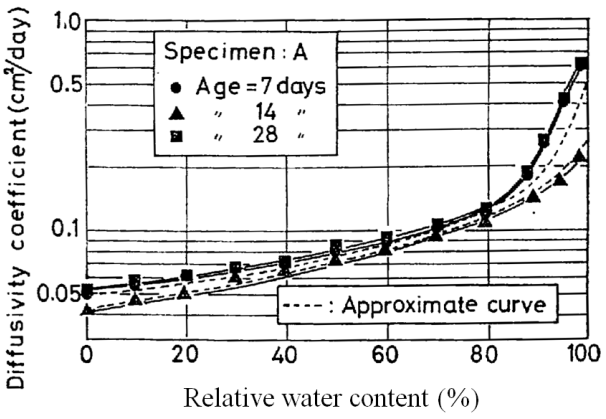

Fig. 2.8 Relationship between D and R (Sakata [2])

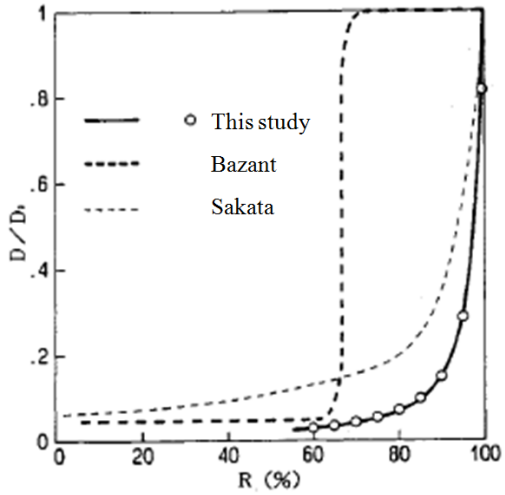

Fig. 2.9 Relationship between D/D1 and R (Akita [4])

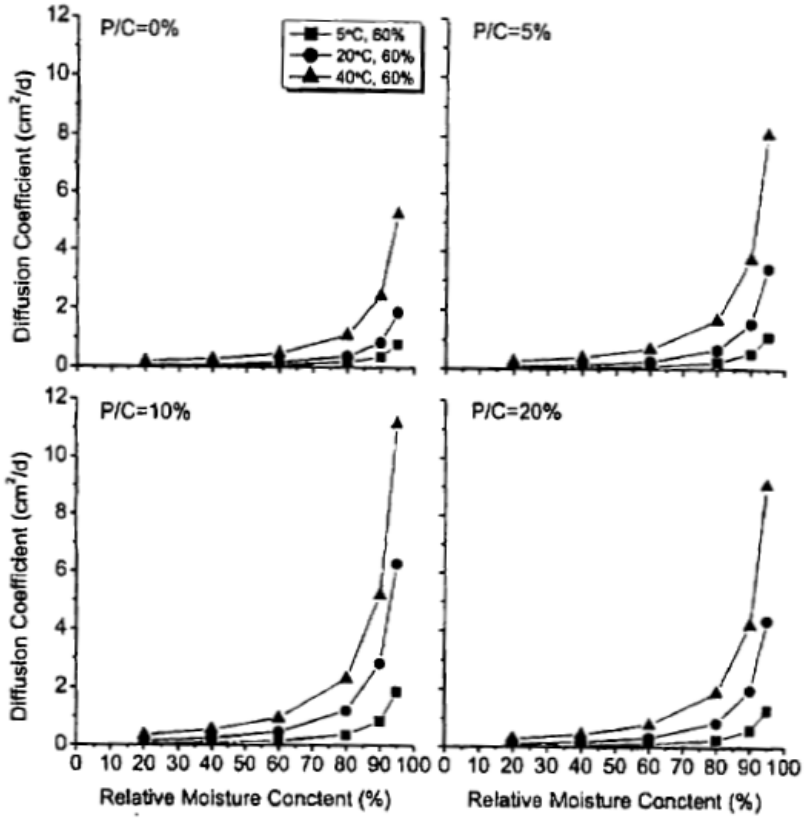

Fig. 2.10 Relationship between D and R (Park [7])

2.1.3 Experimental methods of water movement

Fujiwara [5] compared three experimental methods of water movement as presented in Fig. 2.11:

1) Pre-cutting

The specimen is firstly cut into several segments before drying. Those segments are then combined again for drying. The mass of each segment is measured over time. In the end of the drying experiment, those segments are dried to attain their absolute dry weight. In this way, the water distribution at different drying time could be calculated.

2) Cutting after drying

The specimen is cut after drying at the specified day, and the mass of each segment is immediately measured. After that, those segments are dried in furnace to absolute dry state. The water distribution can be obtained based on the difference in mass before and after heating.

3) Using specimens with different length [2].

Water distribution is based on mass changes of specimens with various lengths.

The water content distributions with diverse experimental approaches are presented in Fig. 2. 12. The second method cutting after drying is treated as the most reliable and direct approach for water movement experiment. Yet this method demands specimens in considerable amount. Precutting takes on a little lower speed of drying, whereas the tendency of water content distribution from the drying surface is basically the same. Furthermore, the cutting surface exerts very small impact on water movement inside concrete specimens.

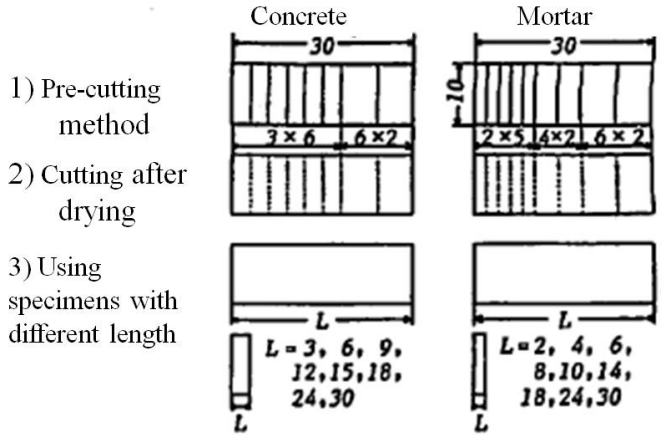

Fig. 2.11 Water movement experimental specimens (Fujiwara [5])

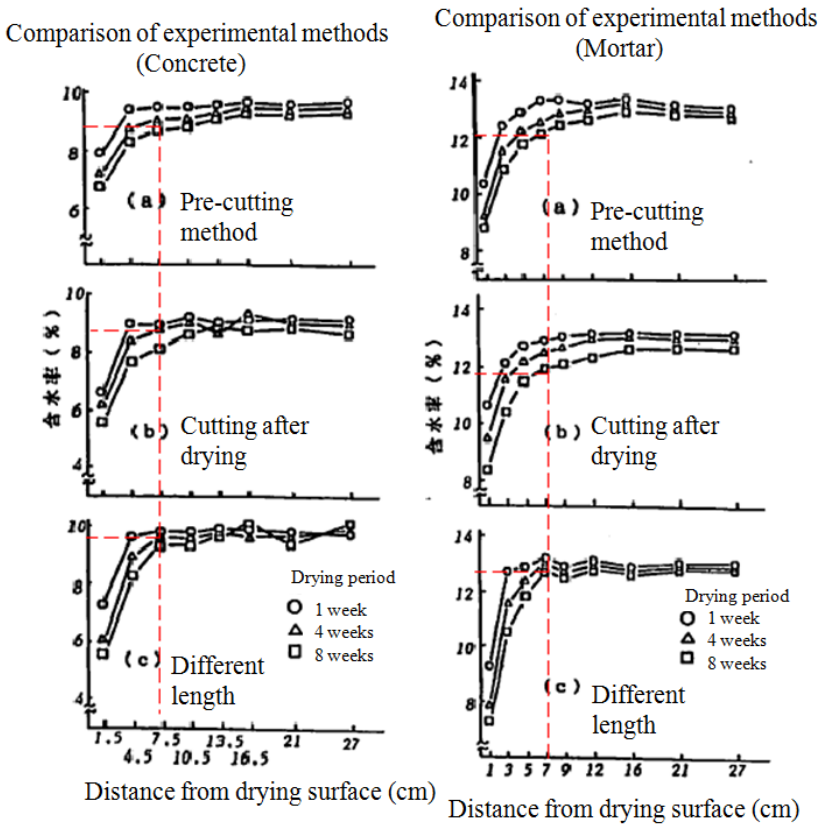

Fig. 2.12 Water content distribution obtained by different methods (Fujiwara [5])

2.1.4 Temperature Dependency of Water Diffusion Coefficient

Fujiwara [6] conducted drying experiments of concrete under various temperatures, and they found the diffusion coefficient of water is dependent on temperature. In the temperature range of 10 ℃ to 30 ℃, the relationship between temperature and diffusion coefficient of water is linear (Fig. 2.13).

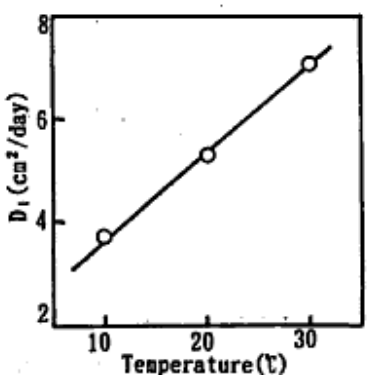

Fig. 2.13 Relationship between temperature and water diffusion coefficient (Fujiwara [6])

The function of pore humidity and temperature functions were proposed by Bazant [3] as semi-empirical equation of water diffusion coefficient. By modifying Bazant's equation, Mihashi [10] got numerical results consistent with the experiments by Schwesinger [11]. The elevated temperature were 20℃~102℃ and 20℃~132℃.

Afterward, a mathematical model was presented by Numao [12] to describe the drying process of concrete heated at elevated temperatures. A series of tests were performed, with concrete and mortar cylinders of two different water-cement ratios heated up to 80℃, 110℃, 150℃ and 200℃. Their numerical analysis results agreed well with the experimental results.

The temperature dependency of water diffusion coefficient in polymer cement mortar was assessed by Park [9] on the basis of Bazant and Mihashi's equation. They performed drying experiment at 5℃, 20℃ and 40℃, respectively. The water diffusion coefficient is evidently dependent on the temperature; higher temperature leads to higher diffusion coefficient, as presented in Fig. 2.10.

As proved in the foregoing researches, temperature is a potential of water diffusion, and should be assessed in moisture transfer of cement based materials. Moreover, the range of temperature being studied needs to be extended.

2.1.5 Effect of aggregate size on water diffusion coefficient

Cement paste, mortar and concrete have aggregate sizes different from each other. Concrete with coarse aggregate has the maximum grain size. Mortar with fine aggregate has smaller aggregate size, and cement paste without aggregate has the minimum grain size as 0 mm.

The water diffusion coefficient of concrete was experimentally studied by Sakata [2] and Akita [7]. The water diffusion coefficient of mortar was experimentally studied by Akita [4]. The water diffusion coefficient of cement paste was experimentally studied by Maruyama [8]. However, the foregoing experiments had cement in different types, which makes difficult the comparison between different cement based materials in water diffusion coefficient. To do such comparison, drying experiments of concrete, mortar and cement paste should be performed under the identical cement and water cement ratio.

2.2 Concrete properties change under drying

2.2.1 Compressive strength

Maruyama et al. have reported the changes in concrete compressive strength during heating to 90 ℃ or drying [13]. The change of the compressive strength of the concrete was not monotonic under

drying, as demonstrated by that research. The damage caused by the different volume change between the paste and aggregate and the strength change of harden cement paste during drying affect the compressive strength of concrete. Aggregates with greater shrinkage or with smaller size cause less damage to the concrete, while aggregates with smaller shrinkage or larger size cause more damage to the concrete. It was confirmed that the damage was mainly accumulated from sealed condition to 60% RH. For concrete using aggregates with larger shrinkage or with smaller size, damage is not accumulated from the different shrinkage between aggregate and mortar, the behaviour of cement paste are expressed in concrete strength, and thus the relationship between normalized strength Fc/Fco (strength at dried state/strength at sealed condition) and drying conditions are similar to that of mortar (see Fig. 2.14). In contrast, in the course of drying, the damage is accumulated progressively when the aggregate with small shrinkage and large size are used in concrete, and the increase of concrete strength due to cement paste is neutralized by such damage.

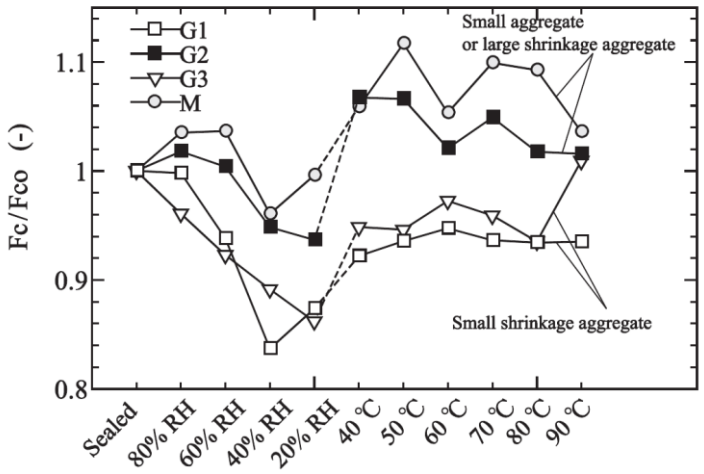

Fig. 2.14 Impact of the shrinkage properties of aggregate on normalized strength (Fc/Fco) under different drying conditions. M represents mortar. The coarse aggregate of concrete G1, G2 and G3 is limestone, sandstone and altered tuff, respectively (Maruyama et al. [13]).

Furthermore, as reported by Maruyama et al. [14], cement paste combines characteristics of porous and colloidal, shows various strength levels under drying conditions (as presented in Fig. 2.15 and Fig. 2.16), which can be expounded by the increasing strength in solid phase and macropores arising from the calcium-silicate hydrate's colloidal behavior (abbreviated as C-S-H). From 95% RH (close to sealed conditions) to 80% RH, the strength slightly increased. It could be explained by inter-globule bonding, which results from the orientation and rearrangement of globules forming the fibrillar C-S-H. In the range of 80%~40% RH, the strength decreased and arrived its lowest compressive strength at 40% RH,

which is expounded by the increase in macropores' amount arising from the globule clusters' consolidation according to the surface free energy. The globules structure and strength of globule do not change over the range of this drying condition. Under severer drying conditions than 40% RH, strength tends to increase, which is explained by the globule strength change arising from the densification of the globules by the removal of water from the interlayers. Similarly, in the case of concrete with a W/C of 0.55, the lowest compressive strength was found to be at 40% RH. Under more serious drying conditions, strength tends to increase.

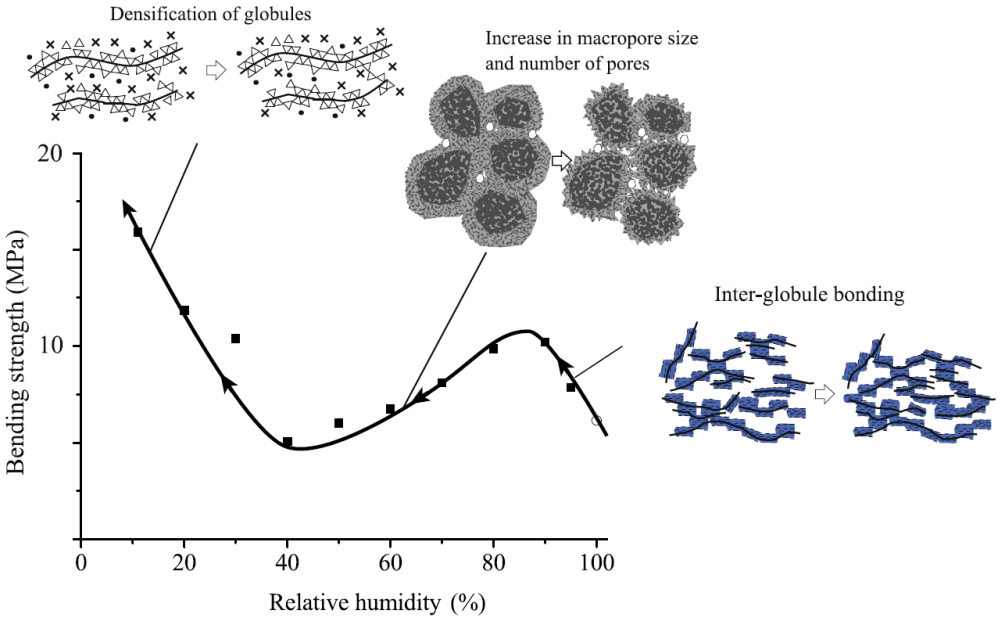

Fig. 2.15 Schematic of relationship between the microstructural changes caused by drying at various RHs and strength (Maruyama et al. [14]).

It is important to conduct testing under full equilibrium with no more moisture transport in the test specimens to admittedly prove the problems arising from drying, as indicated by the experimental results of Kishitani et al. [15]. The reason is the fact that self-stress is caused in the test specimens by the internal and external moisture distribution, which could be an error factor in the measurement. Pihlajavaara [16] also reported the importance of experiments under equilibrium conditions.

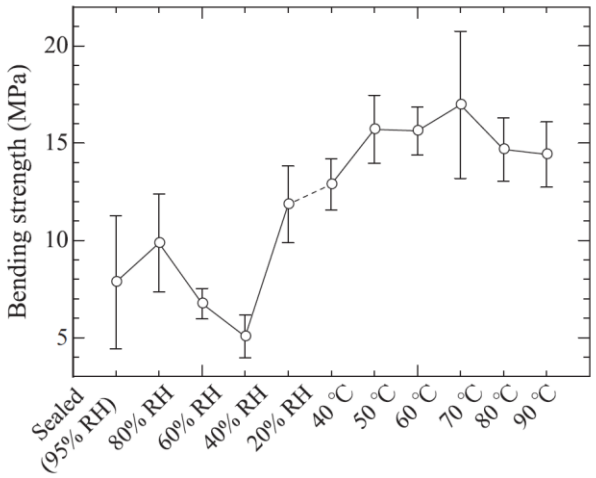

Fig. 2.16 Bending strength of harden cement paste under various drying conditions. Error bars of 1-sigma of measured variation are shown. (Maruyama et al. [14]).

2.2.2 Tensile strength

A high correlation between the tensile strength and compressive strength of concrete is unlikely to be found as in the case of concrete of young age that is undergoing hydration, given such a multi-factor strength determination mechanism discussed in Section 2.2.1 [17] [18].

The splitting tensile strength of ordinary concrete turns the greatest around 60% RH during drying at room temperature as highlighted by Hanson [19] (as presented in Fig. 2.17). It have shown that any drying environment between relative humidity of 75% and 10% has about the identical effect on splitting tensile strength measured at 28 days.

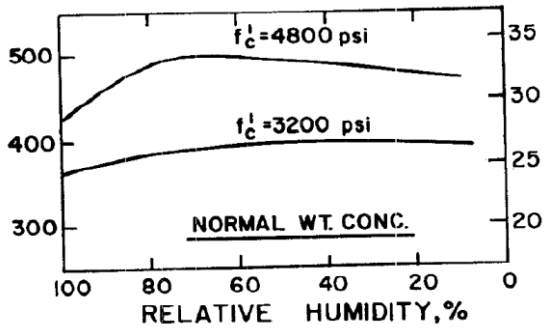

Fig. 2.17 28 day splitting tensile strength of concrete dried at different RH for 21 days

Additionally, as reported by Kishitani et al. [15], the splitting tensile strength of concrete, exposed to a high temperature for 1000 days, decreased as the temperature is elevated in the range up to 100 °C (see Fig. 2.18).

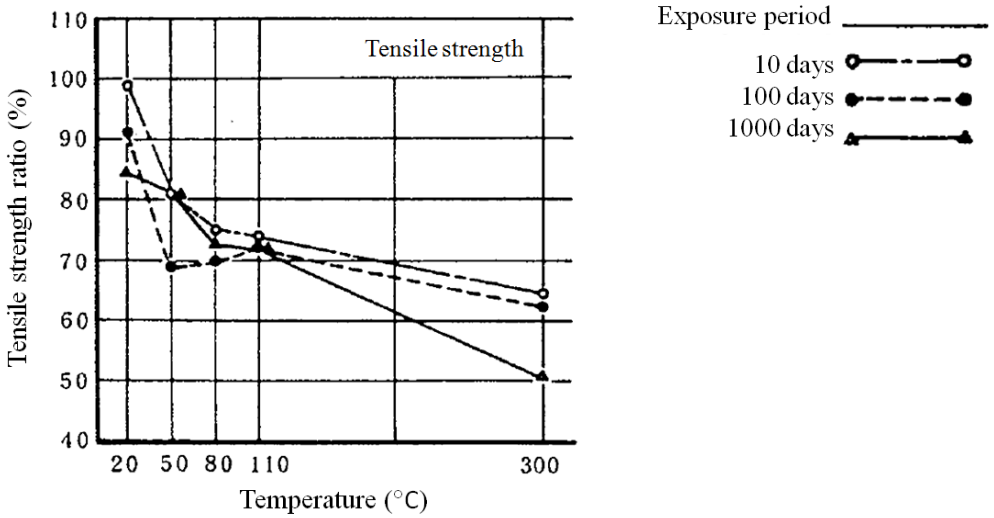

Fig. 2.18 Concrete properties affected by the exposure to high temperature (Kishitani et al. [15])

A high correlation between damage and strength was also reported by Kanda et al. [20]. The study experimentally illuminated the relationship between mechanical properties and damage in concrete in the environment with high temperature and low humidity. The drying conditions were heating temperature of 20, 50, 70°C, and humidity of 30, 60, 100% RH, respectively. The experimental results showed that the maximum decease of mechanical properties was 20%. The degree of damage in concrete and mechanical property variation was correlated in the test results (as presented in Fig. 2.19 and Fig. 2.20).

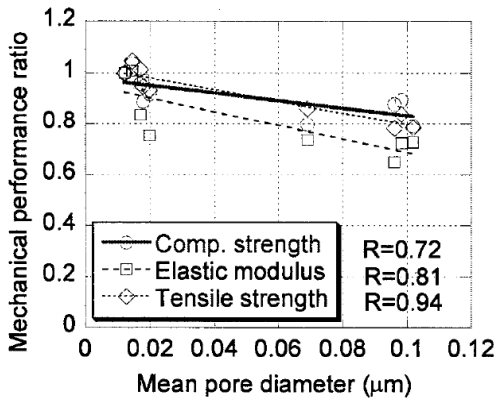

Fig. 2.19 Effect of mean pore diameter on mechanical performance (Kanda et al. [20])

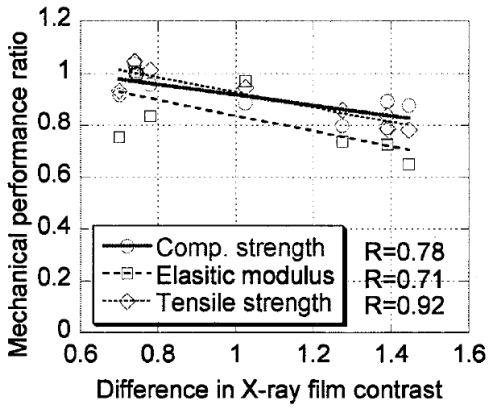

Fig. 2.20 Effect of X-ray film contrast on mechanical performance (Kanda et al. [20])

Tensile strength tends to decrease monotonically with temperature in the course of long-term drying, as also observed in a study by Naus et al. [21]. However, under short period of exposure to high

temperatures, tensile strength was also found extremely low in the range up to 100 ℃.

2.2.3 Drying shrinkage affected by aggregate

Affecting factors of drying shrinkage includes properties and amount of aggregate, specific surface area of aggregate, and type of aggregate. The aggregate of limestone, which has low drying shrinkage, corresponds to low drying shrinkage of concrete. Furthermore, drying shrinkage also varies with aggregate size. The numerical study was performed by Maruyama and Sugie [22] on drying shrinkage of concrete influenced by aggregate size. In the case of aggregate with large size, the thickness of the interfacial transition zone around the aggregate is relatively small compared to the diameter of coarse aggregate, and cracks might easily appear even at moderate dryness. They indicated that the influence of aggregate size on concrete shrinkage is affected by the surface area of aggregate. The analytical model considering characteristics of interfacial transition zone (ITZ) successfully reproduced the damage and the drying shrinkage strain with dependence on aggregate size. Shrinkage occurs in ITZ is the dominant factor. Therefore, concrete shrinkage may be reduced through controlling the distribution of aggregate size in order to decrease the amount of ITZ.

Fujiwara [23] did comprehensive research on the effect of aggregate on drying shrinkage of concrete. . The hardened cement paste shrinkage is considered restrained by aggregate, thus the concrete shrinkage is reduced. As presented in Fig. 2.17, in the case of normal concrete, the larger elastic modulus of aggregate leads to the smaller shrinkage of concrete. Therefore, the restraint of aggregate dominates. However, the shrinkage behavior of light weight concrete is different. Accordingly, the restraining effect of aggregate is not the only role of aggregate affecting drying shrinkage of concrete. The relationship between aggregate shrinkage and concrete shrinkage is shown in Fig. 2.22. There is an apparent proportional relationship for both normal and lightweight concrete. The shrinkage property of aggregate is strongly related to the drying shrinkage of concrete, as indicated by the study.

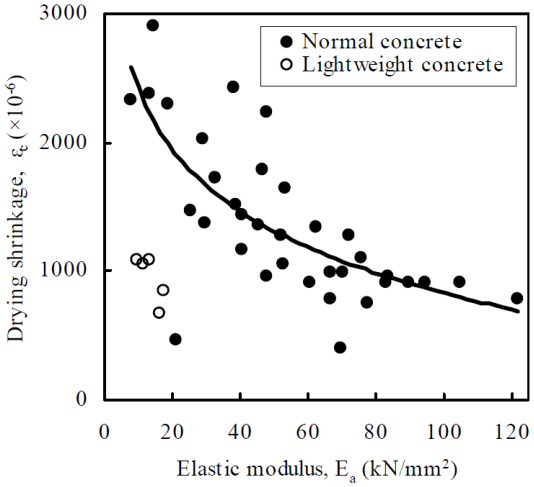

Fig. 2.21 Effect of elastic modulus of aggregate on drying shrinkage of concrete (Fujiwara [23])

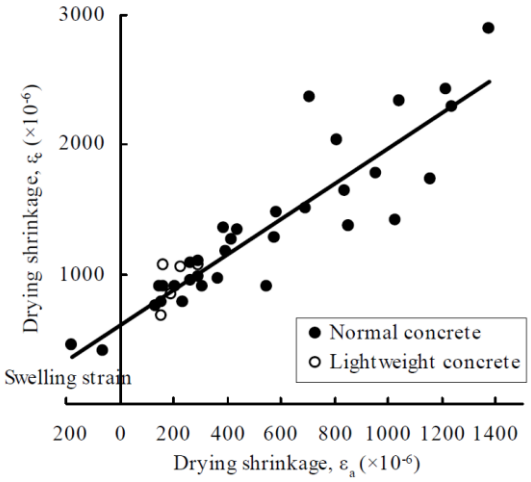

Fig. 2.22 Effect of length change of aggregate on drying shrinkage of concrete (Fujiwara [23])

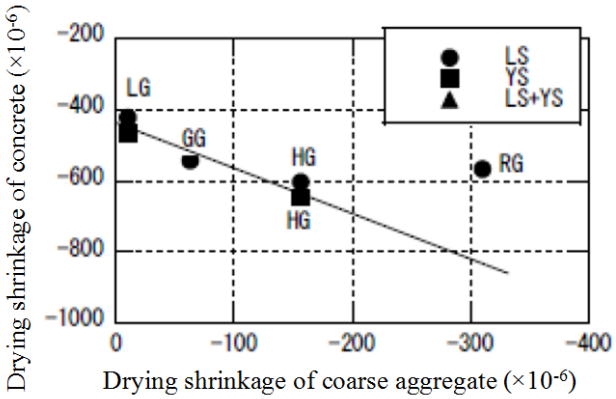

Fig. 2.23 The relationship between drying shrinkage of coarse aggregate and concrete (Tanaka [24])

To study the impact of aggregate properties on concrete properties, the experiments were performed by Tanaka et al. [24] with four types of coarse aggregate and two types of fine aggregate. The impact of coarse aggregate on concrete drying shrinkage surmounts that of fine aggregate, as indicated by the experimental results. The drying shrinkage of concrete increases with the increase of the drying shrinkage of coarse aggregate as presented in Fig. 2.23.

The impact of different aggregate properties on the drying shrinkage of mortar and concrete had been experimentally studied by W. Zhang et al. [25] with three types of coarse aggregate (limestone gravel, andesite gravel, and hard sandstone gravel) and 14 types of fine aggregate. According to the experimental results, for concrete specimens, the major impact factors on drying shrinkage are the characteristics of coarse aggregate, namely the shrinkage strain, absorption ratio, pore structure, and

specific surface area. The limestone aggregate can reduce the shrinkage of concrete. The smaller shrinkage strain of the coarse aggregate, the smaller the drying shrinkage of concrete is (see Fig. 2.24). It was revealed that the drying shrinkage of concrete increases with the increase of specific surface area of coarse aggregate as shown in Fig. 2.25.

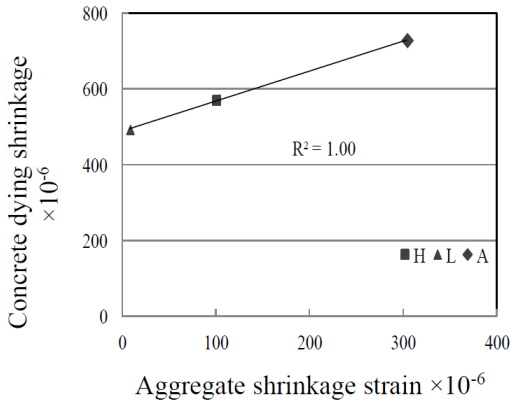

Fig. 2.24 Relationship between drying shrinkage and aggregate shrinkage strain (Zhang [25])

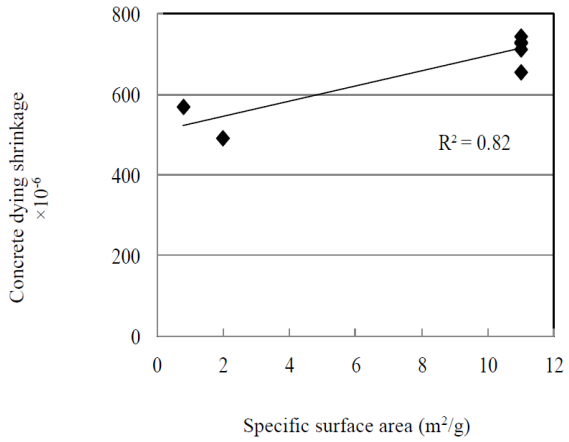

Fig. 2.25 Relationship between the specific surface area of coarse aggregate and drying shrinkage of concrete (Zhang [25])

2.3 **Shrinkage induced cracking**

2.3.1 Effect of aggregate properties on cracking of concrete

According to the study of P. Grassl [26], crack length increases as aggregate diameter decreases at the identical volume fraction (as presented in Fig. 2.26a). And the increase of volume fraction at the identical aggregate diameter consequently increases the crack length. Furthermore, crack width (Fig. 2.26b) decreases with decreasing aggregate size at constant volume fraction. And the increase of the volume fraction at constant aggregate diameter leads to the reduction of the crack width.

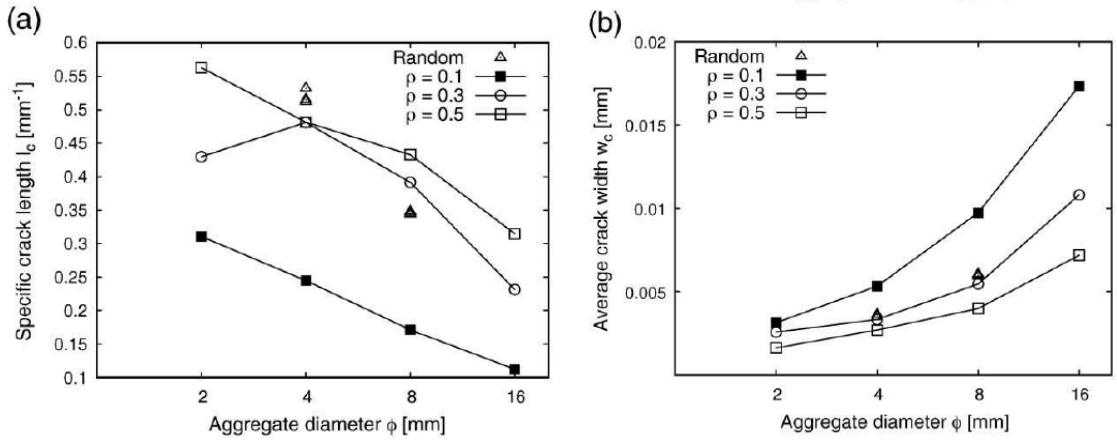

Fig. 2.26 The relationship between aggregate diameter and crack length/width. ρ is volume fraction of aggregate (P. Grassl [26]).

It has been reported that series of concretes which have the same volumetric mixture proportions except for coarse aggregate type showed different number of through-cracking under restrained condition and also difference in surface minor cracking [27][28]. The patterns of surface crack in concrete with different coarse aggregates are compared in Fig. 2.27. The crack patterns of two types of concrete recorded at 20℃ and a relative humidity of 60% RH are presented on the left of Fig. 2.27. These concrete types contained a coarse aggregate of pure limestone and exhibited a concrete shrinkage of about 600 microns, while the concrete on the right side of Fig. 2.27 contained a coarse aggregate of sandstone with considerable clay minerals and showed a concrete shrinkage of 1000 microns. It was experimentally confirmed that concrete with limestone had a smaller number of through-cracks than concrete with sandstone as the aggregate.

Fig. 2.27 Surface crack patterns of concrete with low-shrinkage limestone coarse aggregate (PL3-No.2) and high-shrinkage sandstone coarse aggregate (PL1-No.1) under uniaxial restraint conditions.

2.3.2 The behavior of concrete under restraint conditions

Concrete behavior under restraint condition is less studied than those under free condition. Among those, numerous researches on cracking behavior and initiation of through-cracking criteria can be found.

Understanding cracking of reinforced concrete structures due to volume change has become of more practical interest in recent years. Investigators have proposed various formulas that predict widely different forms of behavior of structures subjected to volume changes. Reinforced concrete base restrained walls were considered in the study of G.F. Kheder et al. [29], because they are widely used as retaining walls. The cracking behavior of 14 experimental walls and 61 full size walls was studied. The primary and secondary observed crack widths and spacings were compared with the values obtained using recently and previously developed formulas. Good agreement was found between those predicted values using the developed formulas and the observed values.

H.T. See et al. [30] performed an experiment and analysis process to quantitatively evaluate the behavior of restrained concrete with shrinkage using ring specimens. The results show that cracking resistance depend both on tensile creep characteristics and shrinkage rate of the concrete and on the tensile strength and shrinkage potential. Through reducing both the shrinkage rate and the shrinkage potential, the cracking concrete resistance is evidently intensified by shrinkage-reducing admixtures.

J.-H. Moon et al. [31] concluded that the bond condition between cement paste and aggregate has little impact on stress development when a concrete member is not restrained externally. But the bond condition becomes more crucial when the concrete member has external restraint.

A simple fracture mechanics model was proposed by S.P. Shah et al. [32] for the purpose of quantitatively predicting shrinkage induced cracking behaviour of a restrained concrete ring specimen subjected to drying. This work determined the specimen curve of fracture resistance (R-curve) with the measured fracture parameters. On that basis, given the energy balance while the ring was undergoing shrinkage, this work calculated the maximum tensile strain allowable. This work predicted the age at ring specimen’s transverse crack arising from the restrained drying shrinkage through equating the difference between the estimated creep and the measured free shrinkage to the maximum allowable tensile strain. The predicted age at cracking reasonably agreed with the experimental results.

2.3.3 ITZ impact on drying shrinkage

Maruyama et al. [22] implied that property of interfacial transition zone (ITZ) has an impact on the drying shrinkage of concrete.

The study of P.J.M. Monteiro et al. [33] indicates that carbonate rock has reaction with cement paste at the interface. The etching of calcite and the succeeding precipitation of crystals which are much

smaller than calcium hydroxide may be the causes for the strength increase of concrete containing limestone.

X. Ping et al. [34] found that there are two major factors influencing bond strength at the interface between cement paste and nonporous aggregate, i.e. water to cement ratio and the thickness of the water layer on the surface of aggregate at the beginning of mixing. Therefore, it is possible to increase the bond strength by decreasing w/c ratio and the thickness of the water layer.

2.3.4 DICM for measurement of crack propagation

Although crack propagation due to drying is difficult to observe experimentally, a measurement method for crack propagation using a digital image correlation method (DICM) has been recently developed to address this problem [35].

A random pattern was first sprayed on the specimens in this measurement method. After that, with a digital camera, the surface before and after drying was captured. In the DIC algorithm, subset regions have a certain luminance distribution pattern. The images of subset regions before and after drying are compared, and the displacement vector of the centre pixel of the subset region is determined by the correlation between them. The surface colour variation arising from drying is observed as an initial image is adopted without any treatment. Accordingly, the correlating algorithm shall be failed. In this regard, the black and white acrylic paints on the surfaces of the specimens were adopted in this method.

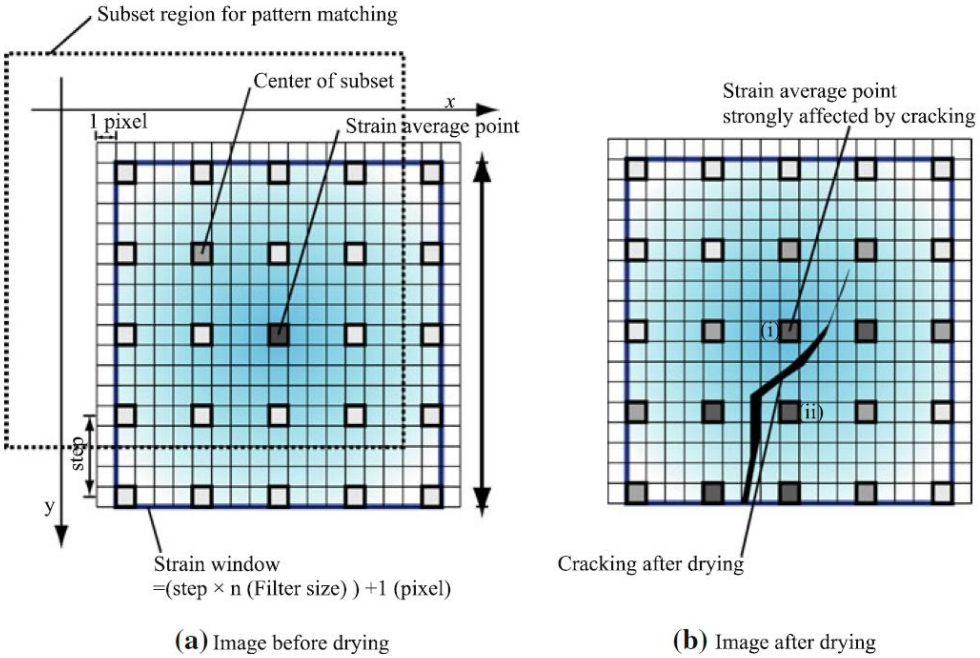

Fig. 2.28 Schematic of subset, filter size and strain window in DIC algorithm and effect of cracking on DIC results (Maruyama [35])

This method employed a commercial program (Vic-2D) for the DIC analysis. An algorithm for maximizing a normalized cross-correlation criterion (abbreviated as NCC) between the reference subset and the deformed subset was implemented in Vic-2D. To conduct DIC for the determination of local displacement and strain distributions, a decay filter (90% center-weighted Gaussian filter), a step of 5 (5-pixel-spacing between centers of subset) and a subset of 25 pixels × 25 pixels were employed in the analysis. Fig. 2.28 presents the schematic of those parameters.

Given that shadow dropping and defocusing in air bubbles will make DIC results inaccurate, this method, while analyzing the image, omitted a cross-section containing entrained air bubbles on the surface of specimen. Consequently, the DIC calculation will be aborted sometimes. Even small cracks on the specimen surface can induce a large expansive strain in the DIC algorithm. When two centre pixels of a subset located near a crack are focused on, relative displacement between pixel (i) and pixel (ii) is increased arising from the opening of crack, and even macroscopic strain of concrete is shrinkage, as presented in Fig. 2.28b. Given this, the DIC algorithm cannot directly locate the opening of crack, whereas it is able to indicate the expansive strain near the opening of crack.

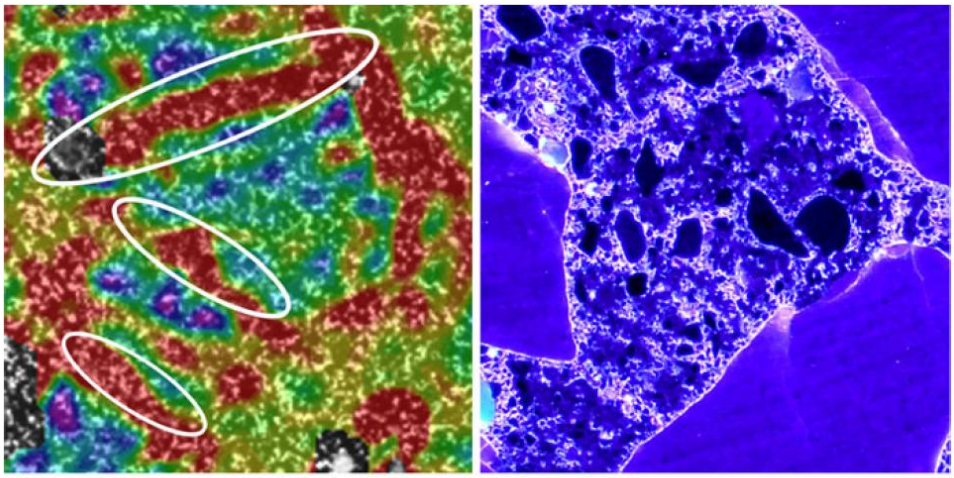

(a) DIC method **(b)** fluor-epoxy impregnation

Fig. 2.29 Comparison of magnified images of maximum principle strain distribution (a) and image obtained with FEIM (b) (Maruyama [35])

DICM shows strain distributions, while FEIM shows crack distribution. Expansive strain at distribution of maximum principal strain obtained by DICM had high correlation with crack position obtained by FEIM (see Fig. 2.29). It suggested that DICM could be used for the damage evaluation of cross section of concrete along with time. Two kinds of fine cracks were found, i.e., interfacial cracks between mortar and aggregate by virtue of the formation of stress arch and cracks restrained by aggregate.

2.3.5 Rigid-body-spring networks (RBSN)

The Rigid-Body-Spring Networks (RBSN) was developed by Kawai [36] and has been applied for structural analysis. The RBSN easily deals with crack propagation of concrete directly [37], because the RBSN represent a continuum material as an assembly of rigid particle elements interconnected by zero-size springs along their boundaries and the zero-size springs having the nonlinearity as it can simulates the cracking behavior of continuum material. The nonlinearity and discrete behavior of continuum material is emulated by the crack development at the interfaces of the rigid particles.

The truss networks model was adopted for analysis of mass transfer, and the RBSN model was employed for structural analysis by H. Nakamura et al. [38]. The analysis incorporate drying shrinkage caused by water movement, rebar corrosion caused by ions penetration and external load. The presented approach well simulated the process of deterioration due to mass transfer for initial cracking behavior and ultimate behavior of concrete structures. As shown in Fig. 2.30, each rigid particle has two translations and one rotational degree of freedom at the nuclei. Three individual springs in the rotations, tangential and normal are included as the interface between two particles. The crack pattern and resultant nonlinear behavior of the targeted model are evidently impacted by the mesh design, as cracks initiate and propagate along the rigid particle interfaces. To address this problem, random geometry using Voronoi diagrams [37] is adopted to partition the material into assembly of rigid particle. The mesh bias on potential crack directions is abated with the random geometry.

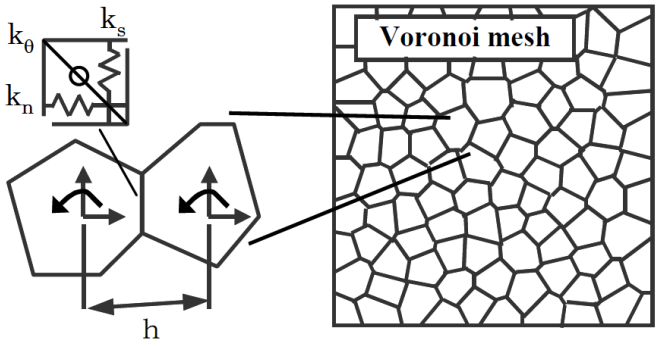

Fig. 2.30 Rigid-Body-Spring Networks (H. Nakamura et al. [38])

Y. Yamamoto et al. [39] developed three dimensional Rigid-Body-Spring model to quantitatively reproduce compression fracture of concrete member (see Fig. 2.31). Constitutive models were developed and the parameters of material were adjusted through fitting the response of concrete under unaxial compression, uniaxial tension, laterally confined compression and hydrostatic compression from literature researches. It was concluded that the model could reasonably assess the increase of strength

and negative slope of the strain softening region with the increasing lateral pressure, as well as the localization behavior and the macroscopic strain-softening in uniaxial compression.

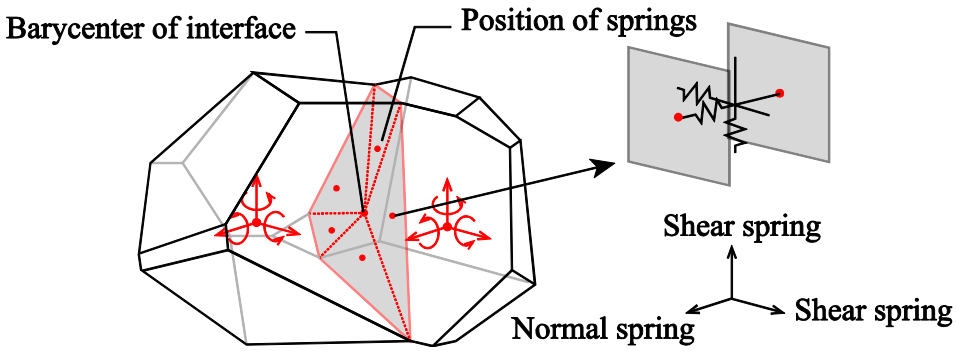

Fig. 2.31 3D Rigid-Body-Spring Model (Y. Yamamoto et al. [39])

2.3.6 Truss networks model for mass transfer

Water diffusion in the mortar and aggregate was modeled using a random lattice, whose mesh was defined by a Voronoi diagram, was originally developed by Bolander and Berton [40]. The elasticity and transport properties of the material are discretized using Voronoi diagrams on a semi-random set of points. Compared with the rest points in the domain, the Voronoi cell bound by point *i* is more approaching to point *i* (see Fig. 2. 32a). The material domain is robust in Voronoi partitioning which promotes the realization of a pre-processing automation in high degree. One of the advantages of this method is that the material structure, such as the boundaries between two phases, can be modelled explicitly with this method. This is realized through placing semi-regularly spaced points strategically before filling the domain randomly (Fig. 2.32b), and by the average size grade of cell, advantaged by the ablation of computational expense. Through adopting a random lattice defined by a Voronoi diagram, the problem of potential flow is modelled. The lattice sites are connected by lineal conduit elements as presented in Fig. 2.33; the cross section of an established conduit is equivalent to the corresponding Voronoi facet in area.

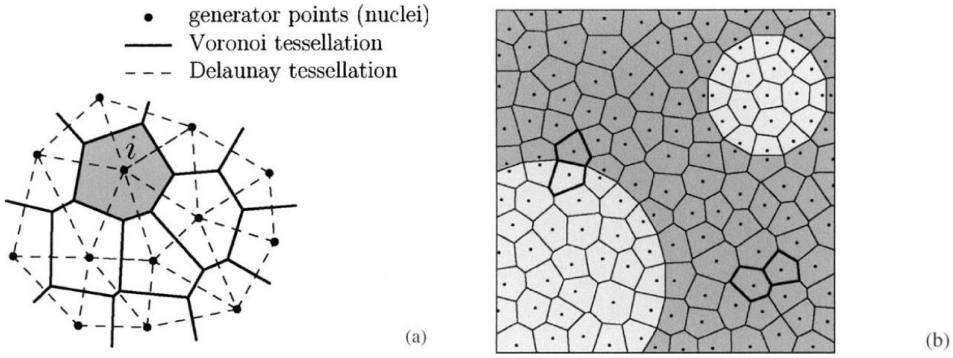

Fig. 2.32 (a) Dual tessellations of a two-dimensional set of points and (b) Voronoi diagram partitioning of a multi-phase material (Bolander and Berton [40])

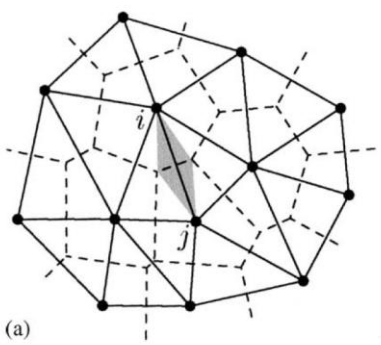

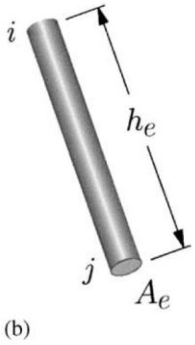

Fig. 2.33 Discretization for 2-D diffusion analysis: (a) conduit element *ij* within network, and (b) conduit element *ij* (Bolander and Berton [40])

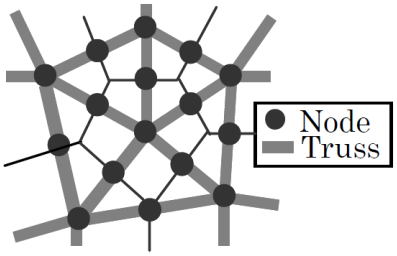

Fig. 2.34 Truss networks model (H. Nakamura et al. [38])

In the study of H. Nakamura et al. [38], the truss networks model was adopted to analyze the mass transfer for attaining the initial strain. Such attained strain is then employed for structural analysis by using RBSN with Voronoi diagrams. Truss elements link every Voronoi element with the nodes at the intermediate points of particle boundaries and Voronoi nuclei (as presented in Fig. 2.34). On that basis, a simplified one-dimensional diffusion equation is adopted for mass transfer. One of differences with the model proposed by Bolander and Berton [40] is that it assumes the node position of truss elements on middle points of the particle boundaries.

2.4 Summary

In this chapter, the past researches of water movement, concrete properties change due to drying and shrinkage-induced cracking in concrete are reviewed. Analytical methods and experimental results relating to this study are presented. The following conclusions are obtained through the literature review:

(1) Boltzmann-Matano method is efficient to experimentally evaluate water diffusion efficient of cement based materials. Both the approach of pre-cutting and cutting after drying could be applied for drying experiment as they have similar effect on water diffusion. Temperature dependency and effect of aggregate size on water diffusion coefficient need to be studied.

(2) Compressive strength of concrete changes during drying, and the change is not monotonic. The shrinkage property of aggregate has large influence on the strength development of concrete. Tensile strength of concrete also changes under various drying condition. The mechanism of change of tensile strength needs to be studied, and the role of aggregate properties playing in strength development also needs to be investigated.

(3) The pattern of shrinkage-induced cracking of concrete under restrained condition is influenced by aggregate properties. The drying shrinkage of concrete is influenced by the properties of interfacial transition zone. Therefore, the impact of aggregate properties on shrinkage-induced cracking of concrete needs to be investigated. DICM is an efficient method for measuring crack initiation and propagation. Rigid-body-spring networks (RBSN) is suitable for simulating cracking behavior, and Truss networks model could be applied for moisture transport.

References

1 T.C. Powers, “Mechanisms of shrinkage and reversible creep of hardening cement paste”, in Proc. Int. Symp. “Structure of Concrete and its behabiour under load”, London, 1965, pp. 319-344

2 K. Sakata, “A Study on Moisture Diffusion in Drying and Drying Shrinkage of Concrete”, Cement and Concrete Research, Vol. 13, Mar. 1983, pp. 216-224

3 Z.P. Bazant, and L.J. Najjar, “Nonlinear Water Diffusion in Nonsaturated Concrete”, Materiaux et Constructions, Vol.5, 1972, pp.3-20

4 H. Akita, T. Fujiwara and Y. Ozaka, “Water Movement within Mortar due to Drying and Wetting”, Proceedings of JSCE, No. 420, 1990, pp. 61-69 (In Japanese)

5 T. Fujiwara, K. Sato, and T. Konishi, “Water Movement within Concrete due to Drying and Wetting”, Review of 42 General Meeting, CAJ, 1988, pp. 427-430 (In Japanese)

6 T. Fujiwara, M. Kayaba, and H. Akita, “Water Movement within Concrete due to Drying under Various Temperature Conditions”, CAJ Proceedings of Cement & Concrete, No.46, 1992, pp.428-433 (In Japanese)

7 H. Akita, T. Fujiwara and Y. Ozaka, “An Analytical Method of Moisture Transfer within Concrete due to Drying”, Proceedings of JSCE, No. 490, 1994, pp.101-110 (In Japanese)

8 I. Maruyama, G. Igarashi, and N. Kishi, “Fundamental Study on Water Transfer in Portland Cement Paste”, Journal of Structural and Construction Engineering. Transactions of AIJ, No. 668, vol.76, Oct. 2011, pp.1737-1744 (In Japanese)

9 D. Park, M. Kanematsu, T. Noguchi, “A Study on the Drying of Polymer Modified Cement Mortar used as Patch Repair Materials and Constraint Stress Analysis”, Concrete research and technology 18(2), 2007, pp. 71-82 (In Japanese)

10 H. Mihashi , F.H.Wittmann , P. Roelfstra, ‘Theoretical study on water diffusion under high temperature’, Proceedings of cement technology, Vol.41, 1987, pp.495-498 (in Japanese)

11 P. Schwesinger, Drying process of concrete at elevated temperatures, Technical Report at Architecture and Building College of Weimar (1980)

12 T. Numao, H. Mihashi, and K. Fukuzawa, ‘Moisture diffusion process in concrete at elevated temperatures’, Journal of Structural and Construction Engineering. Transactions of AIJ, No. 441, 1992 (In Japanese)

13 I. Maruyama, I., H. Sasano, Y. Nishioka and G. Igarashi, "Strength and Young's modulus change in concrete due to long-term drying and heating up to 90 ℃." Cement and Concrete Research, 66 (2014), 48-63.

14 I. Maruyama, Y. Nishioka, G. Igarashi and K. Matsui, "Microstructural and bulk property changes in hardened cement paste during the first drying process." *Cement and Concrete Research* 58(2014), 20-34.

15 K. Kishitani, H. Kasami, F. Oshida and T. Okuno (1982). "Properties of concrete exposed to 20～300℃, Part 1 and 2." Summaries of technical papers of Annual Meeting Architectural Institute of Japan, Structure (57), 317-320.

16 S.E. Pihlajavaara, A review of some of the main results of a research on the ageing phenomena of concrete: effect of moisture conditions on strength, shrinkage and creep of mature concrete, Cem. Concr. Res. 4 (1974), 761–771.

17 Comité Euro-International du Béton, "CEB-FIP Model Code 90", 1993, Thomas Telford.

18 Japan Concrete Institute , "Guidelines for Control of Cracking of Mass Concrete 2008". Tokyo, Japan Concrete Institute, 2008.

19 J.A. Hansen, "Effects of curing and drying environments on splitting tensile strength of concrete." Journal of the American Concrete Institute (65), 1968, 535-543.

20 T. Kanda, Y. Ichikawa, O. Kontani, M. Takeda and K. Otsuka. "Experimental investigation of concrete damaged by exposuring to high temperature and low humidity environment." Journal of structural and construction engineering (615), 2007, 15-22.

21 D.J. Naus, "A compilation of elevated temperature concrete material property data and information for use in assessments of nuclear power plant reinforced concrete strucutres", 2010, NUREG/CR-7031, US-NRC.

22 I. Maruyama and A. Sugie, "Numerical Study on Drying Shrinkage of Concrete Affected by Aggregate Size." Journal of Advanced Concrete Technology 12(8), 2014, 279-288.

23 T. Fujiwara, "Effect of Aggregate on Drying Shrinkage of Concrete", Journal of Advanced Concrete Technology 6(1), 2008, 31-44.

24 H. Tanaka and H. Hashita, “Influence of aggregate type on the drying shrinkage of concrete”, Proceedings of Japan concrete institute, Vol.31, No.1, 2009, 553-558

25 W. Zhang, M. Zakaria, Y. Hama, “Influence of aggregate materials characteristics on the drying shrinkage properties of mortar and concrete”, Construction and Building Materials, 49 (2013) 500-510.

26 P. Grassl, H.S. Wong, N.R. Buenfeld, Influence of aggregate size and volume fraction on shrinkage induced micro-cracking of concrete and mortar, Cement and Concrete Research, 40 (2010) 85-93.

27 Y. Mitani, M. Tanimura, I. Maruyama, Shrinkage cracking characteristics of concrete using shrinkage reducing agent, in: AIJ (Ed.) Summaries of technical papers of annual meeting, Sapporo, Japan, 2013,

pp. 41-42.

28 Y. Mitani, Y. Ishii, M. Tanimura, I. Maruyama, Quantitative evaluation on reduction effect of drying shrinkage cracks by expansive additive, in: AIJ (Ed.) Summaries of technical papers of annual meeting, Nagoya, Japan, 2012, pp. 747-748.

29 G.F. Kheder, R.S.A. Rawi, J.K.A. Dhahi, Study of the Behavior of Volume Change Cracking in Base-Restraint Concrete Walls, ACI Materials Journal, 91 (1994) 150-157.

30 H.T. See, E.K. Attiogbe, M.A. Miltenberger, Shrinkage Cracking Characteristics of Concrete Using Ring Specimens, ACI Materials Journal, 100 (2003) 239-245.

31 J.-H. Moon, F. Rajabipour, B.J. Pease, J. Weiss, Autogenous shrinkage, residual stress, and cracking in cementitious composites: The influence of internal and external restraint, in: B. Persson, D. Bentz (Eds.) Fourth International Seminar on Self-desiccation and Its Importance in Concrete Technolog, Lund University, Washington D. C., USA, 2005, pp. 1-20.

32 S.P. Shah, C. Ouyang, S. Marikunte, W. Yang, E. Becq-Giraudon, A Method to Predict Shrinkage Cracking of Concrete, ACI Materials Journal, 95 (1998) 339-346.

33 P.J.M. Monteiro, P.K. Mehta, Interaction between carbonate rock and cement paste, Cement and Concrete Research, 16 (1986) 127-134.

34 X. Ping, J.J. Beaudoin, Effects of transition zone microstructure on bond strength of aggregate-portland cement paste interfaces, Cement and Concrete Research, 22 (1992) 23-26.

35 I. Maruyama, H. Sasano, Strain and crack distribution in concrete during drying, Mater Struct, 47 (2014) 517-532.

36 T. Kawai, New discrete models and their application to seismic response analysis of structures, Nuclear Engineering and Design, 48 (1978) 207-229.

37 J.E. Bolander Jr, S. Saito, Fracture analyses using spring networks with random geometry, Engineering Fracture Mechanics, 61 (1998) 569-591.

38 H. Nakamura, W. Srisoros, R. Yashiro, M. Kunieda, Time-Dependent Structural Analysis Considering Mass Transfer to Evaluate Deterioration Process of RC Structures, Journal of Advanced Concrete Technology, 4 (2006) 147-158.

39 Y. Yamamoto, H. Nakamura, I. Kuroda, N. Furuya, Analysis of compression failure of concrete by three dimensional regid body spring model, Doboku Gakkai Ronbunshuu E, 64 (2008) 612-630.

40 J.E. Bolander Jr, S. Berton, Simulation of shrinkage induced cracking in cement composite overlays, Cement and Concrete Composites, 26 (2004), 861-871.

Chapter 3
Fundamental Study on Water Diffusion Coefficient of Cement Based Material

3.1 Introduction

Water movement is an important topic affecting the durability and service lives of concrete structures. The water/cement ratio of normal concrete is from 0.4 to 0.6. Concrete mixtures contain more water than necessary for cement hydration. Water would evaporate if the environment is dry. The water loss would induce insufficient cement hydration on the surface of concrete if the demolding time is short. The insufficient cement hydration would lead to coarse cover (rough surface) which facilitates the penetration of substances leading to rebar corrosion. Continuous water loss is strongly related to drying shrinkage and shrinkage induced stress and cracking. The shrinkage crack could be through crack or surface crack. The effects of these two kinds of crack on durability are different, however, they both jeopardise the durability of concrete structures. Besides these effects, the water content distribution in concrete components has an important impact on the movements of chloride ion and carbon dioxide.

Based on above-mentioned knowledge, the studies on water movement in concrete are necessary for long term design and maintenance of concrete structures. The experimental study of water movement was firstly conducted by Sakata [1]. Sakata used Boltzmann-Matano method to obtain the relationship between water content and water diffusion coefficient. The difficulty of water movement phenomena is that it takes too much time to attain equilibrium for porous materials. Therefore, compared to other methods, Boltzmann-Matano method has benefits for cement based materials. The details of Boltzmann-Matano method are introduced in Section 2.1.2. The dependency of water diffusion coefficient on water content was confirmed by Bazant [2] through numerical study.

After Sakata's studies, Akita and Fujiwara also did comprehensive research on water movement [3-5]. They used different methods to acquire the relationships between water content (or relative water content) and water diffusion coefficients, and got consistent results as Sakata. The experimental results are presented in Section 2.1. Besides these experimental results, they got further discovery on temperature dependency of water diffusion coefficient (see Section 2.1.4). They also studied on water diffusion coefficient in low water content range, and water diffusion coefficient of desorption and adsorption processes.

In this chapter, the effects of temperature and aggregate size on water diffusion coefficient are focused on, and the reproductions by comparing with the existing researches are discussed.

3.2 Experiment

3.2.1 Temperature dependency of water diffusion coefficient in mortar

The drying experiment of mortar specimens was conducted to evaluate the temperature dependency of water diffusion coefficient. In this study, normal Portland cement is used (marked as N). Cement properties are listed in Table 3.1. Standard sand with density of 1.76g/cm^3 is used as fine aggregate. The water absorption of the fine aggregate is 0.42% and the maximum grain size is 2 mm. Water/cement ratio is 0.55, and the proportion of cement to sand is 1:1.8. The dimension of mortar specimen in this experiment is 200×44×10 mm. The specimens are demolded 3 days after casting, and cured in a saturated solution of calcium hydroxide under the constant temperature 20±1°C. The saturated solution of calcium hydroxide was chosen to prevent the leaching of calcium from those specimens. To attain a stable porous structure, the drying experiment was performed after standard water curing for 300 days. At that time, the hydration process had been completed in the mortar specimens, and the effect of hydration could be neglected.

In this experiment, all the surfaces of the specimens are sealed with aluminium tape except for one surface exposed to the air for drying as shown in Fig. 3.1. In this way, the water diffusion became one dimension problem. And then the specimens were dried in temperature and humidity controlled chambers. The drying temperature was 20°C, 40 °C and 55 °C, respectively. The 20 °C chamber used silica desiccant to control relative humidity below 15%.

Table 3.1 Cement Properties

Cement Type	Density (g/cm^3)	Specific Surface (cm^2/g)	LOI (%)	Chemical Composition (mass %)								
				SiO_2	Al_2O_3	Fe_2O_3	CaO	MgO	SO_3	Na_2O	K_2O	Cl^-
N	3.16	3110	0.64	21.8	4.49	2.90	63.9	1.84	2.26	0.20	0.38	0.007

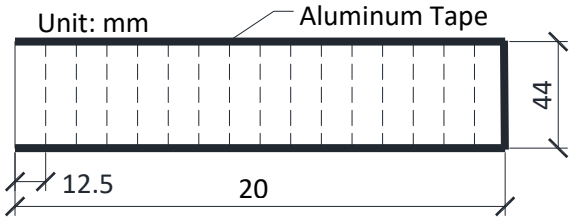

Fig. 3.1 Mortar Specimens Dimensions

To calculate water diffusion coefficient, those specimens were dried over 7, 14 and 28 days, respectively. The water content distribution is determined by the water content at various depth from the drying surface at various time which was 7, 14 and 28 days after drying, respectively. Fujiwara [4] proposed 3 drying approaches: 1. precutting; 2. cutting after drying; 3. using specimens with various lengths. In this experiment, the second approach, cutting after drying, was adopted. The specimens were cut into 16 segments with identical length. Each segment was weighed immediately after drying, and then dried for 24 hours at 105℃ to get its absolute dry

mass. The mass change before and after 105℃ drying was the water content of each segment. A digital precision balance with resolution of 0.0001g was used to measure the mass of those specimens in this study.

In addition, to check the sealing effect of aluminum tape in this experiment, specimens with all surfaces sealed, were also dried under the temperature of 20°C, 40°C and 55°C, respectively. The mass changes after drying for 28 days were 0.559%, 0.202% and 1.052%, respectively. These results show that the aluminum tape offers a good sealing condition in this experiment.

The drying process of the mortar specimens is a one-dimension problem, so one dimension diffusion equation, Eq. (3.1), is applicable here. In this study, Boltzmann-Matano method was applied to process the experimental data. Boltzmann variable λ is assumed to be $\lambda = x/\sqrt{t}$. After Boltzmann transformation, Eq. (3.1) becomes Eq. (3.2), in which water diffusion coefficient *D(w)* (m^2/s) is expressed as a function of water content.

$$\frac{\partial w}{\partial t} = \frac{\partial}{\partial x}\left(D\frac{\partial w}{\partial x}\right) \qquad (3.1)$$

$$D(w) = -\frac{1}{2}\int_{w_0}^{w} \lambda dw / \frac{\partial w}{\partial \lambda} \qquad (3.2)$$

where,

λ : Boltzmann variable ($m/s^{1/2}$)

x : distance from the drying surface (m)

t : drying time (s)

w_0 : saturated water content (g/m^3)

w : water content at any time (g/m^3)

The relationship between λ and *w* can be obtained by the regression of the experimental data, and then Eq. (3.2) can be solved. Based on the existing researches, the fitting function from Akita [3] was applied for experimental data regression in this study as follows:

$$w = w_0\left(1 + f - \frac{a}{(\lambda/2 + b)^2}\right) \qquad (3.3)$$

where: *a*, *b*, and f is the constants in the fitting function obtained by fitting the experimental data using least square method. In this study, relative water content *R* ($R=w/w_0$) is used as a parameter.

Figs. 3.2 to 3.4 shows the relative water content changing along with drying time at different depths from the drying surface of the specimens under different drying temperature of 20 °C, 40 °C and 55 °C. It is clearly demonstrated that the drying rate is the highest at the depth of 6.25 mm from the drying surface, and the drying rate slow down as the distance from the drying surface is larger. Furthermore, according to those figures, the temperature dependency of water content is apparent. The specimens lose more water when the drying temperature is higher.

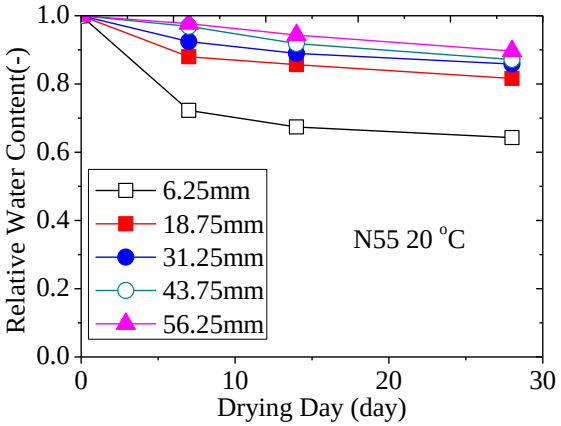

Fig. 3.2 Relative water content at 20 °C

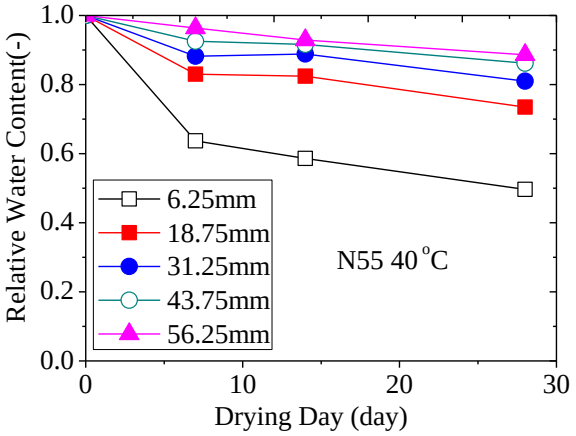

Fig. 3.3 Relative water content at 40 °C

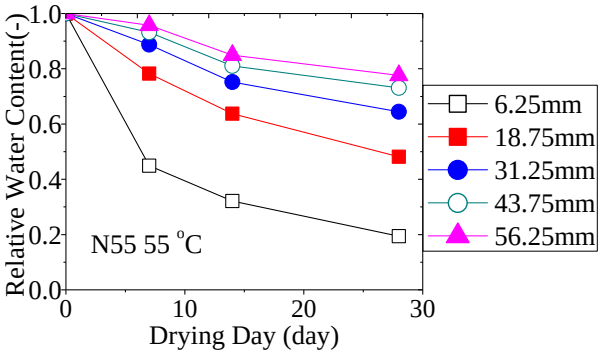

Fig. 3.4 Relative water content at 55 °C

The water diffusion coefficient is calculated through Boltzmann-Matano method. The relationship between relative water content R and Boltzmann variable λ is acquired by the regression of the experimental data. Eq. (3.3) is applied as the fitting function of such regression. In Figs. 3.5 to 3.7, the experimental results are plotted with λ on the X-axis and R on the Y-axis, and the regression curves are also plotted. The constants of Eq. (3.3) of the regression results are listed in Table 3.2.

Table 3.2 Constants of Eq. (3.3)

Temperature	*a*	*b*	*f*
20℃	0.03859	0.2678	0.0001
40℃	0.09866	0.4004	0.0001
55℃	0.2213	0.4712	0.0001

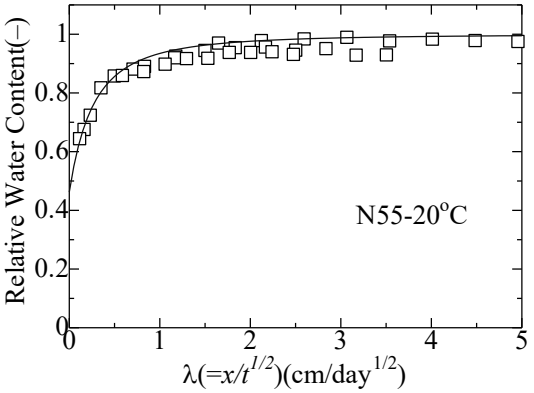

Fig. 3.5 Relationship of *R* and λ at 20 °C

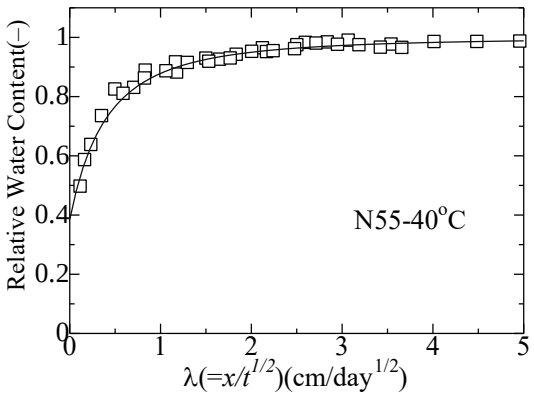

Fig. 3.6 Relationship of *R* and λ at 40 °C

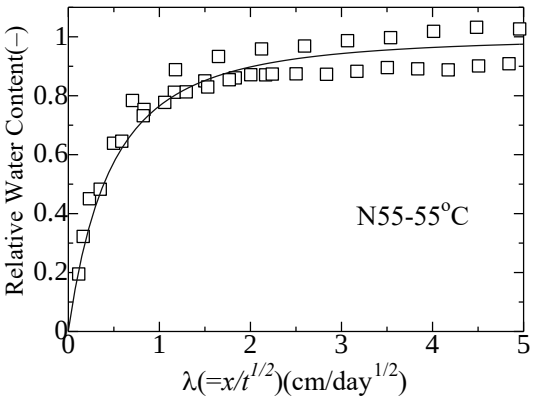

Fig. 3.7 Relationship of *R* and λ at 55 °C

Based on the function of λ and *R* obtained by the above-mentioned regression of the experimental data, the water diffusion coefficient is calculated through Eq. (3.2). The results of water diffusion coefficient (WDC) and R are plotted in Fig. 3.8. It can be seen that WDC become

larger when water content is higher. When R is above 90%, WDC increase sharply, while the increasing rate of the WDC in the range of low water content is relatively small. Such results show the same trend as Sakata [1] and Akita [3]. WDC is not only affected by water content, but also affected by the drying temperature. The higher the temperature, the larger the WDC is.

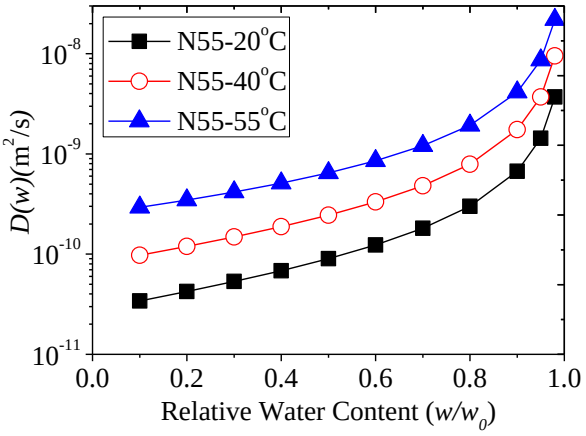

Fig. 3.8 Water diffusion coefficient of mortar

The value of relative WDC *D/D20* at relative humidity of 90% are compared with Fujiwara's paper [5], where *D20* is the WDC under the drying temperature of 20 °C. The comparing results are shown in Fig. 3.9. Temperature dependency of WDC is confirmed through such results. In the high temperature range, temperature has more influence on WDC. According to the fitting curve of the data, the relationship of T and *D/D20* follows power law. The details of the fitting function are listed in Fig. 3.9.

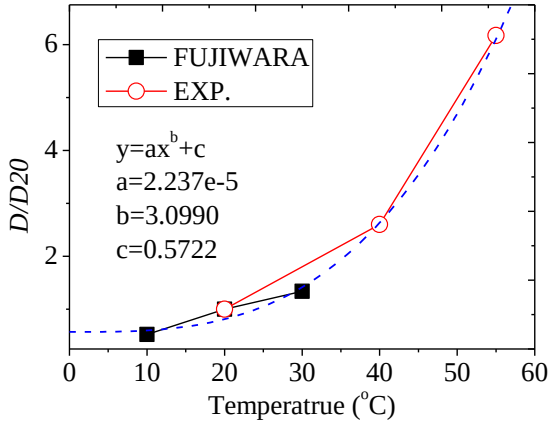

Fig. 3.9 Relation between temperature and *D/D20*

3.2.2 Effect of Aggregate Size on Water Diffusion Coefficient

Ordinary Portland cement is used in the experiment. Diorite crushed stone is used as coarse aggregate. The density of the coarse aggregate under saturated surface-dry condition is 2.95g/cm^3, while the water absorption of it is 0.48% and the maximum grain size is 20 mm. Crushed sand is used as fine aggregate. The water absorption of it is 2.34% and the maximum grain size is 5 mm.

The mix proportion of concrete are listed in Table 3.3. The specimen size is ϕ 100×300 mm. The concrete specimens are demolded 2 days after casting and then cured in saturated solution of calcium hydroxide. The use of a saturated solution of calcium hydroxide was to prevent the leaching of calcium from the specimens. The drying experiment started after the concrete age of 100 days. The ambient temperature is 20℃ and the relative humidity is 40% for the drying experiments.

Table 3.3 Mix proportion of concrete

W/C	Fine aggregate ratio	Mass (kg/m^3)			
		Water	Cement	Sand	Coarse aggregate
0.55	0.43	185	336	783	1026

The drying experiments adopt the method of pre-cutting. As discussed by Fujiwara [4], for the method of pre-cutting, the drying rate is relatively slow, but the trend of water content distribution from the drying surface is consistent with other drying approaches. Moreover, the effect of the cutting surface on water movement inside the concrete specimens is small. As the water loss is larger near the drying surface than the interior of the concrete specimens, the specimens are cut into 6 pieces with different length. The length is smaller near the surface and become larger as the distance from the drying surface is greater. The details of the size of the cut specimens are show in Fig. 3.10.

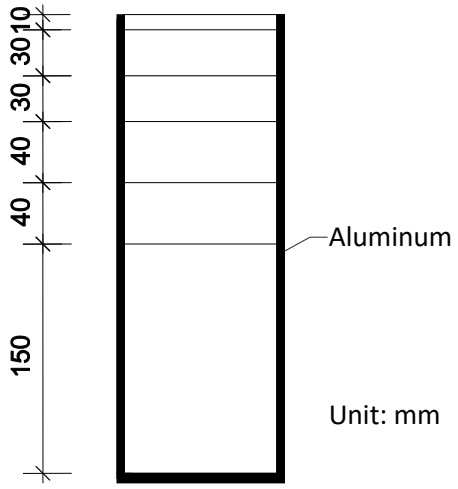

Fig. 3.10 Concrete specimens dimensions

There are three specimens for concrete drying experiment. Each specimen was cut into 6 segments with different length. The weights of those segments under saturated surface dry condition were firstly measured by the electrical scale with accuracy of 0.01 gram. Those segments were then combined again for drying. As shown in Fig. 3.10, the side and bottom of the cylinder specimen were sealed with aluminum tape to block water evaporation, while the top surface was exposed to the environment for drying in one direction. Each concrete segment was weighed after drying for 1, 3, 7, 14 and 27 days, respectively, and then combined again for further

drying. In the end of the drying experiment, those specimens were dried in the furnace with temperature of 105 °C for 7 to 10 days to attain their absolute dry weight. In this way, the water content at different depth from the drying surface for different drying time could be calculated. The results are shown in Fig. 3.11. The values of relative water content are used instead. The changing trend of water content in concrete specimens is basically consistent with the drying experiment of mortar specimens in Section 3.2.1. The water loss is most drastic at the depth of 5mm from the drying surface, while the drying process slows down at the depth larger than 55 mm.

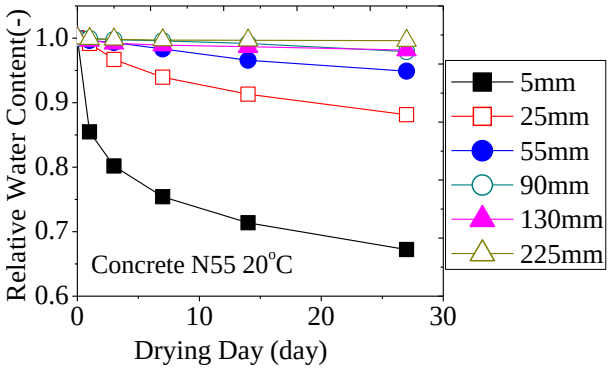

Fig. 3.11 Relative water content of concrete

Boltzmann-Matano method was applied to calculate WDC. The relationship between relative water content R and Boltzmann variable λ could be obtained by the regression the experimental data through the fitting function of Eq. (3.3). The experimental data and the regression results are shown in Fig. 3.12. And then the WDC at different water content were calculated by Eq. (3.2). The WDC in this concrete drying experiment are compared with the results of Sakata [1] and Akita [6] as shown in Fig. 3.13. The curve of WDC in this experiment is similar to that of Akita's result, and also in the same magnitude of Sakata's results. In other words, the WDC obtained in this experiment has the same trend as the results of Sakata [1] and Akita [6].

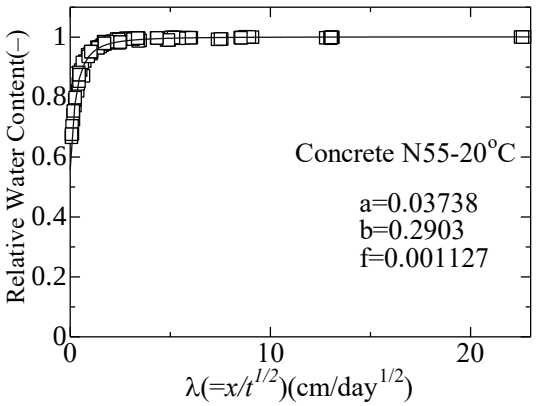

Fig. 3.12 Relationship of *R* and λ of concrete

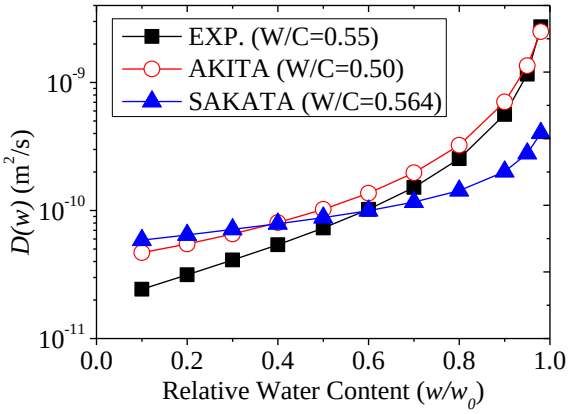

Fig. 3.13 Water diffusion coefficient of concrete

In this study, the influence of aggregate size on WDC is also evaluated. The drying experiment of concrete is compared with that of cement paste [7] and mortar. The water cement ratio for those experiments is identical, which is 0.55, and the drying temperature is also identical which is 20 ^{o}C. Those cement based materials have different aggregate size. The aggregate size of concrete is the largest, which is 20 mm. The aggregate size of mortar and harden cement paste is 2 mm and 0 mm, respectively. The relationship of WDC at different relative water content R and maximum grain size are plotted in Fig. 3.14.

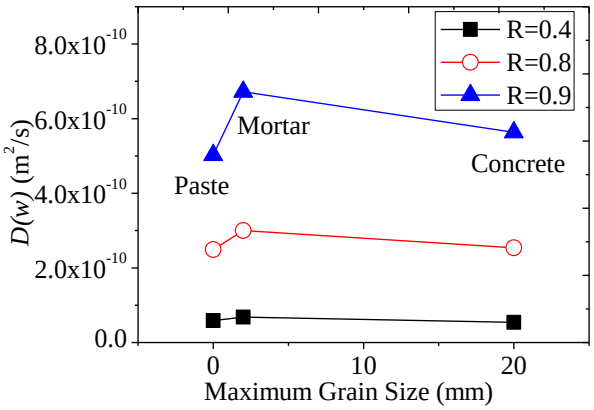

Fig. 3.14 Relation between maximum grain size and *D(w)*

According to the results of comparison, the WDC of mortar is the largest, while the WDC of concrete and cement paste are similar. The apparent relationship between aggregate particle size and WDC was not observed in this study. As is known to all, in interfacial transition zone, there are micro-cracking around aggregate, which could promote moisture transport. But in the case of concrete, when the aggregate size is relatively large, the path of water movement is extended, so the WDC of concrete becomes smaller than mortar.

3.3 Summary

Drying experiments of mortar and concrete specimens had been done in this chapter. The following conclusions were obtained:

(1) The temperature dependence of water diffusion and coefficient (WDC) was determined in the drying experiment of mortar specimens under different ambient temperatures. The higher temperature corresponds with the greater WDC. The temperature dependence of WDC conforms to power law.

(2) The WDC curve as a function of relative water content obtained by the drying experiment of concrete specimens in this study reproduces the results of previous studies.

(3) Due to the limitations of this study, there is no aggregate size dependence of WDC on the whole. The WDC of mortar is the largest, concrete the second, and paste the least. The increase of WDC in mortar can be explained by that there are more interfacial transition zones (ITZ) than paste. Concrete is also affected by the same ITZ effect, but because of the larger aggregate size, the path of water movement is extended. This could be the reason why the WDC of concrete is smaller than that of mortar.

(4) In general, WDC is not affected much by aggregate, so the moisture transport behavior is governed by harden cement paste during the first drying process. Temperature dependency of WDC of mortar obtained in this study could aid in predicting the drying rate in concrete, and resultantly contribute to the prediction or assessment of current state of concrete properties affected by drying, such as compressive strength, tensile strength and Young's modulus. The knowledge of moisture transport in harden cement paste could also be applied to the prediction of shrinkage-induced cracking in restrained concrete member.

References

1 K. Sakata, “A Study on Moisture Diffusion in Drying and Drying Shrinkage of Concrete”, Cement and Concrete Research, Vol. 13, Mar. 1983, pp. 216-224

2 Z.P. Bazant and L.J. Najjar, “Nonlinear Water Diffusion in Nonsaturated Concrete”, Materiaux et Constructions, Vol.5, 1972, pp.3-20

3 H. Akita, T. Fujiwara, and Y. Ozaka, “Water Movement within Mortar due to Drying and Wetting”, Proceedings of JSCE, No. 420, 1990, pp. 61-69 (In Japanese)

4 T. Fujiwara, K. Sato, and T. Konishi, “Water Movement within Concrete due to Drying and Wetting”, Review of 42 General Meeting, CAJ, 1988, pp. 427-430 (In Japanese)

5 T. Fujiwara, M. Kayaba and H. Akita, “Water Movement within Concrete due to Drying under Various Temperature Conditions”, CAJ Proceedings of Cement & Concrete, No.46, 1992, pp.428-433 (In Japanese)

6 H. Akita, T. Fujiwara and Y. Ozaka, “An Analytical Method of Moisture Transfer within Concrete due to Drying”, Proceedings of JSCE, No. 490, 1994, pp.101-110 (In Japanese)

7 I. Maruyama, G. Igarashi and N. Kishi, “Fundamental Study on Water Transfer in Portland Cement Paste”, Journal of Structural and Construction Engineering. Transactions of AIJ, No. 668, vol.76, Oct. 2011, pp.1737-1744 (In Japanese)

Chapter 4

Mechanism of Change in Splitting Tensile Strength of Concrete during Drying or Heating up to 90 ℃

4.1 Introduction

The establishment of performance assessment methods that examine the current state of concrete properties, and the establishment of predictive performance assessment methods are both essential to enable the long-term use of reinforced concrete structures. Changes in compressive strength of concrete during drying or heating up to 90 °C have previously been reported by Maruyama et al. [1]. That research demonstrated that concrete strength does not decrease uniformly with drying. Specifically, the compressive strength of concrete is influenced by the physical properties of the cement paste and the damage caused by volumetric change during drying of the paste and aggregate, and further cement paste, which combines porous and colloidal characteristics [2], exhibits various strength levels under drying conditions. Concrete with a W/C of 0.55 was found to have its lowest compressive strength at 40% RH. Under severer drying conditions, strength showed a tendency to increase, demonstrating strength development during drying. More details are presented in Section 2.2.1.

Considering such a multi-factor strength determination mechanism, it is quite unlikely that a high correlation between the compressive strength and tensile strength of concrete can be found as in the case of concrete of young age that is undergoing hydration [3, 4]. Therefore, the influences of drying and heating on splitting tensile strength should be investigated.

A previous study pointed out that splitting tensile strength of ordinary concrete is greatest in the vicinity of 60% RH during drying at room temperature [5]. Further, Kishitani et al. [6] reported that when exposed to a high temperature environment for 1000 days, the splitting tensile strength of concrete declined almost linearly with temperature in the range up to 100 °C. Based on the results of a comparison of micro-damage and exposure to high temperature, Kanda et al. [7] also reported a high correlation between damage and strength. A study by Naus et al. [8] observed also that tensile strength tends to decline monotonically in relation to temperature during long-term drying, but they found tensile strength to be extremely low in the range up to 100 °C when the period of exposure to high temperatures is short. The experimental results of the above-mentioned studies are presented in Section 2.2.2. However, according to the experimental results by Kishitani et al. [6], in order to clearly demonstrate the problems posed by the drying effect, it is important to perform testing in a state of full equilibrium where there is no water movement in the test specimens. This is because the differences in internal and external water distribution causes self-stress in the test specimens and has an impact as an error factor during measurement.

As concluded in Chapter 2, aggregate properties play an important role in strength

development of concrete under drying. In order to assess the impact of micro-damage around aggregate during drying, the influence of aggregate properties is also investigated by comparing concrete with a limestone aggregate, which is characterized by little shrinkage, and concrete with a sandstone aggregate, which is characterized by large shrinkage.

4.2 Experiment

4.2.1 Materials and mix proportions

The materials used in the experiments are listed in Table 4.1.The chemical composition and mineral composition of the cement are shown in Tables 4.2 and 4.3.The mix proportions of the mortar and concrete and the results of the fresh property test are shown in Table 4.4.

Table 4.1 Properties and characteristics of materials for experiments.

Cement	Notation	Properties and characteristics
Cement	C	Ordinary Portland cement, Density: 3.16g/cm^3, Blaine value: 3230cm^2/g
Fine aggregate	S	Land sand, Saturated and surface-dry density: 2.58 g/cm^3, Adsorption ratio:2.08%
Coarse aggregate	GLS	Limestone, Saturated and surface-dry density:2.64 g/cm^3, Adsorption ratio: 0.36%
	GSS	Sandstone, Saturated and surface-dry density:2.59 g/cm^3, Adsorption ratio: 0.89%
AE agent	AE	Complex of denatured lignin sulfuric acid compound and poly-carboxylic acid compound
Viscosity improver	AS	Cellulosic water-soluble polymer

Table 4.2 Chemical composition of cement.

LOI (%)	Chemical composition (mass%)								
	SiO_2	Al_2O_3	Fe_2O_3	CaO	MgO	SO_3	Na_2O	K_2O	Cl^-
2.3	20.04	5.21	2.87	64.9	1.46	2.21	0.14	0.34	0.019

Table 4.3 Mineral composition determined by X-ray/Rietveld analysis.

Mineral composition (mass%)							
C_3S	C_2S	C_3A	C_4AF	C$\underline{C}$	C$\underline{S}$ 2H	C$\underline{S}$ 0.5H	M
58.3±1.5	17.5±1.2	5.7±0.7	10.5±0.7	4.9±0.5	1.1±0.3	1.2±0.3	0.8±0.2

Table 4.4 Mixture proportions of concretes and properties of concretes at fresh state.

	Mixture proportions									Slump (cm)	Air (%)	Temp. (°C)
	W/C (%)	s/a (%)	Unit mass (kg/m^3)									
			W	C	S	GLS	GSS	AE	AS			
Mortar	55	—	271	492	1432	—	—	4.9	2	23	4.9	21
LS-S	55	51.8	177	322	940	909	—	3.2	1.3	6.5	2.9	21
LS-M										8.5	2.9	21
LS-L										11.5	2.8	21
LS-Mix										10.0	3.0	21
SS-S	55	51.8	177	322	940	—	892	3.2	1.3	6.5	2.6	20
SS-M										8.5	2.6	21
SS-L										9.5	2.5	21
SS-Mix										9.0	2.6	21

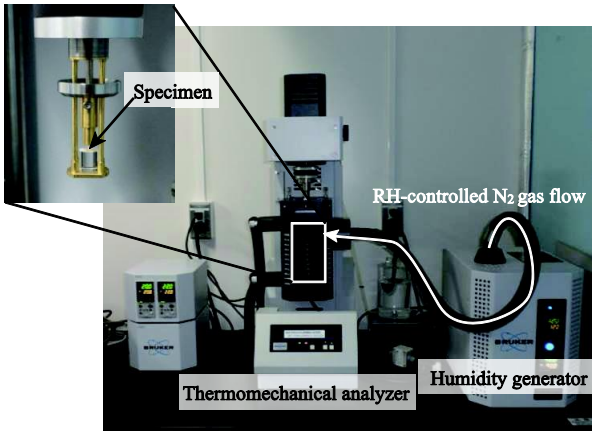

Fig. 4.1 Schematic of a system for measurement of length change isotherm of aggregates.

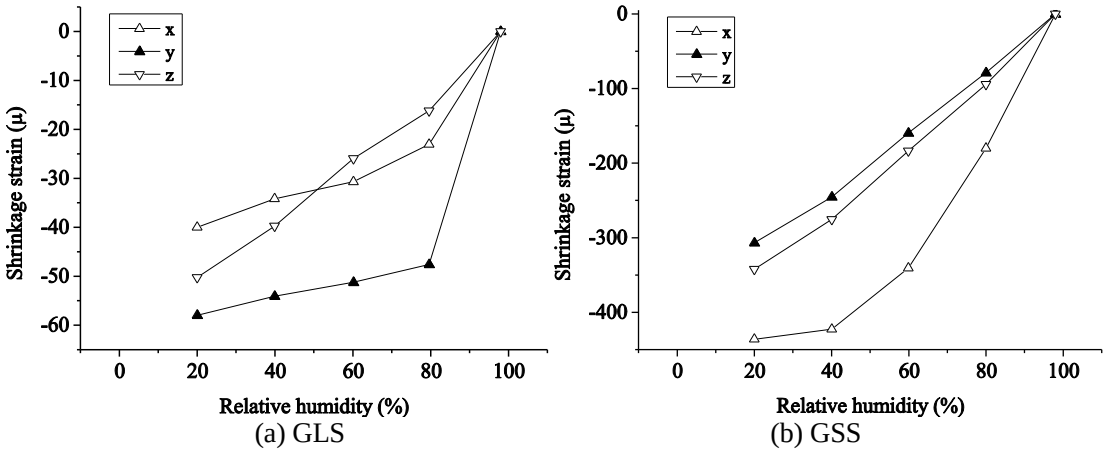

(a) GLS (b) GSS

Fig. 4.2 Relationship between drying shrinkage strain of coarse aggregate and relative humidity.

As the coarse aggregate for the concrete, crushed limestone aggregate (GLS), which has small drying shrinkage strain, and large crushed hard sandstone (GSS), which has large drying shrinkage strain, were used. Three orthogonal specimens each measuring 3×3×8 mm were cut from both types of aggregate, and the results of length change isotherm measurement using humidity-controlled thermomechanical analysis (TMA, Fig. 4.1) are shown in Fig. 4.2. The

temperature was controlled within 20±0.1 ºC.

Because aggregate size affects length change and damage around aggregate during drying (Maruyama et al. 2014a, Maruyama and Sugie 2014), coarse aggregate with grain sizes of 5-10 mm, 10-15 mm and 15-20 mm was used in equal parts by mass. The concrete specimens are designated as LS-Mix for concrete using crushed limestone aggregate, and SS-Mix for concrete using crushed hard sandstone.

Further, to assess the effect of aggregate size on drying, testing of concrete using exclusively GLS of either 5-10 mm, 10-15 mm, or 15-20 mm grain size was also conducted. These concretes were named LS-S, LS-M, and LS-L, respectively. Concrete using similarly graded GSS was named SS-S, SS-M, and SS-L, respectively.

In terms of mix proportions, the same volumetric proportions of coarse aggregate, water, cement, and fine aggregate were used for all concrete batches. Therefore, slump and air content were not adjusted. However, viscosity agent was used to suppress bleeding.

Batches of 80 L mixtures were produced by mixing each type in a 100 L pan type mixer for 3 minutes in a thermostatic chamber at 20 ±1 ℃.

The two types of concrete and mortar using different types of coarse aggregate were placed in φ100 × 200 mm lightweight molds and the cylinders were demolded after two days. Standard water curing was performed up to the age of 1 year under the constant temperature of 20 ± 1 ℃ in a saturated aqueous solution of calcium hydroxide. The choice of a saturated aqueous solution of calcium hydroxide was to prevent leaching of calcium from the specimens

The ø100×200mm mortar and concrete cylinders were then cut with a diamond cutter to a thickness of 9 mm to produce ø100×9mm specimens.

The specimens were dried at the constant temperature of 20 ℃ and humidity of 95% RH, 80% RH, 60% RH, 43% RH, and 20% RH, and were also heated in a constant-temperature furnace at 40 ℃, 65 ℃, and 90 ℃. Drying by saturated salt solutions was performed under the constant temperature of 20 ℃, and air circulation was performed in the chamber. To eliminate the effects of carbonation on the specimens under heating, heating was performed in a closed system in equilibrium with a saturated sodium hydroxide solution at room temperature. The schematic of the drying process is shown in Fig. 4.3. Both the inflow and outflow air around the specimens passed through a gas scrubbing bottle to eliminate the influence of carbon dioxide.

4.2.2 Size-dependence experiments

For faster drying, ø100× 9 mm disc-shaped specimens obtained by sawing ø100×200mm specimens were used in this study. Thereupon, the influence of specimen size on experimental results needs to be investigated.

Many studies have been conducted on the influence of specimen size on concrete strength, including assessment in terms of fracture mechanics [9] and assessment in terms of aggregate size

[10].

With regard to the influence of size in splitting tensile tests, Hasegawa et al. [11] reported that no size effect on specimen length was observed. Further, Tanaka et al. [12] reported that in the case of specimens with a diameter of 500 mm or greater, a size effect caused by the non-homogeneity of the material was observed, and that in the case of specimens with a diameter of up to 200 mm, a size effect caused by fracture energy exists. As described above, with regard to splitting tensile strength, a diameter size effect is recognized, but there is no agreement about the effect of length size. Therefore, in order to evaluate the size effect when using specimens of ø100 × 9 mm, splitting tensile tests on specimens of four different sizes, i.e. ø100 × 150 mm, ø100 × 100 mm, and ø100 × 50 mm in addition to ø100 × 9 mm, were conducted. The mix of the specimens was the LS-L type whose large and single sized coarse aggregate would show the size dependence of defects more clearly.

4.2.3 Influence of aggregate shrinkage

The effect of aggregate shrinkage was investigated for mortar, LS-Mix, and SS-Mix samples.

After cutting, the specimens were again subjected to standard water curing. Prior to the measurement, the specimens were wiped with a clean rag, and measurement of length and mass was performed in a water-saturated state. They were then placed under the specified drying or heating conditions, and the specimens were considered to have reached equilibrium when the change in mass of the specimens over 24 hours declined to 0.03% or less. After high-temperature drying, the specimens were sealed in aluminum bags and placed in a temperature-controlled room at 20 ℃ for three hours, and subjected to measurement of length and mass changes. Then the specimens promptly underwent splitting tensile strength testing with a universal testing machine.

Heated drying of the specimens was done using a hot-air circulation type heating chamber. To avoid carbonation, care was taken to supply CO_2 free air from a gas scrubbing bottle with a CO_2 absorbent as it is shown in Fig. 4.3. The drying period, which was longest for the humidity level of 43% RH, was 32 days for mortar and 36 days for concrete.

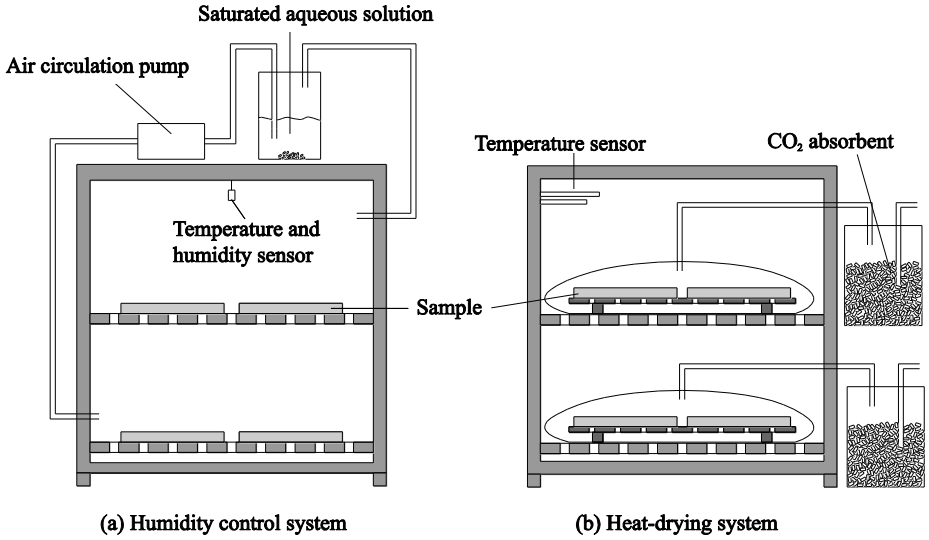

Fig. 4.3 Schematic of drying systems. Carbonation was prevented by CO_2 adsorbent or closed air circuit.

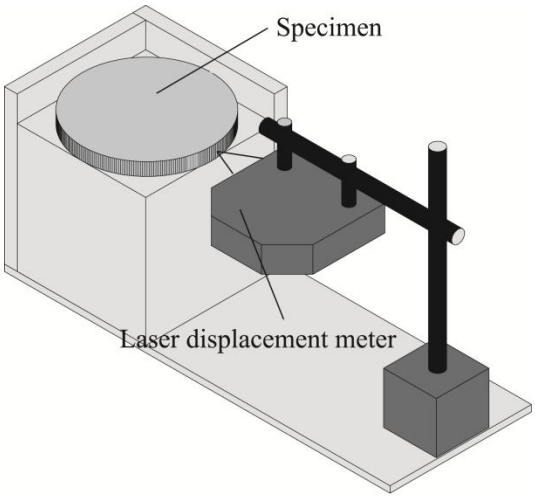

Fig. 4.4 Schematic of a measurement system for length of specimen.

Change in the length of the specimens before and after drying was measured with a laser displacement meter (1/2000 mm accuracy). The schematic of measurement process is shown in Fig. 4.4. The specimen temperature at drying shrinkage strain measurement was 20 °C. Stainless steel (SUS304) of a known length was provided and the length of each specimen was determined based on the length difference between the stainless steel and the specimen, and the drying shrinkage strain was calculated accordingly. It should be noted that because length of the stainless steel changes with temperature, the indoor temperature during measurement was also measured, and the necessary correction was performed using the thermal expansion coefficient of stainless steel of 17.0 $\times 10^{-6}$/℃. In addition, the diameter was measured in three places for each specimen, and the obtained values were averaged as the length of the specimen. Based on the change in length before and after drying, the shrinkage strain was calculated, using the pre-drying length as the base length.

The mass immediately after drying was measured using a precision balance (resolution: 0.0001 g). Following mass measurement, the samples were dried for 48 hours at 105 ℃ in a nitrogen flow until they reached equilibrium mass, and their water content was calculated from the change in mass before and after drying.

4.2.4 Effect of aggregate size

The effect of aggregate size was investigated through tests on LS-L, LS-M, and LS-S specimens and SS-L, SS-M, and SS-S specimens, comparing the LS-Mix and SS-Mix described in section 4.2.3. Specimen drying and water content measurement were performed using the same procedures as those described in section 2.4. After drying and the attainment of mass equilibrium, the splitting tensile strength was performed.

4.3 Results and discussion

4.3.1 Size effect

The splitting tensile test results for the various specimen sizes are shown in Fig. 4.5. Error bars of 1−sigma of measured variation are also shown. On the whole, specimen size shows no correlation with splitting tensile strength and standard deviation of strength, while the specimen with the smallest size has the smallest standard deviation. It was concluded that splitting tensile strength can be assessable even for ø100 × 9 mm specimens.

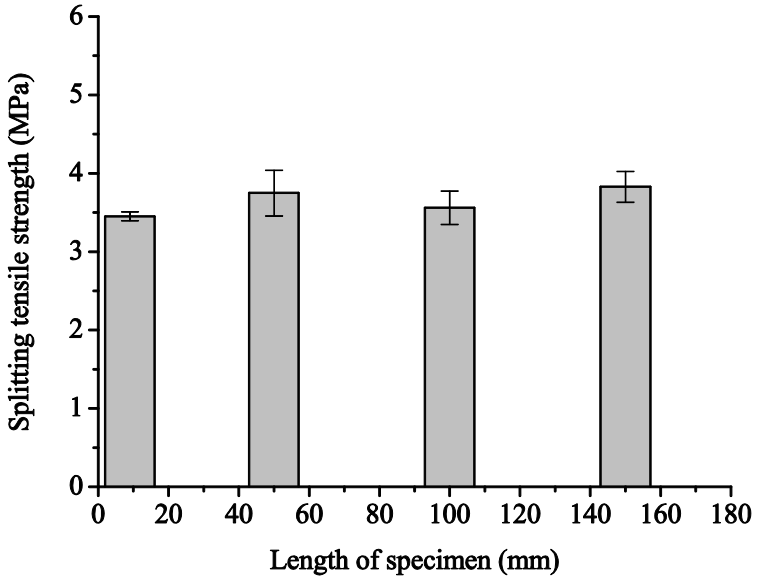

Fig. 4.5 Length size effect on splitting tensile strength. The samples were LS-L.

4.3.2 Influence of aggregate shrinkage on splitting tensile strength

4.3.2.1 Drying shrinkage strain and water content

Figure 4.6 shows the relationship between the equilibrium drying shrinkage strain and the drying conditions of the LS-Mix, SS-Mix, and mortar specimens. In each drying condition, the drying shrinkage strain of SS-Mix was greater than that of LS-Mix. Error bars of 1−sigma of measured variation are shown also in this figure, but they are all within the marker size. As shown in Fig. 4.2, the drying shrinkage strain at each relative humidity level is greater for SS-Mix using coarse aggregate. The fact that the drying shrinkage strain of coarse aggregate influences the drying shrinkage strain of concrete agrees with the existing research data and confirmed that shrinkage of mortar is constrained by coarse aggregate [13]. Figure 4.7 shows the evaporable water content of each concrete specimen. In the LS-Mix and SS-Mix specimens, differences in evaporable water content were observed in the RH range between 95% and 20%. This is considered to be the effect of dehydration of the clay minerals contained in SS-Mix.

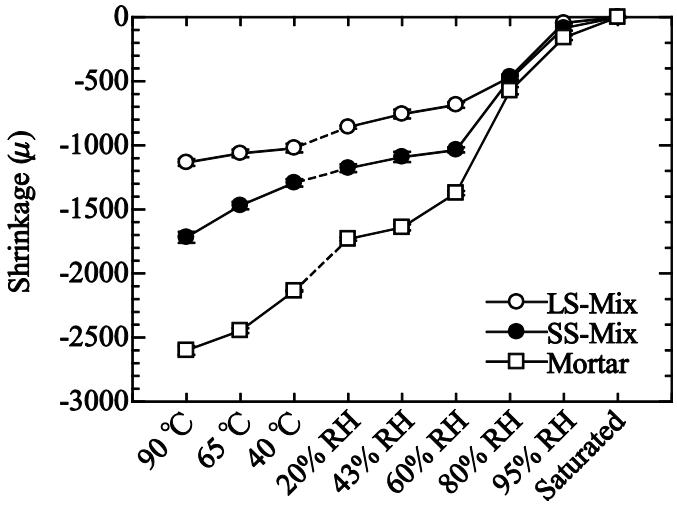

Fig. 4.6 Relationship between drying shrinkage strain and heating or drying condition. Error bars of 1−sigma of measured variation are shown but they are within the size of each marker.

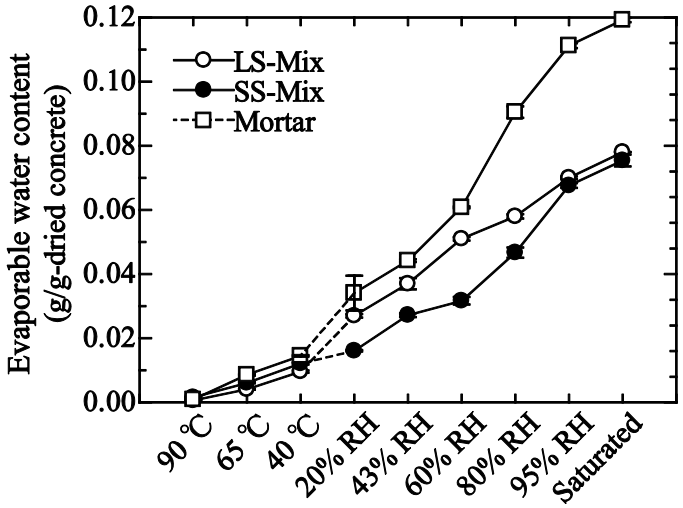

Fig. 4.7 Relationship between evaporable water content and heating or drying condition. Error bars of 1−sigma of measured variation are shown but they are within the size of each marker, except for LS-Mix 20% RH condition.

4.3.2.2 Strength

(1) Influence of the cement paste matrix

Figure 4.8 shows the relationship between the splitting tensile strength and drying conditions of each test specimen. For mortar, the splitting tensile strength increases from saturation to 60% RH, then decreases from 60% RH to 43% RH, then increases again from 43% RH to 20% RH, and reaches its highest value at 20% RH. In the case of drying by heating, strength declined gradually. Thus in the case of mortar, there is a non-monotonic relation between splitting tensile strength and drying conditions. Since such behavior has already been confirmed for cement paste, we checked the behavior trends of mortar against those of cement paste. Figure 4.9 compares the relationship between the normalized strength and drying conditions of mortar and cement paste. In this figure,

normalized strength is the ratio of the average value of the splitting tensile strength of the specimens for each drying condition to the average value of the splitting tensile strength of specimens in the saturated state. The data from bending tests was used for cement paste.

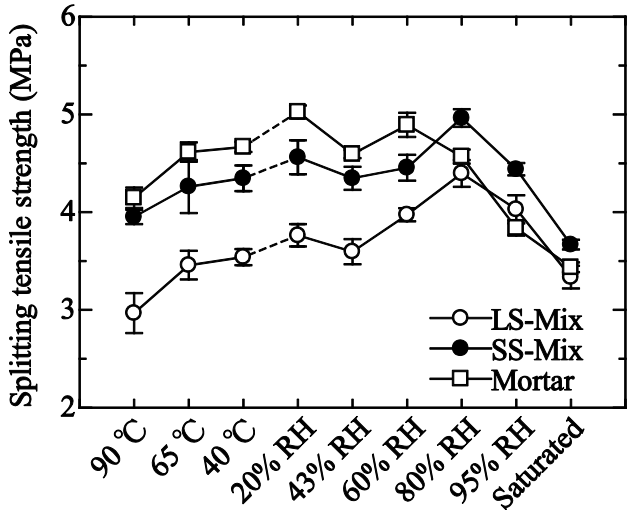

Fig. 4.8 Splitting tensile strength of mortar, LS-Mix, and SS-Mix as a function of heating or drying condition.

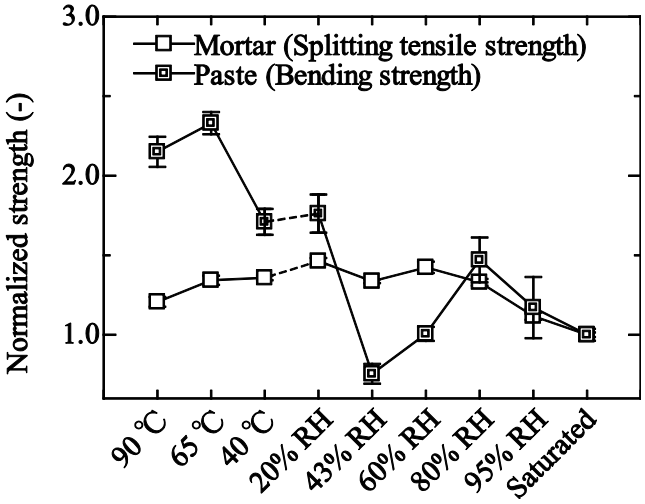

Fig. 4.9 Normalized strength of mortar and hardened cement paste as a function of drying or heating condition.(Paste data is cited from Maruyama et al. 2014b. Datum of paste at 65 ℃ is calculated as an average data of 60 and 70 ℃. And Datum of paste at 43% is assumed to be same as that at 40% RH.).

An examination of the results in accordance with the drying process from the saturated state indicate that the paste showed an increase in strength in the range up to 80% RH, and that after reaching the maximum value, the strength declined until 40% RH. On the other hand, in the case of mortar, the strength increased until 60% RH. Two things can be considered to be at work here, namely (1) the multiplication of crack development paths during fracture owing to the role of fine aggregate, which causes an increase in strength as the result of increased energy consumption

during fracture, and (2) the fact that the alteration process of the paste in the mortar may not have fully run its course due to the limited drying period of about 30 days. However, as regards the phenomenon of the strength value reaching its maximum value once through drying from the saturated state, the influences of the strength increase behavior of cement paste arising from the precipitation of hydrates associated with drying and physical and chemical bonding among hydrates are considered to be dominant [2].

This influence of the incorporation of fine aggregate agrees with the fact that almost no strength reduction due to drying after the maximum strength value is reached can be seen in mortar. In the case of cement paste, the minimum strength value is reached at 40% RH (in the case of mortar in this study, 43% RH), and the amount of decrease of splitting strength of mortar is extremely small. This is assumed to be due to the increase in apparent strength caused by the formation of some cracks around the fine aggregate, which makes it easy for multiple cracks to appear under loading.

Strength of cement paste tends to increase under drying conditions more stringent than 40% RH [2]. This is due to the fact that calcium silicate hydrate interlayer distance becomes shorter, C-S-H densifies, and the strength of solids increases. The strength of mortar tends to be almost similar to that of cement paste.

The gradual decline of strength after it reaches its maximum value is caused by the expansion of crack width as the result of the increased shrinkage of the paste, and dehydration and decomposition of the aluminate hydrate in the paste at temperatures of 65 °C or higher [2].

(2) Influence of aggregate shrinkage

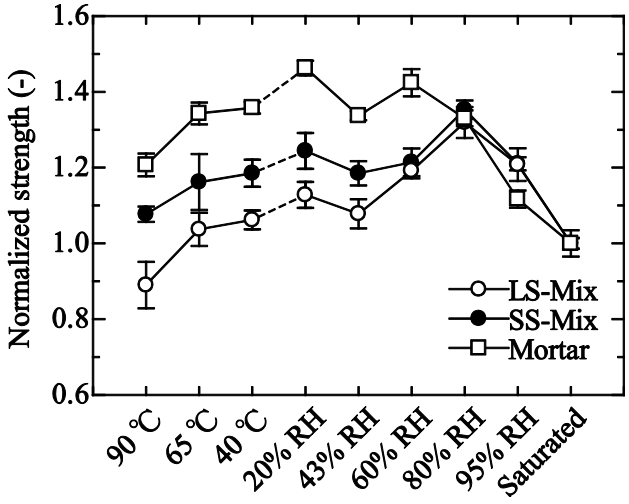

Fig. 4.10 Normalized strength of mortar, LS-Mix, and SS-Mix as a function of heating or drying condition.

Fig. 4.10 shows the relationship between normalized strength and drying for LS-Mix, SS-Mix, and mortar specimens. In the case of both LS-Mix and SS-Mix, splitting tensile strength increases from saturation to 80% RH, then declines until 43RH%, and from 43% RH to 20% RH,

it increases slightly. While this behavior is largely similar to that of cement paste, it differs slightly from that of mortar. The behavior from saturation to 80% RH is similar to that of mortar, and the rate of strength increase is also the same. Thus the strength increase trend of SS-Mix and LS-Mix in this region can be said to be due to the influence of the mortar. However, the trend from 80% RH to 43% RH differs among mortar, SS-Mix, and LS-Mix. In other words, the restraining effect of coarse aggregate in that range is considered to be large. In fact, as can be seen in Fig. 4.6, in that humidity range, large differences in drying shrinkage strain of concrete appear, and differences in restraint dependent on aggregate shrinkage, in other words, the influence of damage around the aggregate, are considered to dominate [1].

The strength increase in the range from 43% RH to 20% RH follows the same trend for mortar, SS-Mix, and LS-Mix, but the fact that the rate of increase is smaller for concrete than for mortar is due to the smaller amount of mortar that is effectively working in the load transfer path contributing to strength increase through the damage that has already occurred around the aggregate [1].

In the drying range from 20% RH to 90 °C, the rate of strength decrease of LS-Mix is larger than that of SS-Mix, and that amount is either comparable to that of mortar or slightly smaller. In any case, the strength reduction behavior of mortar dominates that of concrete.

Looking these behaviors from the perspective of the damage that accumulates in concrete, clear differences in strain can be seen between concrete and mortar as shown shrinkage strain graph in Fig. 4.6. Because the strain of mortar with the same mix proportions as that of the mortar used in the concrete is shown, this significant difference in strain between concrete and mortar is believed to be caused by the restraining effect of aggregate. On the other hand, taking into account the fact that this is strain at the equilibrium state, the strain of the mortar in concrete has to be the same as the strain of the mortar specimen. Because the tensile strength of mortar is on the order of several MPa, a large number of cracks can be assumed to occur in mortar restrained by aggregate. That is to say, many cracks occur in mortar under the restraining effect of the aggregate in concrete, which results in the creation of voids. If the elastic tensile strain of the mortar is ignored, the amount of voids ought to be in a linear relationship between the strain differences between concrete and mortar. Based on this concept, the strain difference between mortar and concrete has been defined in a past research [1] as gap strain, which is a measure of the amount of damage. The gap strain in this study is indicated in Fig. 4.11. As shown in the figure, in the range from saturation to 80% RH there is virtually no difference in the damage to the mortar portion of the concrete for LS-Mix and SS-Mix, and in the range from 80% RH to 43% RH, that difference expands, and in the drying range from 43% RH to 20% RH, the increase in the amount of damage is almost the same, and further, in the drying range from 40 °C to 90 °C, the amount of damage increases for LS-Mix.

These results correspond to the large increase in normalized strength for LS-Mix and SS-Mix in the range from 80% RH to 43% RH, and the growing decline in strength for LS-Mix in that

same range.

Further, the fact that strength reduction in the range of 40 °C to 90 °C is greater for LS-Mix than for SS-Mix can be interpreted as being caused by expansion of damage.

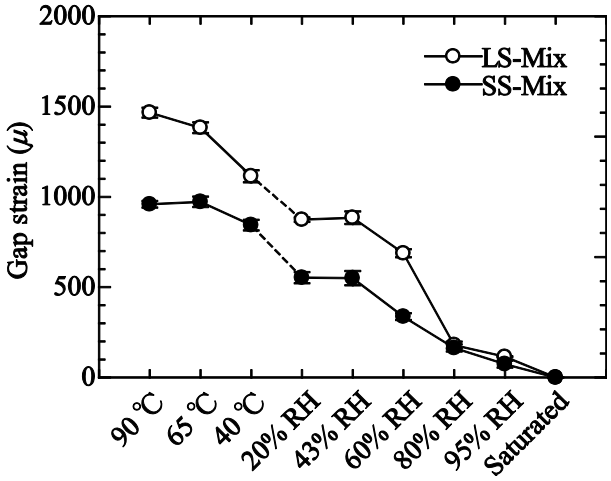

Fig. 4.11 Gap strain, which is defined by the difference between mortar and concrete drying shrinkage strain, and drying or heating condition.

4.3.3 Influence of aggregate size on splitting tensile strength

Figure 4.12 shows the water content under various heating or drying conditions, where the differences in water content between the concretes using LS, as well as using SS, were not large.

Figure 4.13 shows the splitting tensile strength results. The splitting tensile strength in the saturated state was largely the same for LS and SS, on the order of 3.5 MPa. Overall, mortar strength displayed similar trends to those of LS-Mix and SS-Mix. In other words, strength increased in the range from saturation to 80% RH, then declined until 43% RH, and increased slightly at 20% RH. After that, strength declined along with the rise in temperature in the heated drying range of 40 °C on up.

Now looking at the LS series, the strength of LS-L at 80% RH was about 0.5 MPa lower compared with LS-Mix, LS-S, and LS-M. This is thought to be due to the fact that LS-L has already developed cracks around the aggregate by the time it undergoes drying. Because in the case of large aggregate, the effect of the transition zone surrounding the aggregate being relatively small, cracks may easily occur even at moderate dryness [14]. This is thought to be why the strength of LS-L became smaller at 80% RH. The relationship between drying and strength after that was equivalent between LS-M and LS-Mix, and as discussed in section 3.2, the number of cracks that occurred during drying being determined over the humidity range especially from 80% RH to 60% RH, it became clear that the cracks that occur in the high humidity range have a greater influence on the strength behavior during drying. In the case of LS-L as well, the strength declined below the value at saturation during drying at 65 °C and higher.

On the other hand, looking at the SS series, the strength was highest for SS-Mix at 80%

RH. SS-S, SS-M, and SS-L all had strength about 0.5 MPa lower at that humidity level. Although the reason for this is unknown, it might be that distribution of cracks occurs to a greater extent for continuously graded aggregate, which might have prevented a marked decline in strength. Looking at drying at 60% RH, only LS-L showed lower strength by about 0.5 MPa, and similarly to the LS series, only SS-L continued to consistently show lower strength in the subsequent drying.

Comparing the SS series and the LS series, we see that the SS series exhibited greater strength increase at 80% RH, and that after that the strength decline trend was almost the same for both series. As a result, the strength of the SS series during drying up to 90 °C did not fall below the strength at saturation.

As described above, the size of aggregate used in concrete does not have a significant effect on strength at saturation, but it does affect strength during subsequent drying. This effect is particularly pronounced in the range from saturation to 60% RH due to the restraining effect of mortar shrinkage, and the strength at 80% RH varies depending on aggregate size. Even during drying at humidity below 60% RH or heated drying, the strength reduction amount was found to be slightly greater for large aggregate.

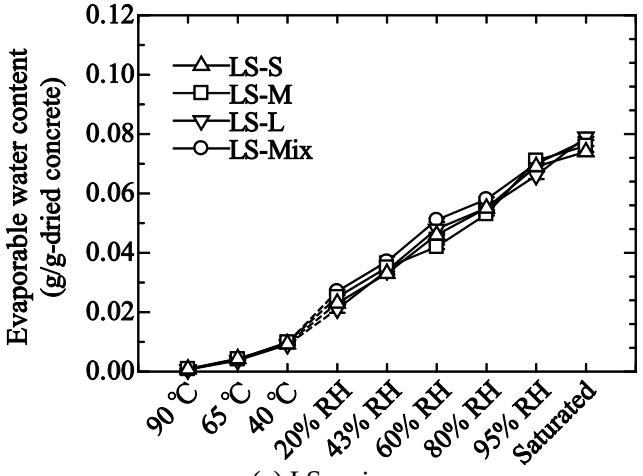

(a) LS series

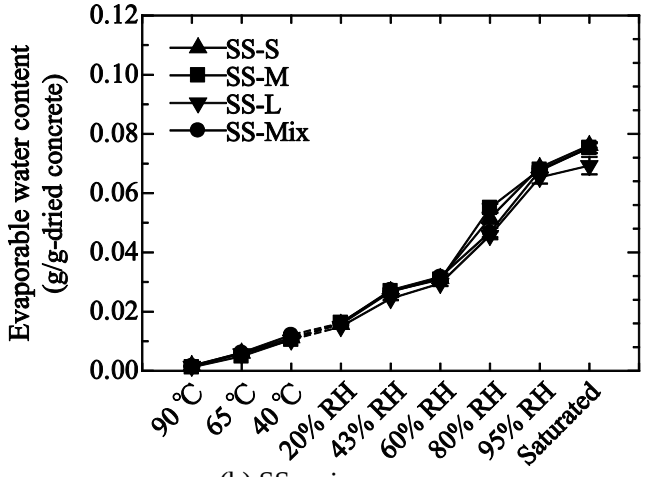

(b) SS series

Fig. 4.12 Evaporable water content of LS-S, LS-M, and LS-L (a), and SS-S, SS-M, and SS-L (b) under different heating or drying conditions.

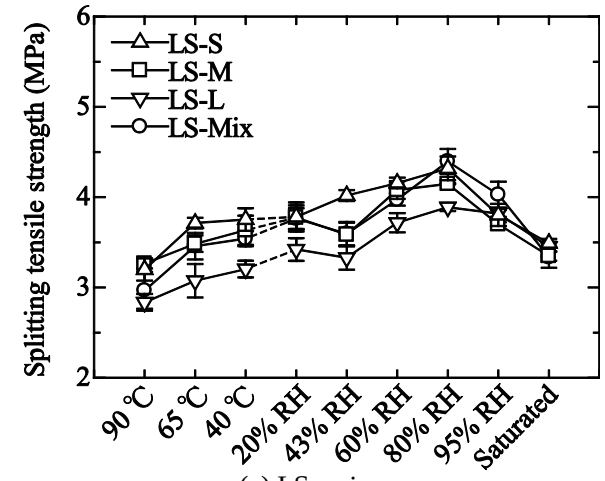

(a) LS series

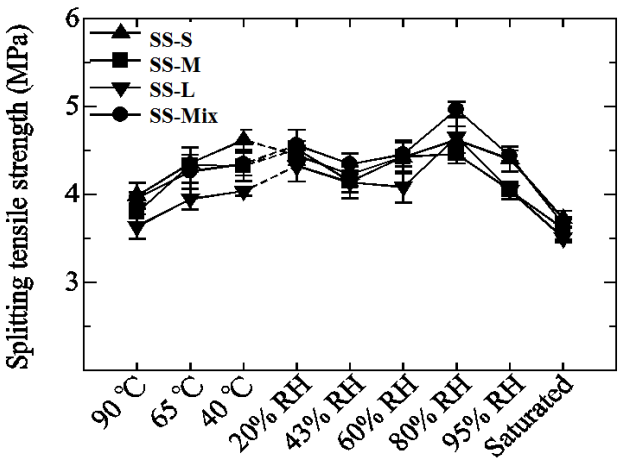

(b) SS series

Fig. 4.13 Splitting tensile strength of (a) LS-S, LS-M, and (b) LS-L, and SS-S, SS-M, and SS-L under different heating or drying conditions.

4.3.4 Notes on strength assessment for aging management

The splitting tensile strength of concrete, used as the cracking strength as well as to assess shear cracking strength, is one of the important parameters for aging control. As a design strength, splitting tensile strength is often expressed as a function of compressive strength. Because this relationship is valid at saturated conditions, these design formulas are not necessarily appropriate for the evaluation of concrete performance after drying.

Moreover, the obtainment of this property value through core sampling from existing buildings and subsequent loading test is anticipated as a direct method. However, because most core sampling is carried out using the wet core sampling method, attention should be paid that the strength data acquisition is done under conditions that differ from the ordinary strength conditions in the building. Particular attention is in order when acquiring data in a high-temperature drying environment.

Separate consideration of the core sampling acquisition method and how the obtained data is

to be interpreted is necessary. Further analytical studies of these questions are planned in the future.

4.4 Summary

This study has discussed the splitting tensile strength change mechanism for mortar with a water-cement ratio of 0.55 and concretes using aggregate with different amounts of shrinkage under various drying conditions.

In the case of mortar, the strength changed along with drying, but the trend was not uniform. In a 20 °C environment, the strength reaches its highest value at 60% RH, while in the range from 43% RH to 20% RH, there was a slight increase in strength. This trend was strongly influenced by the strength change of the cement paste, and was also attributed to the effect of an increase in apparent strength due to multiple cracks in the presence of fine aggregate.

Besides being affected by changes in mortar strength, concrete is influenced also by fine cracks caused by coarse aggregate restraint. The decline in strength due to the fine cracks formation as the result of the restraining effect of coarse aggregate on cement paste was particularly pronounced in the range from 80% RH to 43% RH. The impact of the restraining effect of aggregate was also seen in the range from 40 °C to 90 °C. In the case of aggregate prone to high shrinkage with shrinkage behavior similar to that of mortar, the damage was lesser, and thus the decline in strength was smaller in the range from 80% RH to 43% RH. On the other hand, in the case of aggregate with low shrinkage, the decline in strength was higher in that range. As a result, under the drying condition of 90 °C, which produced a decline in strength, the strength value was lower than that at saturation. Further, in the case of large aggregate size too, the restraining effect of such aggregate affected changes in splitting tensile strength during drying. As a result, tensile strength at 90 °C was likely to be smaller than that at saturated condition.

The splitting tensile strength of concrete changes during drying, but in the range up to 65 °C, the splitting tensile strength does not fall below the value at saturation and remains high regardless of the drying condition.

Assuming that the wet method is used for core sampling for the purpose of strength assessment during maintenance, how the test results should be positioned is a question that warrants discussion.

References

.

1 I. Maruyama, H. Sasano, Y. Nishioka and G. Igarashi, "Strength and Young's modulus change in concrete due to long-term drying and heating up to 90 ℃." Cement and Concrete Research 66(2014), 48-63.

2 I. Maruyama, Y. Nishioka, G. Igarashi and K. Matsui. "Microstructural and bulk property changes in hardened cement paste during the first drying process." Cement and Concrete Research 58(2014), 20-34.

3 Comité Euro-International du Béton. "CEB-FIP Model Code 90", 1993, Thomas Telford.

4 Japan Concrete Institute, "Guidelines for Control of Cracking of Mass Concrete 2008". Tokyo, 2008, Japan Concrete Institute.

5 J. A. Hansen, "Effects of curing and drying environments on splitting tensile strength of concrete." Journal of the American Concrete Institute 65 (1968), 535-543.

6 K. Kishitani, H. Kasami, F. Oshida and T. Okuno. "Properties of concrete exposed to 20~300℃, Part 1 and 2." Summaries of technical papers of Annual Meeting Architectural Institute of Japan, Structure 57 (1982), 317-320.

7 T. Kanda, Y. Ichikawa, O. Kontani, M. Takeda and K. Otsuka. "Experimental investigation of concrete damaged by exposuring to high temperature and low humidity environment." Journal of structural and construction engineering(615), 2007, 15-22.

8 D. J. Naus, "A compilation of elevated temperature concrete material property data and information for use in assessments of nuclear power plant reinforced concrete strucutres, NUREG/CR-7031, 2010, US-NRC.

9 Z. Bažant, "Size Effect in Blunt Fracture: Concrete, Rock, Metal." Journal of Engineering Mechanics 110(1984), 518-535.

10 Y. Tanigawa, Y. and K. Yamada. "Size effect in conpressive strength of concrete." Transactions of the Architectural Institute of Japan(262), 1977, 13-21.

11 T. Hasegawa, T. Shioya and T. Okada. "Size Effect on Splitting Tensile Strength of Concrete." Proceedings of Japan Concrete Instituite(7), 1985, 309-312.

12 Y. Tanakaand J. A. den Uijl, "Probabilistic analysis of size effect of splitting tension test." Proceedings of the Japan Concrete Institute 30(3), 2008, 49-54.

13 T. Fujiwara, "Effect of Aggregate on Drying Shrinkage of Concrete." Journal of Advanced Concrete Technology 6(1), 2008, 31-44.

14 I. Maruyama and A. Sugie. "Numerical Study on Drying Shrinkage of Concrete Affected by Aggregate Size." Journal of Advanced Concrete Technology 12(8), 2014, 279-288.

Chapter 5
Impact of Aggregate Properties on the Development of Shrinkage-Induced Cracking in Concrete under Restraint Conditions

5.1 Introduction

Cracking in concrete produced by drying shrinkage is an undesirable phenomenon since it causes disfigurement of building surfaces and jeopardizes the durability of concrete by facilitating the ingress of water, carbon dioxide, and other aggressive substances. Hence, the shrinkage mechanism of cement paste [1-10], aggregate properties and their restraint performances in concrete [11-20], the effect of aggregate particle size on shrinkage [11, 21-23], water movement behavior [17, 24-32], and formulae to predict drying shrinkage of concrete based on mixture proportions and environmental conditions [33, 34] have been thoroughly studied. Due to the high volume ratio of aggregates in concrete, the impact of aggregate properties on concrete shrinkage has gained fresh attention in recent research, consequently leading to more intense investigations.

Meanwhile, the behavior of concrete under restraint conditions has not been characterized as well as its behavior under free conditions. While numerous studies on cracking behavior and criteria for the initiation of through-cracking criteria have been conducted [35-40], in general, restrained concrete shows a complex behavior during the drying process. Concrete members contain a gradation of water content, which results in intrinsic shrinkage strains that are mutually restrained by each other within each concrete member and by an outer restraining body. Considering this inhomogeneity of stress in concrete members, the majority of the research has focused on engineering or design purposes but not on better understanding of material characteristics. Thus, in addition to through-cracking, the initiation of cracking and the propagation process at the meso-scale (scale from micrometer to millimeter) should be studied.

As shown in Section 2.3.1, a series of concretes that had the same volumetric mixture proportions except for coarse aggregate type showed different numbers of through-cracks in reinforced concrete prism specimens under restraint conditions while differing in minor surface cracking [41, 42]. Fig. 2.27 presents a comparison of surface crack patterns in concrete with different coarse aggregates. Concrete with limestone which has small shrinkage shows a smaller number of through-cracks and a larger number of surface cracks than concrete with sandstone as the aggregate.

The main driving force of concrete shrinkage is the cement paste. A similar amount of cement paste is used to make concrete with limestone and sandstone aggregates. Therefore, it can ignore the role of the cement paste and allows an isolated comparison of the shrinkage caused purely by the aggregates. Under restraint conditions, concrete members produce internal stresses while the expected stresses in concretes with different aggregates are similar, but their cracking behaviors are quite different. While a concrete mix with a limestone aggregate had a small number of through-cracks and a large number of minor surface

cracks, concrete with sandstone aggregates exhibited the opposite behavior [43]. In other words, the shrunk volume of concrete is differently apportioned to through-cracks and minor/micro cracks depending on the aggregate used.

The cracking behavior of concrete is generally considered to be highly complex. Studying aggregate-dependent crack initiation can lead to a better understanding of this phenomenon and aid in formulating mechanisms to control cracking.

Although crack propagation due to drying is difficult to observe experimentally, a measurement method for crack propagation using a digital image correlation method (DICM) has been developed recently to overcome this issue [44]. In the present study, a waterproof coating was firstly applied on the surface of concrete specimens to determine crack proportions in fabricated concrete walls, as well as to provide the background color for the DICM analysis. Secondly, as comparing numerical simulations with experimental data is quite informative [18, 19, 45, 46], rigid-body-spring networks (RBSN) [47-49] were applied to reproduce trends of crack initiation and propagation behavior in order to understand the impact of aggregate properties on these processes.

5.2 Experimental Techniques

5.2.1 Materials

Two concrete specimens with different shrinkage properties were prepared with a water-to-cement ratio of 0.55 using ordinary Portland cement whose properties are summarized in Table 5.1. The differences in shrinkage properties were realized by using two different coarse aggregates, namely limestone (GL) and sandstone (GS). GL is very pure limestone and shows almost no shrinkage, whereas GS has a large amount of chlorite and shows large shrinkage. Short-term length change isotherms of GL and GS in three orthogonal directions [50] are reproduced in Fig. 5.1. We denote concrete containing GL and GS as LS and SS in this study, respectively. Concrete mixture proportions of LS and SS were designed to keep the unit volume of coarse aggregate constant in order to isolate the effect of aggregate properties on the total shrinkage. In addition, in order to eliminate size effects due to differences in particle size distribution, each aggregate was firstly screened with sieves of 5 mm to 10mm, 10 mm to 15mm, and 15 mm to 20mm, and then the three grades of aggregates were mixed uniformly. It should be noted that all the aggregates are prepared in saturated surface dry conditions before mixing. Viscosity improver was used to avoid bleeding and evade any changes in concrete quality; hence, fluidity was not controlled in this mix design. Details of the materials used are listed in Table 5.2. The mix proportions of concrete and their respective fresh properties are listed in Table 5.3 and the properties of the aggregates are listed in Table 5.4. The details of the experiments carried out to study aggregate properties are introduced in Section 5.2.2. Note that concrete specimens were demolded at the age of one day and subjected to underwater curing using a saturated calcium hydroxide solution at a temperature of 20℃ ±2℃ for one year to avoid additional progression of hydration during the subsequent tests.

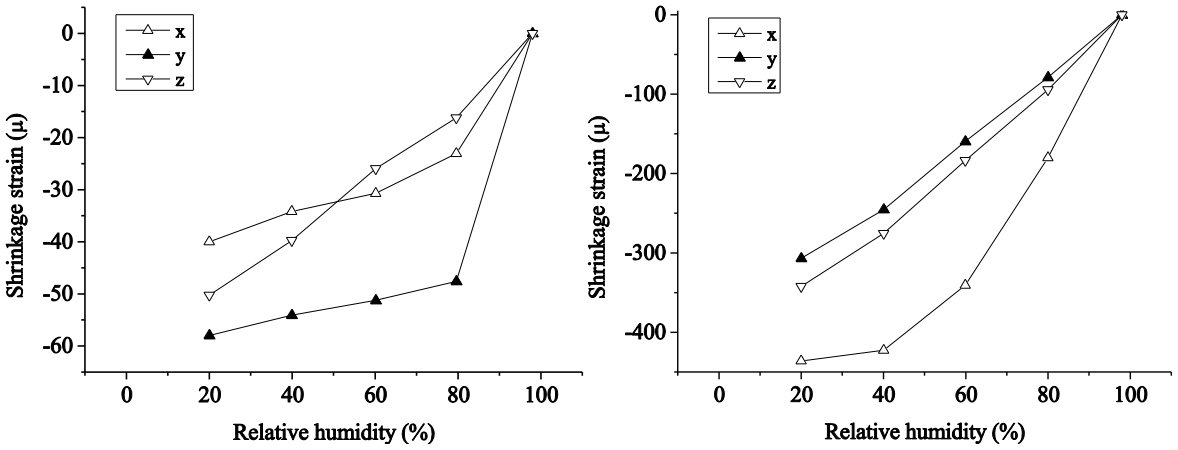

(a) GL (b) GS

Fig. 5.1 Short-term length-change isotherms of GL and GS.

Table 5.1 Materials used.

Material	Notation	Properties
Cement	C	Ordinary Portland cement, density: 3.16g/cm^3, Blaine surface area: 3230cm^2/g
Fine aggregate	S	Ooi river sand, density at surface dry condition: 2.59g/cm^3, absorption: 2.08%
Coarse aggregate	GL	Limestone, density:2.64g/cm^3, absorption: 0.36%
	GS	Crushed sandstone, density:2.64g/cm^3, absorption:0.89%
Agent	AE	AE water reducing agent, polycarboxylic acid type
Agent	AS	Thickening agents, water-soluble cellulose type

Table 5.2 Chemical composition of cement

	ig.loss (%)	Chemical composition (mass%)								
		SiO_2	Al_2O_3	Fe_2O_3	CaO	MgO	SO_3	Na_2O	K_2O	Cl^-
N	2.3	20.04	5.21	2.87	64.9	1.46	2.21	0.14	0.34	0.019

Table 5.3 Mix proportions and fresh properties of concrete

	Mixture proportion									Slump (cm)	Air (%)	Temperature (℃)
	W/C (%)	s/a (%)	Mass (kg/m^3)									
			W	C	S*	GL*	GS*	AE	AS			
LS	55	51.8	177	322	940	909	-	3	1.3	11.5	2.8	21
SS			177	322	940	-	892	3	1.3	9.5	2.5	21

* Aggregates are in the saturated surface dry condition.

Table 5.4 Physical properties of aggregate.

	Drying shrinkage from saturated state to 60% RH equilibrium *1	Bulk modulus*2
GL	-36μ	71.1GPa
GS	-230μ	40.8GPa

*1 Average of three orthogonal strains obtained with a thermal mechanical analyzer with a relative humidity generator (Bruker AXS, TMA4000SA + HC9700). Length-change isotherms are shown in the Appendix.

*2 Calculated using ultrasonic pulse velocity of P-wave and S-wave and density of aggregates. Average of three orthogonal values.

5.2.2 Aggregate properties

Short-term length change isotherms of the aggregates were determined with a humidity-controlled thermo-mechanical analyzer (BrukerAXS TMA4000SA with HC9700) to study volume changes of the aggregates. Three samples with dimensions of 3 mm × 3 mm × 6 mm were cut from each aggregate specimen with a diamond saw in three orthogonal directions taking into account their anisotropy. The original aggregates were the largest among the aggregate batches. Length changes were measured with specimens placed under controlled RH levels of 80%, 60%, 40%, and 20% at 20 ℃ for four hours. A linear variable differential transformer with a precision of 0.5 μm, a resolution of 0.0025 μm, and a contact load of 0.098 N was used to measure changes in the lengths of the samples.

One sample was analyzed for each direction and each aggregate type; therefore, the experimental results cannot be considered as being representative values. Despite this, the results confirm a difference in shrinkage properties between LS and SS.

The Young's modulus and Poisson's ratio of the aggregates are also considered an important factor for preventing large shrinkage of the cement paste [11]. Therefore, these values were calculated by measuring the ultrasonic velocity of the aggregates. Ultrasonic pulse velocities of the P-wave (longitudinal elastic wave) and the S-wave (transverse elastic wave) of water-saturated aggregate samples were measured using an ultrasonic probe (V103-RM and V153-RM, Panametrics-NDT), and a pulsar-receiver (5077PR, Parametric-NDT). The voltage of the pulse oscillator was -400 V, the frequency was 1.0 MHz, and the pulse repetition frequency was 100 Hz for the transmission method. The width of the samples was measured as being 10 mm with a digital micrometer caliper with an accuracy of 0.020 mm. Reference curves were obtained by direct contact, and the period of the pulse peak in the reference curve was subtracted from the period of the pulse peak in the sample record to determine the propagation time. The pulse velocities of the P-wave (V_p) and S-wave (V_s) were calculated from the sample width and propagation time. Using the saturated aggregate density (ρ), Poisson's ratio (v) and Young's modulus (E) were determined by using V_p and V_s according to the following equations:

$$\nu = \frac{1 - 2\left(V_s / V_p\right)^2}{2 - 2\left(V_s / V_p\right)^2} \qquad (5.1)$$

$$E = V_p^2 \rho \frac{(1+\nu)(1-2\nu)}{1-\nu} \qquad (5.2)$$

Sample width and propagation time were measured for three times for each sample, and the results were averaged. The calculated values of Poisson's ratio and Young's modulus of three samples were averaged.

One aspect of the background of this experiment is addressed here. The dynamic measurement result for the modulus of elasticity does not always correspond to the static loading result, and the value obtained by the dynamic method is generally larger than that obtained by the static loading test [51]. This is generally explained by the presence of fine cracks in the rock and this tendency is likely to be found in cases where the specimen size is large. The static loading test is more suitable than the dynamic method; however, due to size limitations, the dynamic method was selected to consider the properties of the aggregate.

5.2.3 Unrestrained shrinkage experiment

Strain distribution in a section of a concrete specimen during the drying process was evaluated by DICM, accompanied by linear deformation and mass change measurements. In the present study, we focused on the section perpendicular to the drying surface, and thus a water vapor impermeable coating to the sides of the specimens was applied.

Concrete samples were placed in a steel mold with a diameter of 100 mm and a height of 200 mm. After a one-year curing period, disks with a diameter of 100 mm and a height of 9 mm were cut out by a diamond saw. Two circular surfaces were coated with a two-part epoxy resin (Kikusui primer EPW, Kikusui Co.) to form a white vapor impermeable film as shown in Fig. 5.3. Preliminary testing, which constituted of periodic mass change measurements of a concrete sample fully coated by this resin, confirmed that the coating was sufficiently impermeable to water vapor and elastic enough not to affect the volume change of concrete. The details are introduced below.

The impervious coating used in this study is compared with the normal concrete surface by evaporation mass per surface area. Environmental conditions during the experiment were 20 ℃ and 60±5% RH. The coating material itself also showed some mass change under these conditions and the material coated on the metal surface was also measured. The results are summarized in Fig. 5.2. Based on this figure, approximately 94% of vapor evaporation from the concrete surface was prevented until 150-day-drying by using the coating material. The slower evaporation rate introduced a smaller water content gradient in the specimen and can mitigate cracking on the concrete surface due to large shrinkage differences derived from a steep water content gradient.

For this reason, the impact of water vapor evaporation from the coating is considered as negligible for surface cracks caused by the internal restraint in the present study.

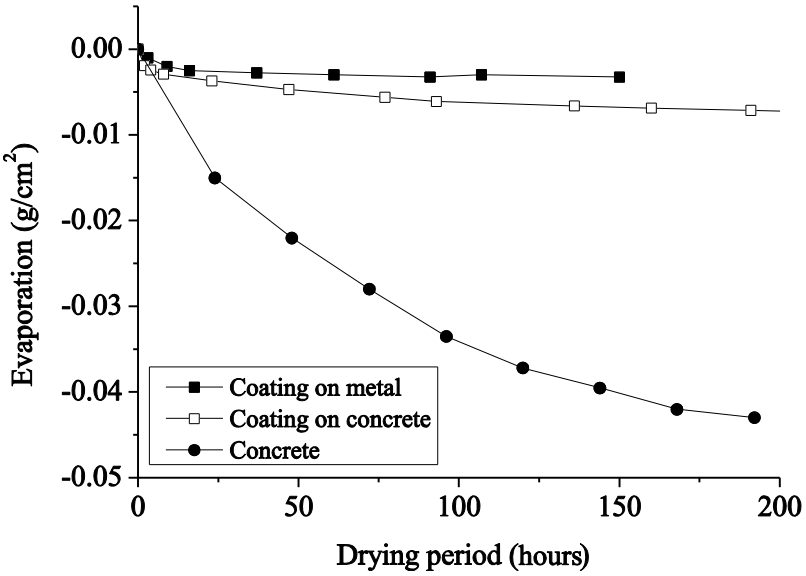

Fig. 5.2 Water vapor evaporation from the surface of concrete or coating on concrete. Result of coating on metal is also shown for comparison. This indicates that coating material itself is dried under drying condition.

Black acrylic ink was sprayed on the test surfaces to create a random pattern consisting of dots with a diameter ranging from 10 μm to 100 μm for the digital image correlation analysis. Specimens were dried under conditions of 20 ℃ ±2 ℃ and 60% ±5% RH. Changes in the length of the specimens were measured with the micrometer MHN3-25MB (Mitsutoyo Co.) with a resolution of 0.001 mm and a precision of ±0.003 mm, and the corrected length of specimens was obtained by calculating the difference in length with respect to a reference stainless steel bar. Specimens were subjected to the first length measurement before drying followed by subsequent measurements every few days. Measured values of diameters in three directions were averaged and recorded as the drying shrinkage strain. All measurements were executed in a room at a temperature of 20 ℃ ±2 ℃.

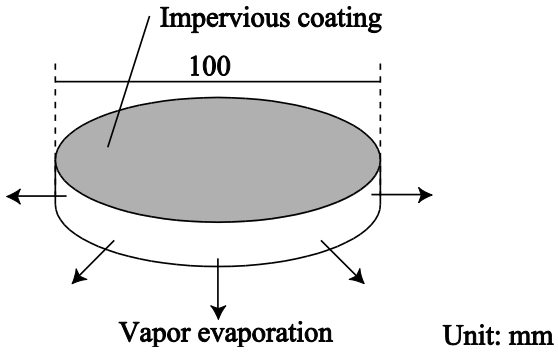

Fig. 5.3 Schematic of disk specimens

Changes in mass were measured with a precision balance with an accuracy of 0.04 g at the same time as the length measurement, and the rate of change was determined with respect to the initial mass. Each condition had three samples and averaged values are used for the discussion except for the DICM image results shown in Fig. 5.9 and 5.10. In Fig. 5.9 and 5.10, the sample most representative of typical results

from the three samples is shown.

5.2.4 Details of DICM

Digital image correlation (DIC) measurements were performed with a CCD camera Atik 383L+ (Artemis CCD Ltd., 3326 × 2504 pixel) and an Ai AF Nikor 35mm f/2D lens (Nikon Co.) as shown in Fig. 5.4. A reference image was captured before drying. In this setup, each pixel had a length of 0.043 mm [44, 50].

A commercial program (Vic-2D, Correlated Solutions, Inc.) was used for the DIC analysis. An algorithm for maximizing a normalized cross-correlation criterion (NCC) between the deformed subset and the reference subset was implemented in Vic-2D. A subset of 25 pixels × 25 pixels, a step of 5 (5-pixel-spacing between centers of subset), and a decay filter (90% center-weighted Gaussian filter) with a size of 15 were applied for conducting DIC to determine local displacement and strain distributions. A cross-section containing entrained and entrapped air bubbles on the specimen surface was omitted in the image analysis due to the occurrence of defocusing and shadow dropping in air bubbles causing inaccuracy in DIC results. This can sometimes cause the abortion of the DIC calculation itself. Even small cracks on the concrete surface can produce a large expansive strain in the DIC algorithm. Parameters were set based on data from our preliminary study [44]. We have also demonstrated that a positive maximum principle strain distribution is well reflected by a micro-crack distribution as confirmed by a fluorescent epoxy impregnation method [44].

Fine cracks have been detected and observed with a scanning electron microscope (SEM) and fluorescent epoxy impregnation techniques; however, these methods are not suited for observing changes in crack development. In this study, the use of DICM should allow the measurement of the development of strain distribution through discrete data and permit an informed discussion of the behavior of fine cracks.

Fig. 5.4 System for capturing digital images of unrestricted shrinkage specimens [52]

5.2.5 Restricted shrinkage experiment

Specimens with dimensions of 100 mm ×100 mm ×400 mm were subjected to underwater curing with a saturated calcium hydroxide solution for a year and then cut out to have dimensions of 185 mm ×100 mm ×9 mm. Specimens were then fixed in a steel frame with two sections of acrylic adhesive as shown in Fig. 5.5 and subjected to a restricted shrinkage measurement. Similar to the unrestrained specimens, two cutout surfaces were coated with a vapor impermeable film, which permitted water to escape only through the sides of the specimens. Specimens were then subjected to drying at a temperature of 20 ℃ ±2 ℃ and a RH of 60% ±5%.

The target surfaces of DIC measurements were prepared by spraying black acrylic ink on the white, impermeable epoxy coating to produce a random pattern. DIC measurements were recorded with the camera system by following the protocol in the previous section 5.2.3 and 5.2.4. In the measurement setup shown in Fig. 5.6, each pixel had a length of 0.079 mm. For each concrete mixture, one specimen was examined. Obtained data were evaluated by comparing against values in the literature and by numerical analysis.

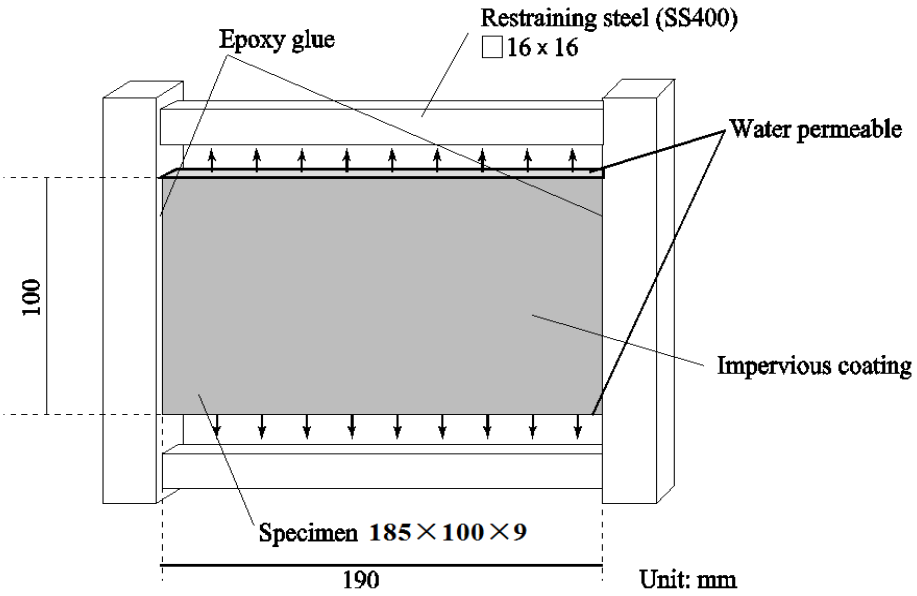

Fig. 5.5 Schematic of restricted specimens

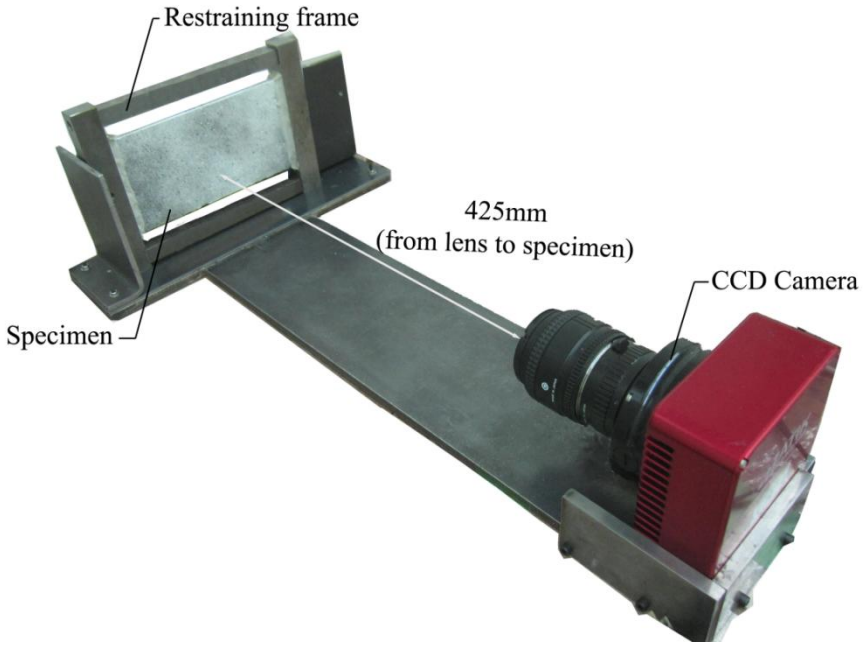

Fig. 5.6 System for taking digital images of restrained shrinkage specimens.

5.3 Experimental results and discussion

5.3.1 Unrestrained shrinkage experiments

Results of the length change measurement experiments on the disc specimens are shown in Fig. 5.7. The concrete total strain of SS was approximately 120 μ larger than that of LS after 91-day drying. This shrinkage strain difference was more than the theoretically calculated strain difference of 80 μ, which was estimated by multiplication of 200 μ, the difference in the aggregate shrinkage strain (taken from Fig. 5.1), by 0.4, the volume fraction of the coarse aggregate. This result suggests that the difference in shrinkage behavior of concrete can be mainly attributed to the drying shrinkage strain of the aggregate and that the average aggregate shrinkage difference might be more than 200 μ while there remains a possibility that the properties of the interfacial transition zone (ITZ) influence the drying shrinkage of concrete [52, 53].

Changes in mass shown in Fig. 5.8 were larger for SS than for LS. This can be attributed to excess water released from the sandstone aggregate, as its water absorption is twice as large as that of the limestone. The results of DIC measurement for LS and SS are shown in Figs. 5.9 and 5.10, respectively. Based on the literature showing that expansive strains in the maximum principal strain distribution correspond to fine cracks, subsets showing strains larger than 500 were taken as the areas containing fine cracks [44]. Minimum principal strains obtained with DIC are shown in Fig. 5.9, where the LS aggregate did not show shrinkage prior to drying. With drying age, changes in color from yellow to purple were observed at mortar parts, suggesting that the shrinking zone developed from the perimeter towards the inside of the specimen. This tendency was also confirmed for SS as shown in Fig. 5.10. Similar to those observed in the minimum principle strain distribution, some areas showed maximum principal strain

distributions changing from yellow to red (i.e., expansive strains developed from the perimeter towards the inside of the specimen, particularly around aggregates). These phenomena likely reflect crack initiation and propagation due to drying and resultant shrinkage strain distribution.

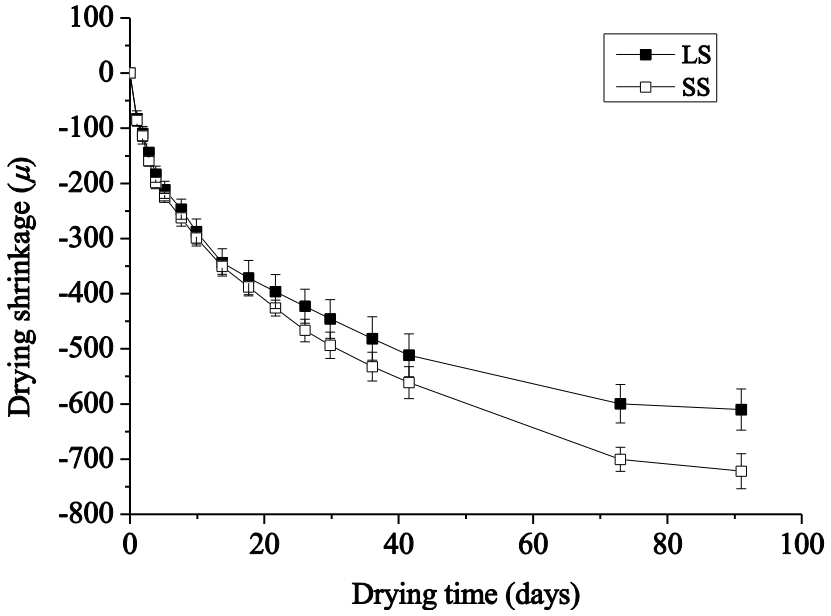

Fig. 5.7 Shrinkage of concretes. Error bars show 1-sigma.

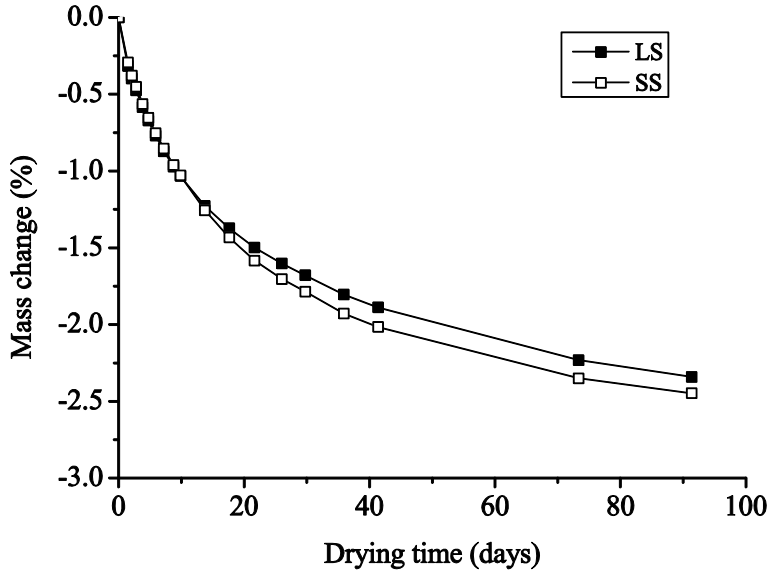

Fig. 5.8 Mass change of concretes. All the error bars for 1 sigma are within square plot.

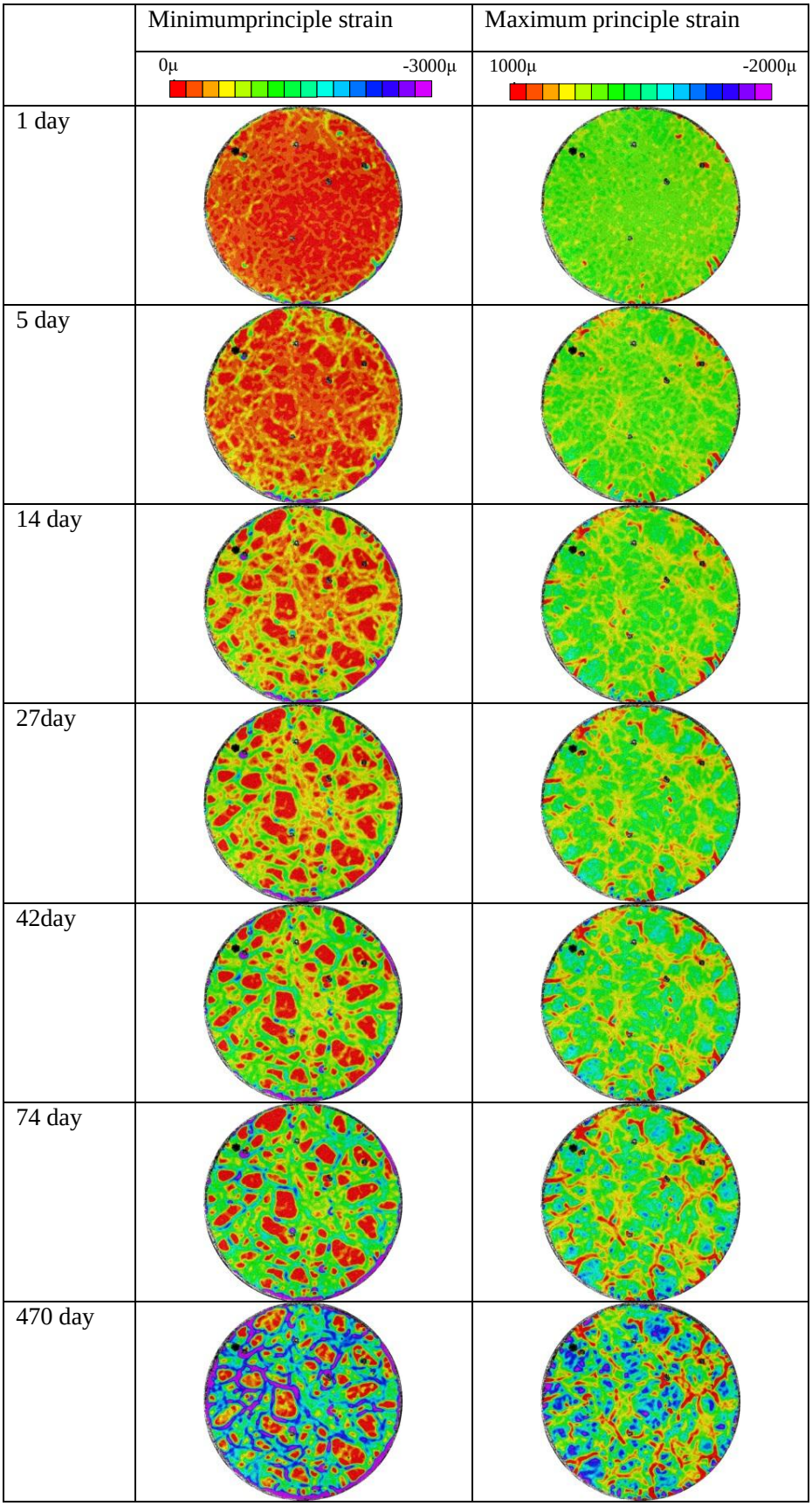

Fig. 5.9 Development of minimum and maximum strain distribution of LS sample section under drying using DICM.

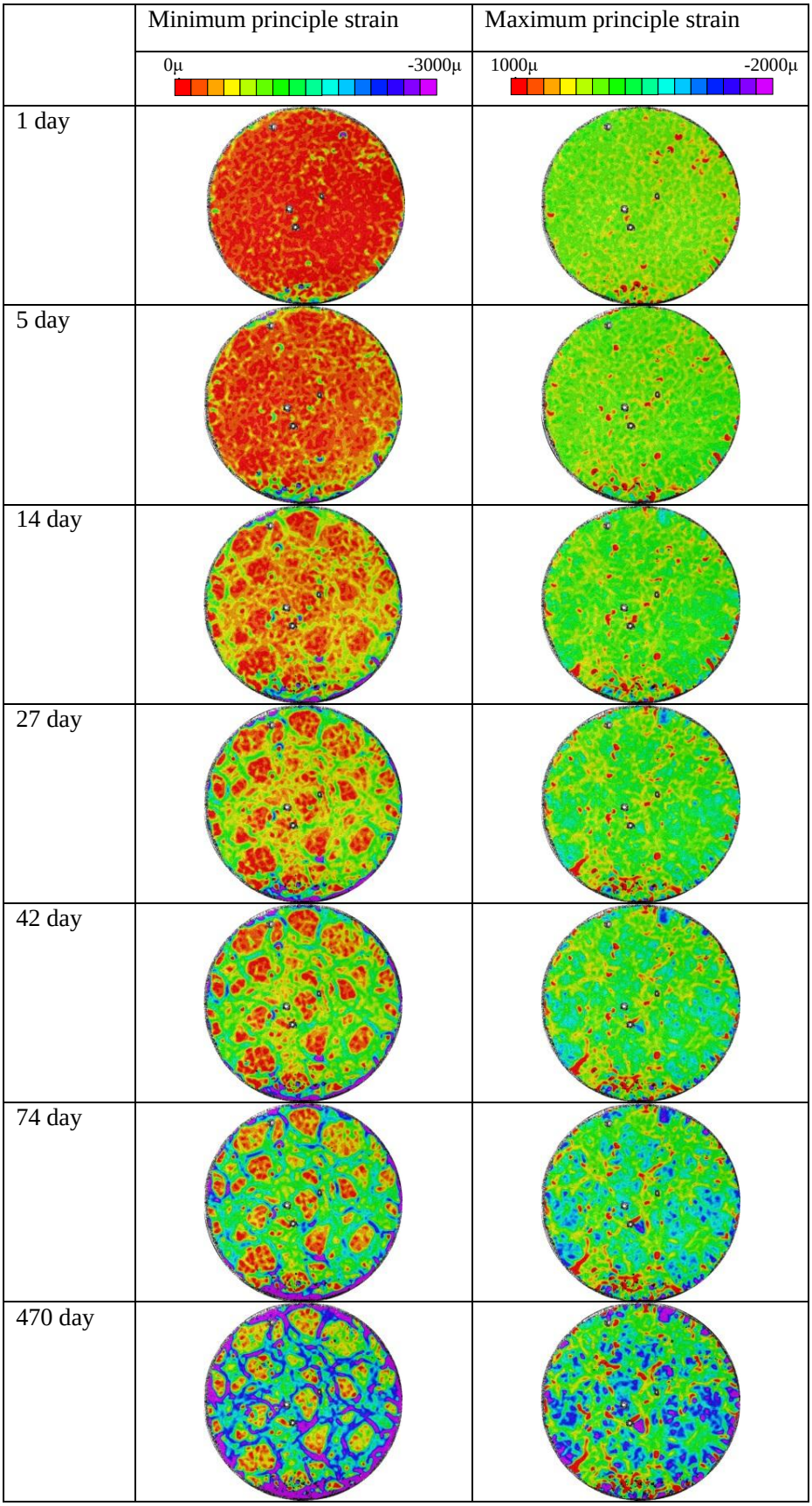

Fig. 5.10 Development of minimum and maximum strain distribution of SS sample section under drying using DICM.

Development of numerous fine cracks (i.e., expansive strains) could be confirmed at the center of the LS specimens even at an age of 14 days, while expansive strains in SS were not significant even at an age of 42 days. The different cracking tendency is a fertile area for further exploration. To discuss this difference in cracking progression, the minimum strain distributions over the test surface as a function of material age are summarized and shown in Fig. 5.11. The minimum principal strains at 2.5 mm, 11.5 mm, 24.5 mm, 37.5 mm, and 47.5 mm from the original point, averaging over the ±6.5mm of each point on 10 radial lines with arbitrarily selected angles, were averaged. The detailed calculation procedure is represented in Fig. 5.11(c). A gradient of shrinkage strain can be found in a region 35mm from the drying surface of the LS specimen even at the age of one day. The behavior of the region remained unchanged after 14 days. Taking into account the minimum principal strain distribution shown in Fig. 5.11(a) and (b), it can be hypothesized that the excessive shrinkage takes place due to accelerated drying caused by fine crack propagation from the surface and around the coarse aggregates, and the aforementioned development of fine cracks originates due to an uneven shrinkage behavior between limestone and mortar. The synergistic impact of crack development and acceleration of drying inside of specimen is represented in Fig. 5.11.

On the other hand, the gradient of shrinkage strain remained within 20mm from the drying surface in the SS specimens. Taking into account the maximum principal strain distributions shown in Fig. 5.10, the shrinkage strain gradient can be attributed to an inhibition of drying due to the large shrinkage of aggregate resulting in less uneven changes in the volumes of aggregate and mortar. In addition to the intrinsic shrinkage properties of GS and mortar, the water supply from the aggregate to mortar might help maintain the moisture content of the mortar, resulting in the inhibition of uneven shrinkage between the aggregate and mortar. This mechanism seems likely since the mass change of SS was larger than that of LS as shown in Fig. 5.8. It has also been proven that water-saturated, porous aggregates can compensate for the drying of surrounding mortar [54, 55].

The present study has not experimentally confirmed that the aggregate-mortar ITZ influences the fine crack generation around the aggregate. However, the literature suggests that the hydrophilicity of the aggregate surface may affect crack propagation [56]. Differences in hydrophilicity cause different characteristics of the ITZ, such as the thickness of voids on the surface of aggregates, bond strength, and stiffness of the nominal mortar-aggregate interface, to arise through the influence of the cement particle packing process on the surface aggregate in fresh concrete. However, the result of a numerical analysis of unrestrained shrinkage under ideal conditions showed that the bond strength between aggregate and mortar exerts no significant effect [43]. On the other hand, it has been observed that the surface of the limestone surface is denser than that of sandstone [57], and a larger bond strength with the limestone aggregate surface would be expected [56]. Therefore, the shear stress on the limestone surface is stronger than that on the sandstone surface. In addition to this, cross cracks between aggregates are more probable in the case of limestone aggregates due to stronger bond strengths, hence facilitating easy crack propagation.

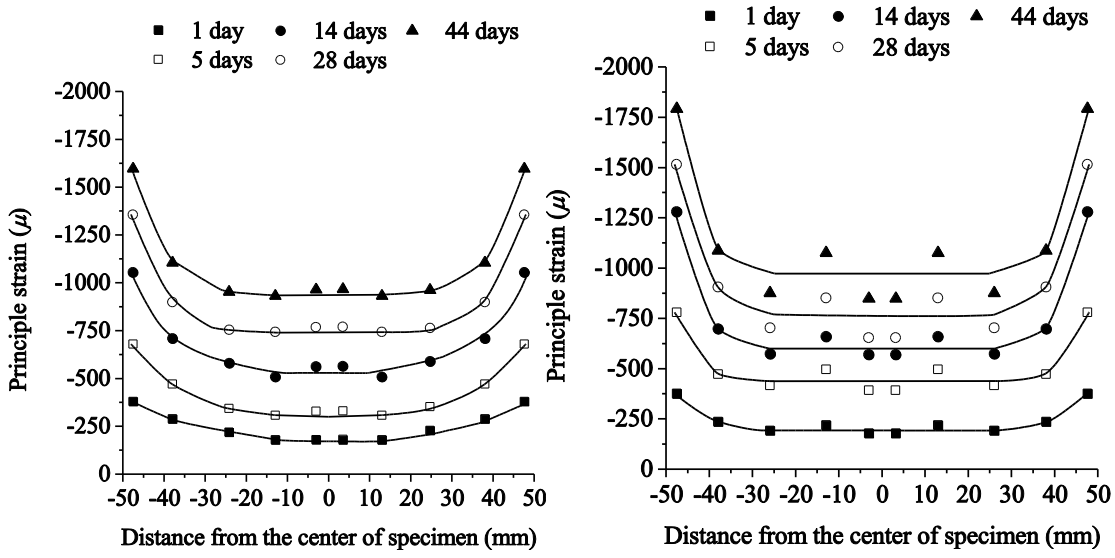

(a) LS (b) SS

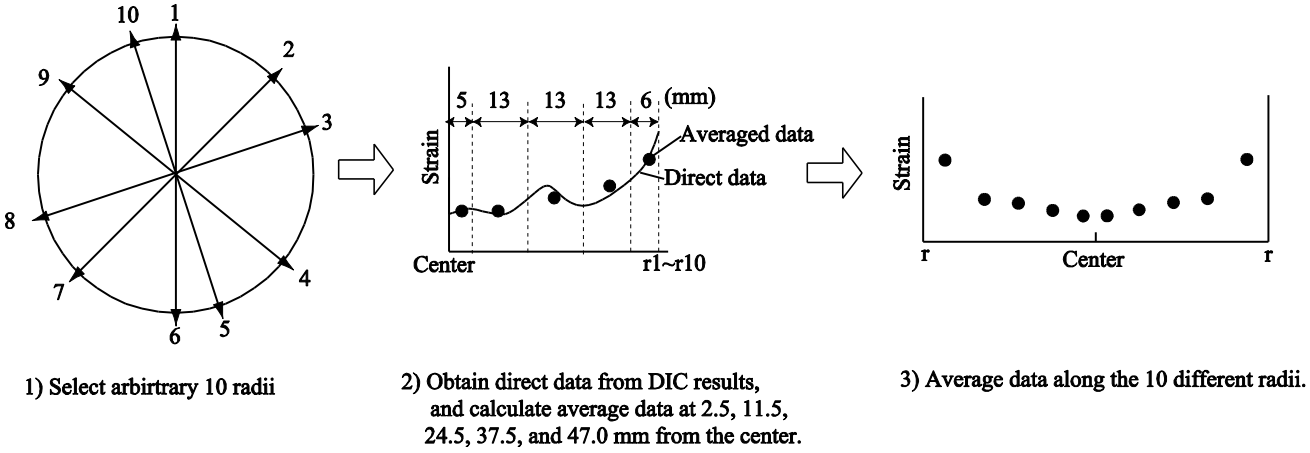

(c) Calculation procedure

Fig. 5.11 Distribution of minimum principle shrinkage strain as a function of distance from the center of the specimen and drying periods. (a) LS, (b) SS, (c) Steps of data calculation.

5.3.2 Restricted shrinkage experiment

The minimum and maximum principal strain distributions in the LS and SS specimens are shown in Fig. 5.12 and 5.13, respectively. Regions with the maximum principal strain larger than 500 μ were assumed to be origins for possible generation of fine cracks and are shown in orange or yellow in the maximum strain distribution images. Sample recordings during the progression of drying through permeable surfaces are shown from the top to the bottom of the figures. The migration of shrinkage from the periphery towards the inside can be confirmed from the minimum principal strain distributions. The maximum strain distribution images of LS confirm that numerous fine cracks were generated at the beginning of the drying process and that they gradually progressed towards the inside of the specimen. The

fine cracks did not show any interlinking with each other, at least at the observed surfaces, and were evenly distributed when the limestone aggregate was used. This can be attributed to the large difference in shrinkage and (likely) large bond strength between the mortar and limestone aggregate.

On the other hand, a few fine cracks were present at the surface of the SS specimens that proceeded to combine into a single large through-crack during drying. Differences in shrinkage between the sandstone aggregate and mortar could potentially be controlled by two factors: the intrinsic shrinking properties of the aggregate and the inhibition of the shrinkage of mortar with water released from the aggregate. Less uneven shrinkage behavior between the aggregate and mortar decreases the possibility of crack generation around aggregates. A smaller bond strength between the aggregate surface and mortar also decreases the possibility of cross cracking between aggregates. Assuming these effects, cracks generated at the surface of concrete would accelerate the drying process along the surface of cracks, and consequently promote shrinkage near the cracks. Therefore, cracks are not distributed, and instead a single crack grows towards the inside of the specimen. As a result, shrinkage cracks are integrated and localized, allowing water release for further shrinkage and localization of the crack, while progression of the crack opening may release stress around it and contribute towards closing other cracks and suppress the acceleration of drying around them. This observed behavior of cracking in concrete under restraint conditions is consistent with the results from the previous experimental studies [41, 42]. Therefore, even though the number of specimens is limited in the current study, these present experimental results accurately reflect the typical cracking behavior in concrete as affected by aggregate properties.

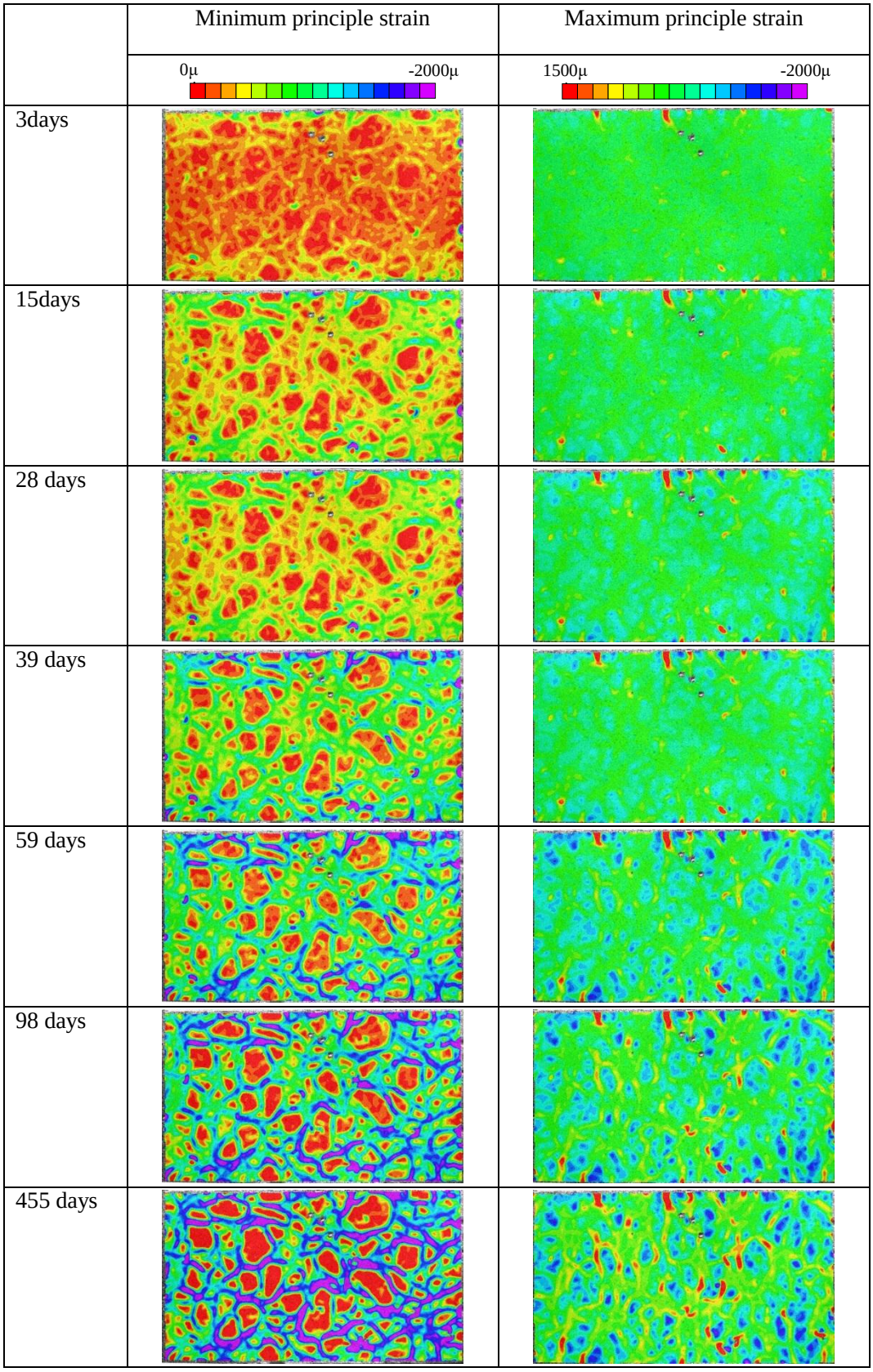

Fig. 5.12 Development of minimum and maximum principle strain distributions of restricted LS specimen during drying.

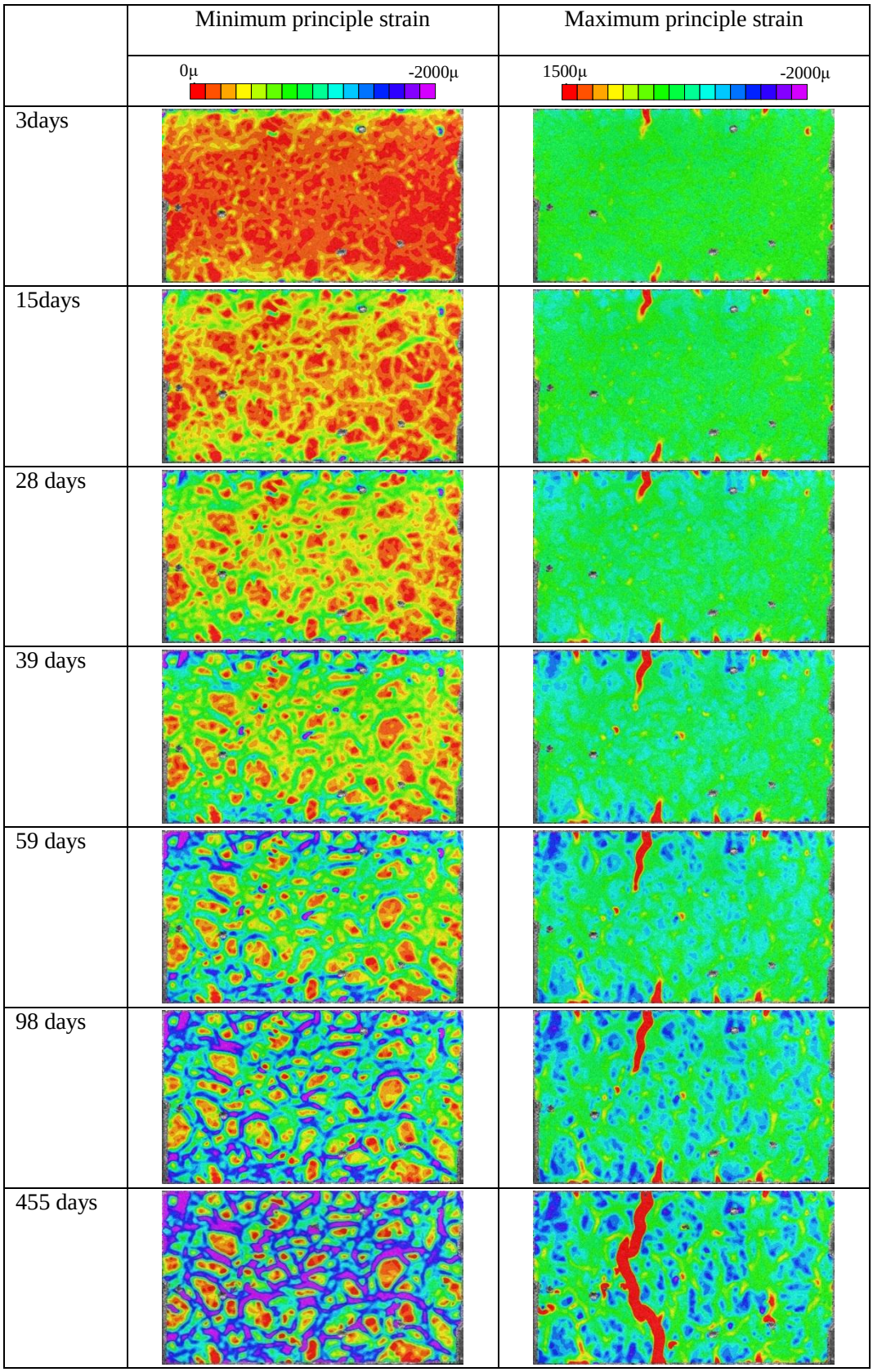

Fig. 5.13 Development of minimum and maximum principle strain distributions of restricted SS specimen during drying.

5.4 Numerical study

5.4.1 RBSN

The Rigid-Body-Spring Networks (RBSN) model developed by Kawai[47] has been applied extensively for structural analysis. RBSN deals with crack propagation of concrete directly[48]since it represents a continuum material as an assembly of rigid particle elements interconnected by zero-size springs along their boundaries [47].Being nonlinear, these zero-size springs can simulate the cracking behavior of a continuum material. In the present modeling, each interface between two rigid particles was divided into several triangles sharing the barycenter of the interfacial plane, with each triangle having three individual springs, one for a normal force and two for orthogonal tangential forces. In existing studies (for e.g.,[49]), the interfacial plane has a rotation spring for bearing momentum, while in the present study, several divided triangles with springs for normal forces bearing the momentum acting on the interfacial plane as shown in Fig. 5.14 were used instead. At the same time, the nonlinearity of normal and tangential springs can take into account the nonlinearity of the rotation behavior on the interfacial plane.

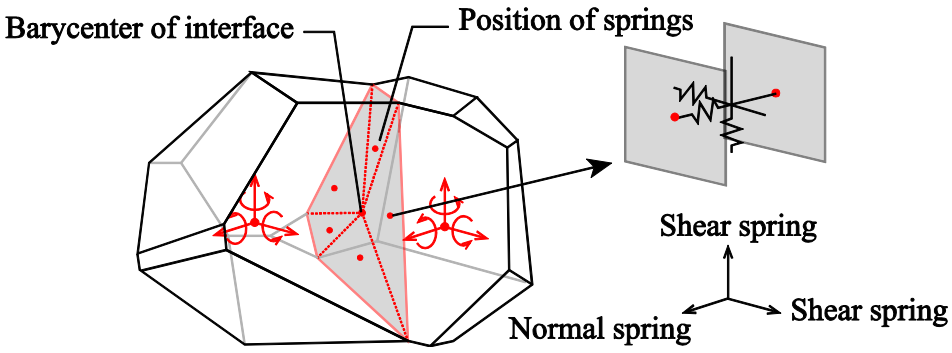

Fig. 5.14 Schematic of the elements in RBSM and springs connecting them.

The nonlinearity and discrete behavior of the continuum material is emulated by cracks developing at the interfaces of the rigid particles. For this reason, crack patterns and the resultant nonlinear behavior of the target model are significantly affected when a mesh design is employed. To solve this problem, random geometry using Voronoi diagrams was applied [48].

Concrete sections under restraint conditions, similar to the results shown in Section 5.3.2, were subjected to the numerical calculation. To evaluate the impact of aggregate properties in isolation, three different phases, namely the mortar matrix, aggregates, and mortar-aggregate interfaces, were modeled.

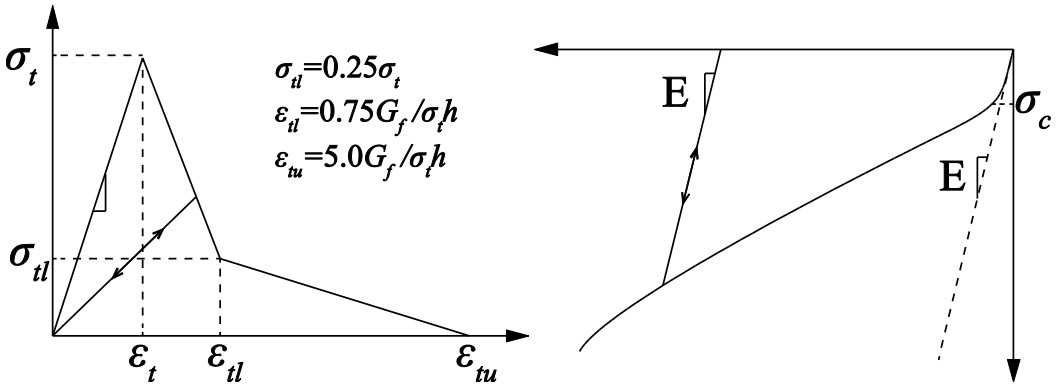

Fig. 5.15 Schematic of the constitutive law of the normal spring in the mortar.

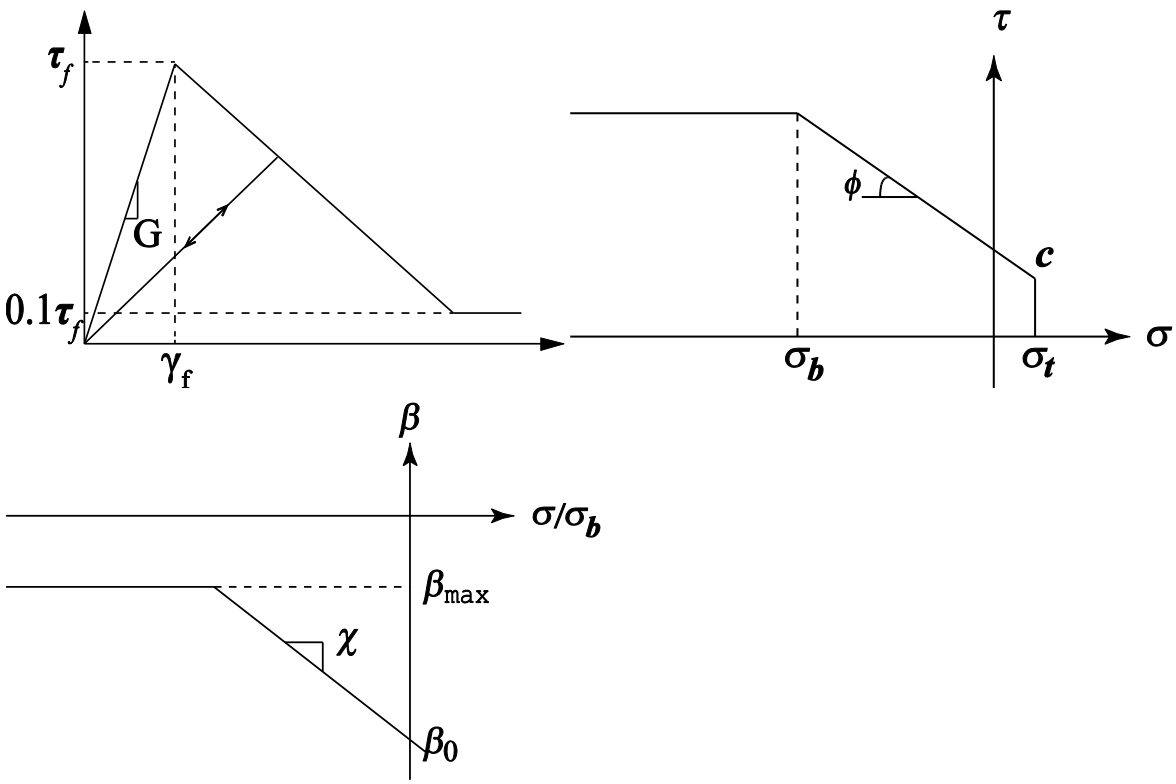

Fig. 5.16 Schematic illustration of shear springs in the mortar.

For the mortar matrix, the tensile behavior of mortar was modeled using linear elasticity to tensile strength, followed by a bilinear softening branch of a 1/4 model [58], as shown in Fig. 5.15(a). The parameters for mortar behavior in the tension field are the tensile strength f_t, the tensile fracture energy G_{ft}, and the distance between the Voronoi generators (centroid of rigid particle) h. The mortar behavior in the compression field is shown in Fig. 5.15(b), whose S-type curve is derived from the relationship between stress and volume under hydrostatic pressure conditions[59]. Tangential springs represent the shear transfer mechanisms of cracked and uncracked mortar matrices (Fig. 5.16(a)). The softening process was modeled by the following equations [59]:

$$\tau = \begin{cases} G\gamma & (\gamma < \gamma_f) \\ \max(\tau_f + K(\gamma - \gamma_f), 0.1\tau_f) & (\gamma_f < \gamma) \end{cases} \quad (5.3)$$

where G: shear stiffness (N/mm2), τ_f : shear strength (N/mm2), γ_f: strain at the maximum stress in shear strain and shear-stress relationship, and K: shear softening coefficient. A linear relationship between shear strain and shear stress was first assumed until the stress reached the peak. Following the peak, the softening process was determined by the strain and stress normal to the plane on which the shear force was acting, while the minimum value was assumed to be 0.1 τ_f.

The shear strength was defined by the Mohr-Coulomb type criterion (Fig. 5.16(b)) and is represented by the following equations[59]:

$$\tau_f = \begin{cases} c - \sigma \tan\phi & (\sigma > -\sigma_b) \\ c + \sigma_b \tan\phi & (\sigma < -\sigma_b) \end{cases} \quad (5.4)$$

Where c: cohesion parameter (N/mm2), φ: angle of internal friction (degree), and σ_b: maximum shear strength of a normal spring (N/mm2).

The softening process of shear springs is a function of normal stress as shown in Fig. 5.16 (c):

$$K = \beta G \quad (5.5)$$

$$\beta = \min(\beta_0 + \chi(\sigma / \sigma_b), \beta_{\max}) \quad (5.6)$$

where β_0, β_{max}, and χ: parameters for shear softening [59].

Shear transfer is reduced when the strain in the normal direction to the plane that shear stress acts upon is in the post-peak region. This process is represented by a coefficient β_{cr} [60] as shown in Eqs. (5.7) - (5.9):

$$\tau = \begin{cases} \beta_{cr} G\gamma & (\gamma < \gamma_{ft}) \\ \beta_{cr} \max(\tau_f + K(\gamma - \gamma_{ft}), 0.1\tau_f) & (\gamma_{ft} < \gamma) \end{cases} \quad (5.7)$$

$$\beta_{cr} = \frac{\varepsilon_t}{\varepsilon} \exp\left\{ \frac{\kappa}{\varepsilon_{tu}} (\varepsilon - \varepsilon_t) \right\} \quad (5.8)$$

$$\tau_{ft} = c - f_t \tan\phi \quad (5.9)$$

where $\gamma_{ft}=\tau_{ft}/G$, ε_t: strain at the peak of normal stress, ε_{tu}: ultimate normal strain when stress attains zero, ε: normal strain, and κ: reduction factor for shear transfer due to cracking.

Linear elasticity was assumed for the aggregate. In general, the strength of the aggregate is larger than that of mortar, and therefore the strength of the aggregate was not taken into account. In the present study, the amount of drying shrinkage of the aggregate was considered as a parameter. We assumed two different magnitudes of shrinkage, specifically 0μ and −400 μ corresponding to the limestone and sandstone coarse aggregates, respectively. These shrinkage values were designed based on former research of sand stone

shrinkage that found that 400μ was almost the maximum shrinkage at 60% RH in the available sandstones [61].

The Young's modulus of aggregates may also affect the cracking behavior through a restraining role for mortar shrinkage. The average Young's modulus of sandstone available in Japan was found to be approximately 65GPa by ultra-sonic pulse velocity measurement [62] and double of this value was used for comparison.

The interface between the aggregate and mortar (i.e., the ITZ [63]) was modeled explicitly, although quantitative data relating to the ITZ has been scarcely reported. The ITZ is generally considered to be produced by the "wall effect" of the cement particle packing process on the surface of the aggregate [64]. Our ITZ is more porous than normal mortar and different physical properties were expected as a result.

In a previous RBSN study dealing with concrete as a two-phase material, the compressive failure of cylindrical concrete specimens was accurately reproduced by taking the average of the physical properties of mortar and the aggregate as the value for the ITZ [60]. However, the tension field properties have not been studied comprehensively, although the tension in the porous ITZ zone must have a large impact on the cracking behavior of concrete.

Calculation parameters for tensile strength, Young's modulus, and fracture energy were adopted based on a literature survey of porosity distribution findings [64-67], nano-indentation results, an SEM analysis [64, 68], and physical properties testing [56, 63, 69-71]. As the porosity in the ITZ is more than three times larger than that of normal mortar located far from the surface of the aggregate[64, 68], the Young's modulus and the tensile strength of the ITZ must be half of the normal mortar under the assumption of a linear or exponential relationship between porosity and physical properties. Therefore, in the present simulation, 0.50 times the Young's modulus and 0.75 times the tensile strength of normal mortar were considered for the calculations. With regard to fracture properties, Alexander et al. [72] have reported that the fracture energy of the ITZ is possibly less than 10% of that of bulk cement paste or mortar of dolomite aggregates with ordinary Portland cement and silica fume. Therefore, 0.1, 0.2, and 0.4 times the fracture energy of normal mortar were considered as the ITZ parameters.

Adopting these parameters, the different stress-strain relations in the compression and tension fields were applied to the modeling of the ITZ. The schematic is presented in Fig. 5.17.

Former research has found that when a limestone aggregate is used, the texture of cement hydrates in the ITZ is densified [57] and the fracture energy and bond strength of the ITZ are strengthened [56, 57]. Note that aggregate particle size and surface roughness remain important factors for ITZ properties [63, 71, 73, 74]. Therefore, these trends of ITZ properties in the case of concrete containing limestone aggregates should be considered during the interpretation of a numerical analysis.

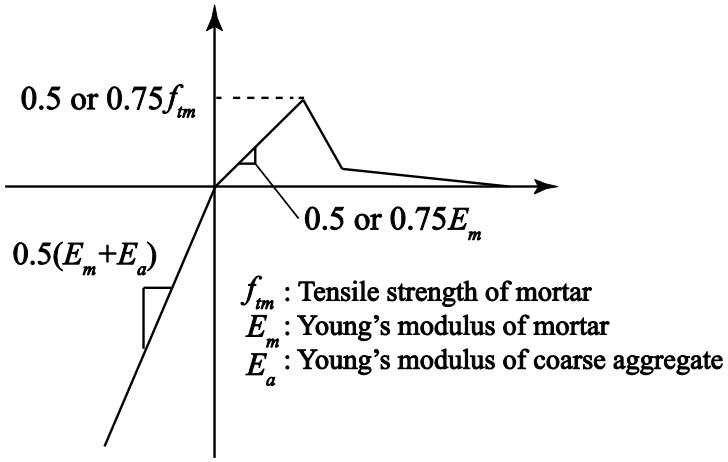

Fig. 5.17 Schematic of different properties of the ITZ in compression or tension fields.

5.4.2 Truss networks model for mass transfer

Water diffusion in the mortar and aggregate was modeled using a random lattice, whose mesh was defined by a Voronoi diagram, originally developed by Bolander and Berton [75]. Lineal conduit elements connect the Voronoi generators and special nodes set on boundary surfaces, which are named "Surface truss nodes", are the centroid of surfaces of Voronoi mesh facing the boundary. The schematic of the lattice model is shown in Fig. 5.18 and both the Voronoi generators and surface truss nodes are shown.

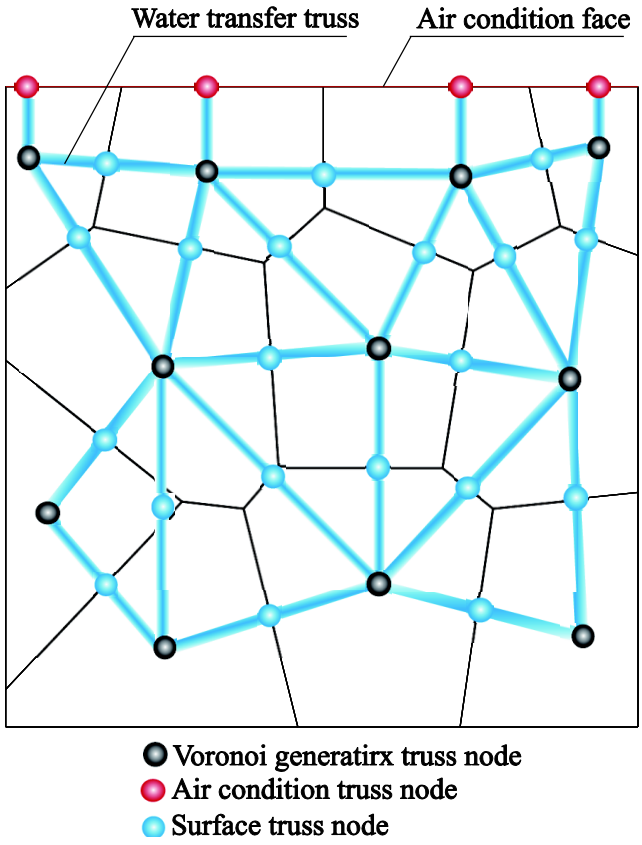

Fig. 5.18 Schematic of the truss network model for moisture transfer analysis.

The governing equation of potential flow of Eq. (5.10) was modeled assuming potential flow in the linear conduit as described in Eq. (5.11):

$$\frac{\partial w}{\partial \mu}\cdot\frac{\partial \mu}{\partial t}=\mathrm{div}\left(K(w)\mathrm{grad}\,\mu\right)+\frac{\partial w_{hyd}}{\partial t} \tag{5.10}$$

$$\frac{A_e K(w)}{L}\begin{bmatrix}1 & -1\\ -1 & 1\end{bmatrix}\begin{Bmatrix}\mu_1\\ \mu_2\end{Bmatrix}+\frac{\partial w}{\partial \mu}\frac{1}{\omega}\frac{A_e L}{6}\begin{bmatrix}2 & 1\\ 1 & 2\end{bmatrix}\begin{Bmatrix}\partial\mu_1/\partial t\\ \partial\mu_2/\partial t\end{Bmatrix}+\frac{A_b K(w)}{d_{env}}\begin{Bmatrix}\mu_1-\mu_{env}\\ \mu_2-\mu_{env}\end{Bmatrix}=\begin{Bmatrix}0\\ 0\end{Bmatrix} \tag{5.11}$$

where w: volumetric water content (g/mm^3);

w_{hyd}: water consumption by cement hydration (g/mm^3);

K (w): water transfer coefficient (mm^2/s·g/mm^3·g/J);

μ_1, μ_2: chemical potential of water in conduit nodes 1 and 2, respectively (J/g);

μ_{env}: chemical potential of water in the environment (J/g);

d_{env}: nominal distance for the boundary condition of water transfer from the matrix to the environment(mm);

t: time (s);

ω: volumetric conversion factor, (2.0 in case of 2-dimensional flow);

A_e: the area of the Voronoi facet between the contiguous nodes i and j;

L: length of conduit from node 1 to 2.

The third term in left hand formula represents the flow on the boundary surface. It is assumed that a hypothetical element with conduit length of d_{env} was set on the boundary surface and this will be shown in Eq. (5.15). In the present method, the total volume of the conduits was set as the total volume of the target Voronoi elements [49]. For the time development, the entire matrix was assembled based on Eq. (5.11) and the Crank–Nicolson scheme was applied with equidistant time steps.

The water transfer model was based on the research of Maruyama et al. [76]. The global chemical potential of water was considered for the flow potential, and the water transfer coefficient of hardened cement paste K (w) was derived from experimental data. The results were reproduced by the following equations:

$$K(w)=\frac{1}{\left(5.0-9.1R+4.15R^2\right)}K_{60} \tag{5.12}$$

$$K_{60}=1.47\cdot10^{-13}\exp\left(4.41t_w\right) \tag{5.13}$$

$$t_w=w_g/\rho_w/S \tag{5.14}$$

where K_{60}: reference water transfer coefficient where the relative water content was 0.6 (mm^2/s·g/mm^3·g/J);

R: relative water content (-);

t_w: statistical thickness of adsorption (nm);

w_g: mass water content where the reference state is oven-dry conditions at 105 ℃ (g/mm^3);

ρ_w: density of liquid water in the mortar or aggregate (0.001 g/mm^3);

S: water vapor BET surface area (mm^2/mm^3).

In the present study, the water transfer coefficient of hardened cement paste was assumed to be the same as that of mortar.

The following equation was used for this boundary condition:

$$J_{w,bnd} = A_b K(w) \frac{\mu - \mu_{env}}{d_{bnd}} \qquad (5.15)$$

where $J_{w,bnd}$: flux at the boundary (g/s);

A_b: area of the finite area on the boundary (mm^2);

μ_{env}: global chemical potential of water vapor of the environment;

d_{bnd}: imaginary distance from the boundary to the environment (3 mm).

For the properties of the aggregate and the ITZ, the water capacity dw/du was based on preliminary experimental data [62], and the water transfer coefficient of the aggregate was assumed to be 10 times that of mortar since the aggregate reaches equilibrium faster than hardened cement paste according to previously measured sorption isotherms[50]. Cracked ITZ, which is expected to have a larger water transfer coefficient, was not considered in the present calculation. This assumption may produce conservative results of cracking behavior in concrete in terms of how it is affected by aggregate properties. In the calculation, the moisture related properties of mortar are estimated from the water to cement ratio of the mixture proportion. Uniformity of the mortar matrix is assumed because a viscosity improver is used in the reference concrete. There is an additional possibility that the water in the aggregate can move during the young age of the sample due to osmotic pressure caused by the ion concentration of pore solution [55] but this phenomenon is considered negligible.

5.4.3 Analysis outline

In the present study, cracks that might be affected by a presence of aggregate are discussed by RBSM analysis results. Due to the limitations of meshing geometry and the calculation process of RBSM, the target cracks are yielded according to the representative mesh size, which is about 5 mm in the present study as shown in Fig. 5.19. In other words, the cracks within 5 mm intervals can not be shown directly in the present calculation, and the physical role of these cracks are numerically represented by a reduction of spring stiffness, which is a function of its strain. For this reason, complete reproduction of concrete behavior, which shows true multi-scale cracking and resultant change in macroscopic physical properties, and quantitative evaluation of the reproducibility of the present calculation are impossible because applicable quantitative indices can not be obtained. However, qualitative evaluation gives insight into understanding the role of aggregate in concrete with regard to the crack propagation process. Therefore, this study attempts to obtain the key parameters of the aggregate in cracking behavior through parametric studies. Although these parametric studies are discussed by relative comparisons, the parameters used in the calculations are set to be as realistic as possible.

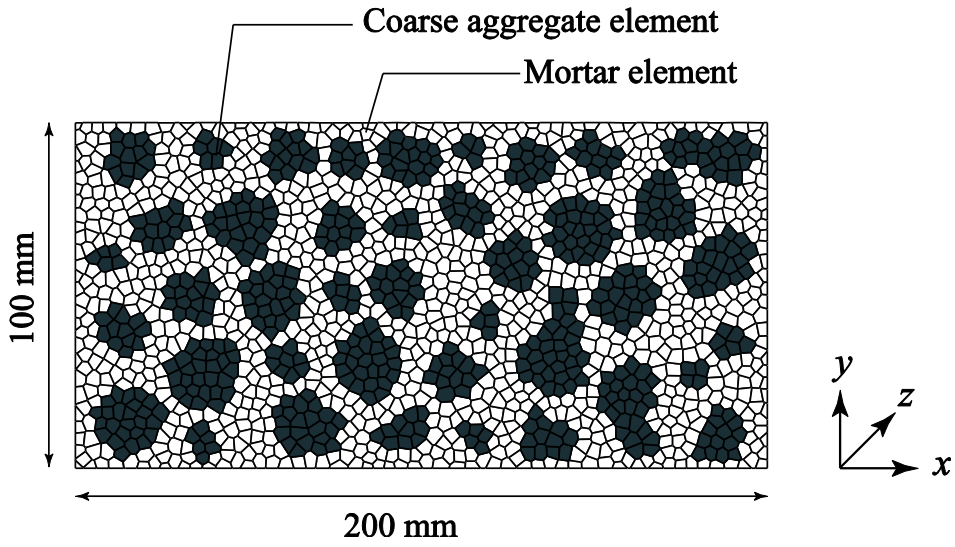

(a) Geometry of the meshing

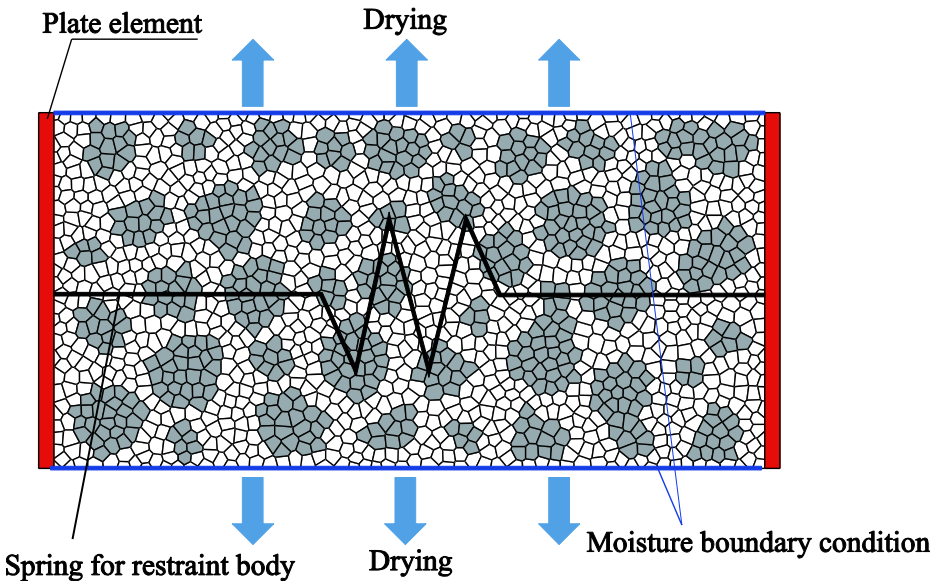

(b) Boundary conditions of the model.

Fig. 5.19 Meshing and boundary conditions.

Specimens with dimensions of 200 mm × 100 mm × 9 mm under restraint conditions discussed in Section 5.3.2 were the target of the present numerical study. For the calculation, the quasi-two dimensional mesh shown in Fig. 5.19(a) was used. Voronoi meshing with a representative diameter of 5 mm was applied in the X-Y plane, while the same section was held in each element in the Z-direction to better understand the crack propagation process in the specimen.

The upper and bottom edges of the model were considered as the boundaries of moisture transport as shown in Fig. 5.19(b). The environmental conditions were considered to be 20°C and 60% RH. The boundary conditions for force equilibrium and the restraint body of stainless steel bars were modeled by a

large spring whose ends were connected to a rigid plate adjoining the edge of the concrete specimen. The stiffness of the spring was calculated from the Young's modulus (205 GPa) and sections ($32mm^2 \times 16\ mm^2$) of the members.

Calculations were performed until 91 days after drying. The shrinkage of the mortar or aggregate was modeled as a function of the relative water content ($R = w/w_0$) as shown in the following equation:

$$\Delta\varepsilon_{sh} = \alpha_{sh} \cdot \Delta R \qquad (5.16)$$

where α_{sh}: coefficient of conversion from relative water content to shrinkage strain and R: relative water content (i.e., the ratio of water content w to the maximum water content w_0). The shrinkage of the mortar or aggregate was considered as an isotopic equivalent nodal force in the calculations.

In the present study, the creep of hardened cement paste was not considered since the preliminary experiments showed that the tensile creep coefficient of hardened cement paste was only 0.1 [77]. Further, given the small tensile stress in the present study, the creep strain in the hardened cement paste or mortar should not have a large impact on the calculation results. In our analytical hypothesis, tensile creep of concrete can be explained by the fine cracks dues to stress and drying shrinkage and the resultant reduction of Young's modulus of concrete [50].

Material properties and parameters used in the calculations are summarized in Table 5.5 ~ 5.7. In addition, a summary of parameters for numerical analysis and a companion group showing the objectives and notations of the parameter sets are presented in Table 5.8, where Sh XX is shrinkage of XX microns; EaXX is Young's modulus of the aggregate of XX GPa, XXE is Young's modulus of the ITZ of XX times the Young's modulus of mortar, XXft is tensile strength of the ITZ of XX times the tensile strength of mortar, and XXGft is fracture energy of the ITZ of XX times the fracture energy of mortar.

Table 5.5 Physical properties of materials assumed in the numerical analysis.

	Young's modulus E^* (N/mm^2)	Poisson's ratio (-)	Tensile strength f_t^* (N/mm^2)	Fracture energy G_{ft}^* (N/m)	Compressive strength f_c^* (N/mm^2)
Mortar	17	0.2	3.0	70[a)]	40
Aggregate	65	0.18	200[b)]	—[b)]	200[b)]
ITZ	d)	0.2[d)]	1.5, 2.25[c)]	7, 14, 35[c)]	40[d)]

a) Calculated from JSCE equation; b) aggregate failure is not assumed in the present calculation;
c) See Fig. 5.17, and Table 5.6; d) The same value as that of mortar is assumed.

Table 5.6 Applied values of springs in the numerical calculation.

(a) Normal spring

	Young's modulus	Tension field		Compression field			
	E (N/mm^2)	f_t (N/mm^2)	G_{ft} (N/mm)	f_c (N/mm^2)	ε_{c2}	α_{c1}	α_{c2}
Mortar	$1.3E^*$	$0.8f_t^*$	$0.5G_{ft}^*$	$1.5f_c^*$	-0.015	0.15	0.25
Aggregate							
ITZ							

(b)Shear spring

	Shear modulus	Failure criteria			Softening behavior			
	η=G/E	c (N/mm^2)	φ (degree)	σ_b (N/mm^2)	β_0	β_{max}	χ	κ
Mortar	0.4	$0.17f_c^*$	37	$0.5f_c^*$	-0.1	-0.05	-0.02	-0.6
Aggregate	0.35							
ITZ	0.4							

E^*, f_t^*, G_{ft}^*, f_c^*: shown in Table 5.5.

Table 5.7 Parameters of materials for drying process

	Volumetric water content at saturation $w(10^{-3}g/mm^3)$	BET surface area S (m^2/g)	Moisture transfer coefficient at saturation ($mm^2/s \cdot g/mm^3 \cdot (J/g)^{-1}$)	Moisture capacity dw/du	Shrinkage at 60% RH	
					α_{sh}	
Mortar (=Paste)	0.2505	170	8.5×10^{-9}	0.0016	-1800 μ	
					4000×10^{-6}	
Aggregate	0.00765	10	8.5×10^{-8} a)	0.00005	-400 μ	0 μ
					906×10^{-6}	0
ITZ	0.129 b)	90 b)	8.5×10^{-8} a)	0.000825 b)	-1200 μ b)	-900 μ b)
					2450 $\times10^{-6}$ b)	2450 $\times10^{-6}$ b)

a): 10 times that of mortar, b):Average value of mortar and aggregate

Table 5.8 Notation and parameters for numerical analysis

Objective	Notation	Shrinkage of aggregate (μ)	Young's modulus of aggregate (GPa)	ITZ properties		
				Young's modulus E	Tensile strength f_t	Fracture energy G_{ft}
Simulation of concrete with sandstone and limestone	Sh0_E130_0.4Gft	0	130	$0.5E^*$	$0.5f_t^*$	$0.4G_{ft}^*$
	Sh400_E65_0.1Gft	400	65	$0.5E^*$	$0.5f_t^*$	$0.1G_{ft}^*$
Impact of Young's modulus and shrinkage of aggregate	Sh0_Ea65	0	65	$0.5E^*$	$0.5f_t^*$	$0.2G_{ft}^*$
	Sh0_Ea130		130			
	Sh400_Ea65	400	65			
	Sh400_Ea130		130			
Impact of Young's modulus and strength of ITZ	Sh0_0.5E_0.25f_t	0	65	$0.5E^*$	$0.25f_t^*$	$0.2G_{ft}^*$
	Sh0_0.5E_0.5f_t			$0.5E^*$	$0.5f_t^*$	
	Sh0_0.5E_0.75f_t			$0.5E^*$	$0.75f_t^*$	
	Sh0_0.5E_1.0f_t			$0.5E^*$	$1.0f_t^*$	
	Sh0_0.75E_0.25f_t			$0.75E^*$	$0.25E^*$	
	Sh0_0.75E_0.5f_t			$0.75E^*$	$0.5E^*$	
	Sh0_0.75E_0.75f_t			$0.75E^*$	$0.75f_t^*$	
	Sh0_0.75E_1.0f_t			$0.75E^*$	$1.0f_t^*$	
Impact of fracture energy of ITZ	Sh0_0.1Gft	0	65	$0.5E^*$	$0.5f_t^*$	$0.1G_{ft}^*$
	Sh0_0.2Gft					$0.2G_{ft}^*$
	Sh0_0.4Gft					$0.4G_{ft}^*$

E^*, f_t^*, G_{ft}^* : values for mortar shown in Table 5.5.

5.4.4 Numerical analysis results and discussion

5.4.4.1 Moisture transfer

Fig. 5.20 shows the results of the drying process. As the analysis takes into account differences in the water capacity and the water transfer coefficient between the aggregate and mortar, oscillation in drying depth was observed. After 91 days, almost exclusively within 1 or 2 mm from the surface, the mortar attained equilibrium with the surrounding environment. On the other hand, the center of the specimen still indicated more than 74% of RH.

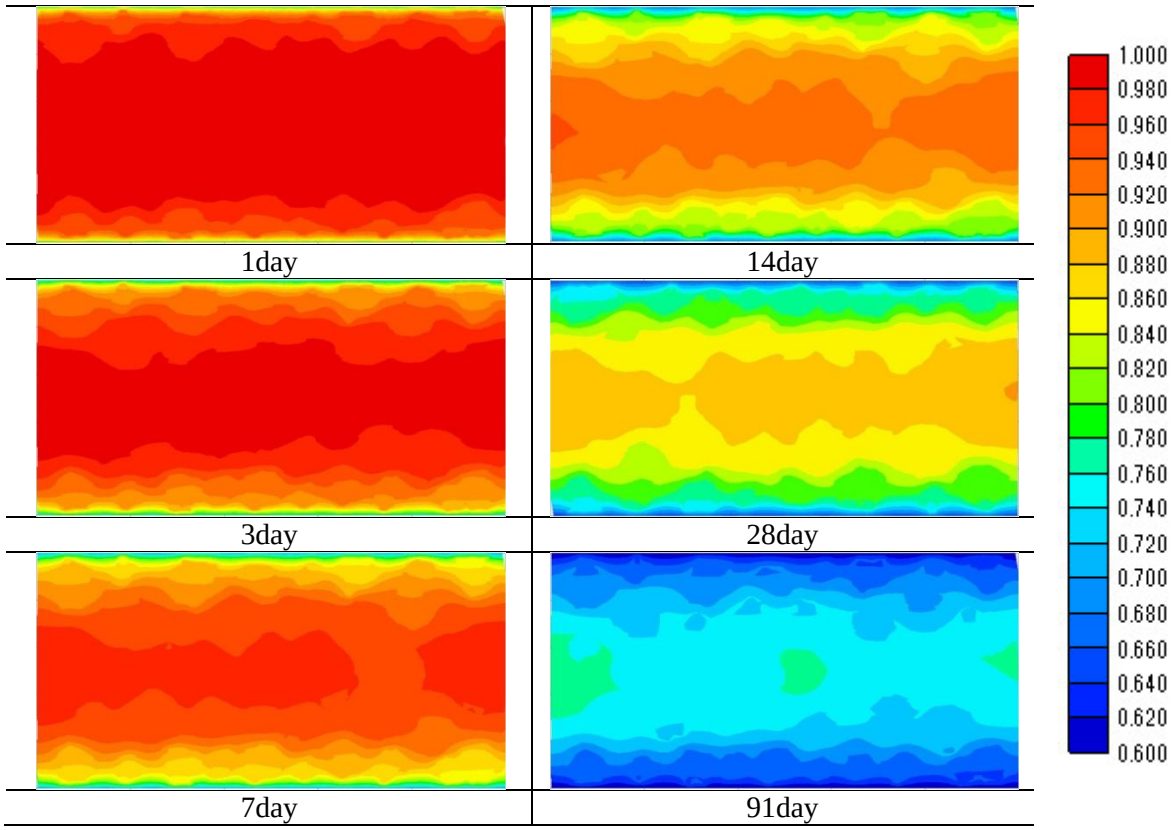

Fig. 5.20 Contour plots of the specimen as a function of equilibrium relative humidity.

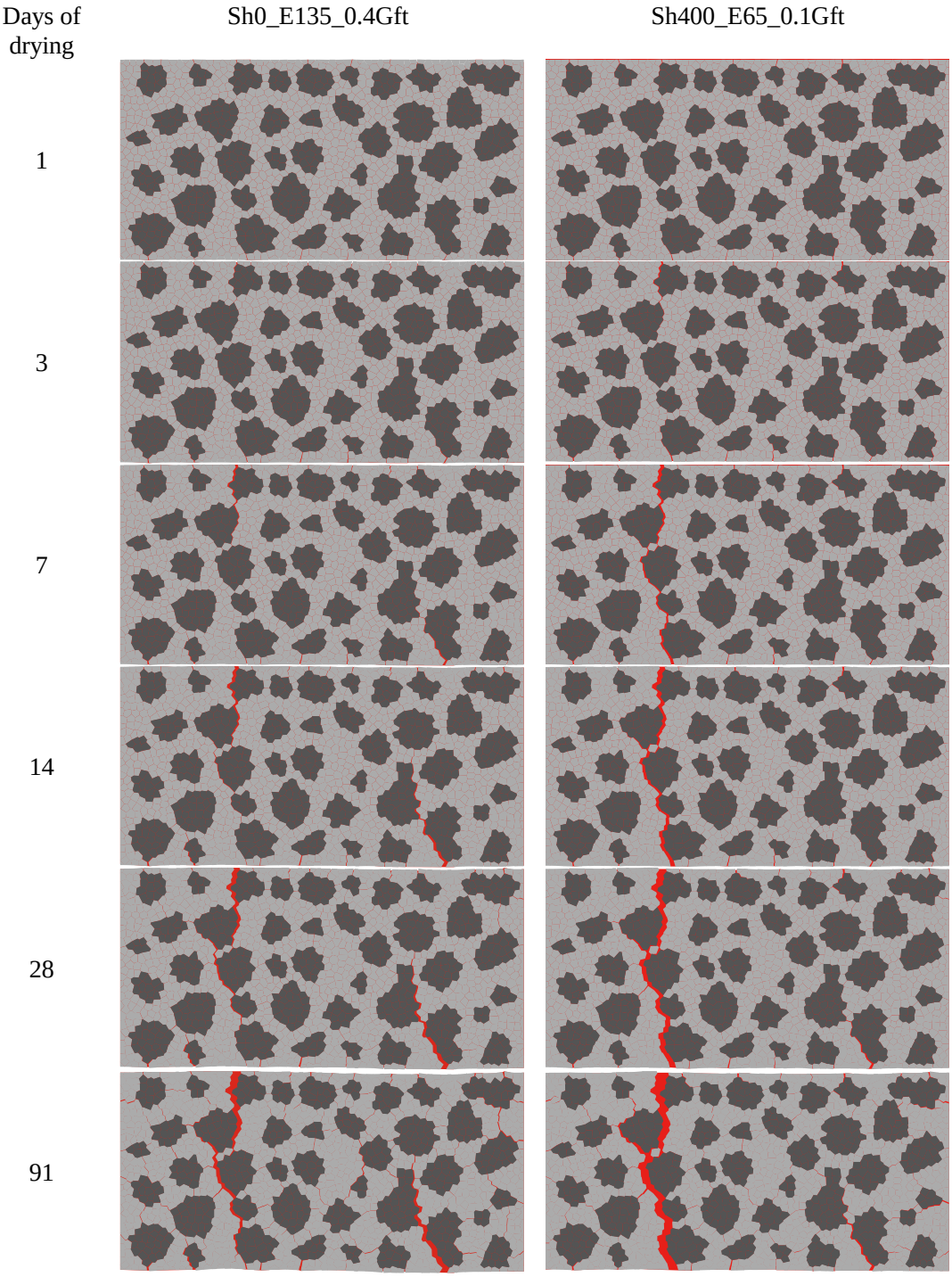

Fig. 5.21 Calculation results of Sh0_E135_0.4Gft and Sh400_E65_0.1Gft at different ages during drying. The width of the red line is linearly proportional to the tensile strain of normal spring. The magnification is 40×.

5.4.4.2 Cracking behavior

(1) Reproduction of the experimental trends

Fig. 5.21 represents the time-dependent cracking behavior under drying of Sh0_E135_0.4Gft and Sh400_E65_0.1Gft. No cracking was observed until the first day of drying. Three days after drying,

several fine cracks were observed on the top and bottom edges of the specimens. In the case of Sh400_E65_0.1Gft, a surface crack propagated along the aggregate surfaces, and a relatively large crack was observed on the upper-left part while many cracks stayed near aggregates in the case of Sh0_E135_0.4Gft. These observations can be explained by the large shrinkage of the aggregate and the small fracture energy of the ITZ. Seven days after drying, Sh0_E135_0.4Gft exhibited a crack distribution with one growing from the top left, and the other growing from the bottom right. On the other hand, Sh400_E65_0.1Gft showed a through-crack. This can also be explained by the large shrinkage of the aggregate and the small fracture energy of the ITZ. A large aggregate shrinkage enhances crack propagation along the aggregates since they shrink during the drying process and a larger stress becomes localized on the surface of the aggregates. This tensile stress promotes crack propagation along the crack surface. Furthermore, the smaller fracture energy of the ITZ means that crack propagation reduces the fraction of the concrete specimen that can bear the total shrinkage-induced stress produced by a restraining body. Therefore, cracks can easily grow under restraint conditions at their front. Thus, the smaller fracture energy of the ITZ has an impact on the localization of cracking.

The cracking pattern in concrete is determined by both fine cracks bridging aggregates and wide cracks propagating and connecting the ITZ zones of aggregates. This is similar to the phenomena observed in Section 5.3.2. In the crack pattern present after 91 days of drying, crack localization is very intense in the case of Sh400_E65_0.1Gft. The close-up figures (Fig. 5.22) confirm wider small cracks around the aggregate in the case of Sh0_E135_0.4Gft. These results imply that Sh0_E135_0.4Gft transformed the elastic energy accumulated by restraining of shrinkage into multiple fine cracks around the aggregate, while Sh400_E65_0.1Gft did so by localizing one large through-crack. These modeled tendencies reproduced the experimental results in Section 5.3.2. In the next section, the contribution of each parameter to crack localization is discussed.

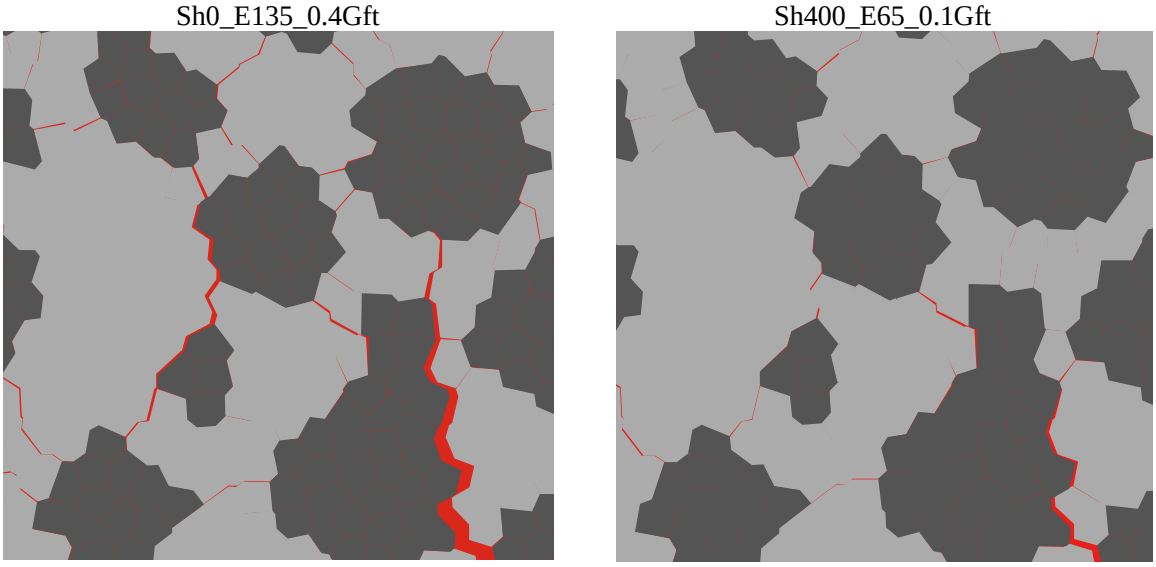

Fig. 5.22 Close-up of the cracking pattern around the aggregate at 91 days of drying in the calculation results of Sh0_E135_0.4Gft and Sh400_E65_0.1Gft.

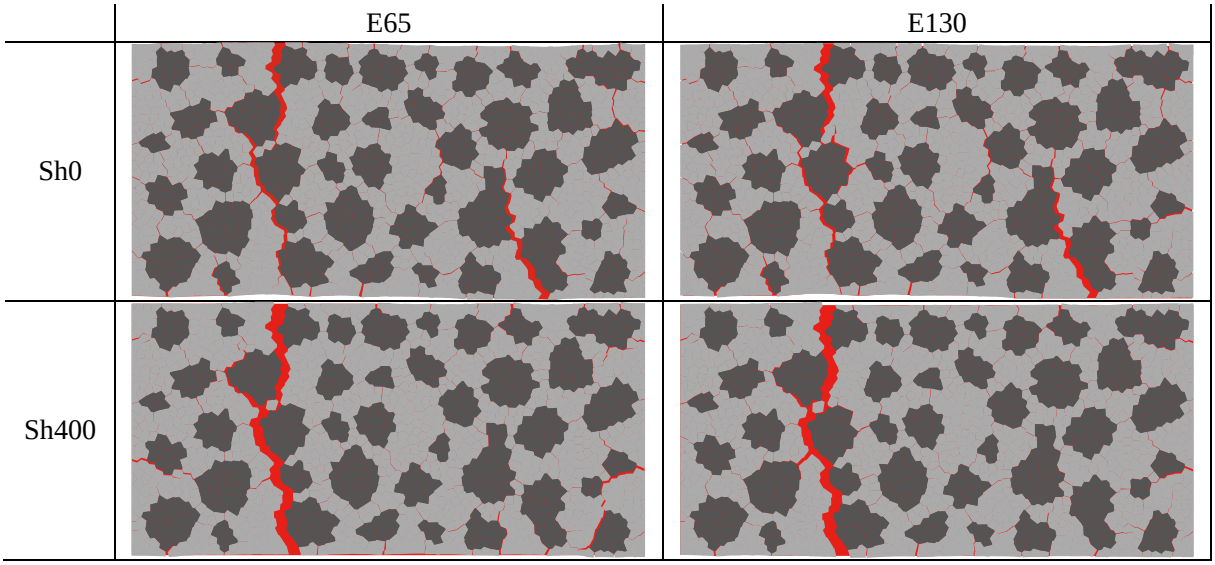

Fig. 5.23 Impact of shrinkage and Young's modulus of the aggregate on crack patterns in concretes. Sh0 and Sh400 depict aggregates having shrinkages of 0 and 400 microns, respectively. E65 and E130 depict aggregates having Young's modulus of 65 and 130 GPa, respectively.

(2) Impact of individual parameters

Fig. 5.23 shows cracking behaviors after 91 days of drying, as affected by differences in Young's modulus and aggregate shrinkage. In this figure, the Young's modulus of the aggregate had little effect on the cracking pattern in concrete under restraint conditions. This can be explained by the fact that almost all the mortar was under the tension field in the X-direction, and the restraining role of the aggregate for mortar shrinkage did not have a large impact in contrast to the case of free shrinkage [78].

On the contrary, the shrinkage of the aggregate had a large impact on cracking behavior in concrete. In the case where the aggregate showed low shrinkage, small cracks were distributed around the aggregate while the concrete containing an aggregate with large shrinkage exhibited one large crack. Thus, the more similar the aggregate and mortar were in terms of their shrinkage properties, the greater was the localization of cracking in concrete under restraint conditions.

Fig. 5.24 shows the impact of the tensile strength and Young's modulus of the ITZ on the cracking pattern. Large cracks appeared in a different position for the Sh0_0.75E_0.5f_t condition. The results indicated that if we increase the tensile strength of ITZ with constant fracture energy, localization of cracking is confirmed.

In Fig. 5.25, cracking patterns in concrete as affected by the fracture energy of the ITZ are shown. During the crack development of cracking, initial crack patterns among SH0_0.1Gft, Sh0_0.2Gft, and Sh0_0.4Gft were similar almost the same until they were dried for 1 day, because the mesh geometry is common. However, after 1 day of drying, the cracks developed differently. The smaller the fracture energy was, the more localized and wider the cracks were. The difference in cracking patterns was largest between Sh0_0.1Gft and Sh0_0.2Gft.

Crack distribution evaluated quantitatively is shown in Fig. 5.26. It shows the frequency of springs assorted by crack widths in a logarithmic scale. Fig. 5.26(a) shows the crack distribution for aggregates with different shrinkages, Fig. 5.26(b) shows that for different strength of ITZ, and Fig. 5.26(c) shows the crack distribution for different fracture energies of the ITZ. In Fig. 5.26(a), the concrete with a smaller aggregate shrinkage value shows a high frequency of cracks with widths ranging from 0.001 mm to 0.01 mm while large cracks of the order of 0.1 mm show a low frequency. Thus, smaller aggregate shrinkage apparently distributes energy into small cracks of the order of 0.01 mm~ 0.001 mm in width by way of compensation for cracks of the order of 0.1 mm in width. The same trend was observed in the cases of Sh0-0.1Gft and Sh0-0.2Gft.

These analytical studies confirmed that the localization of cracking becomes increasingly apparent when aggregate shrinkage is larger, strength of ITZ is larger, or the fracture energy of the ITZ is smaller.

As discussed in the earlier sections, aggregate type has a large impact on the properties of the ITZ and aggregate shrinkage that governs shrinkage-induced cracking in concrete under restraint conditions. Consequently, it can be concluded that the coarse aggregate of pure limestone, which shows smaller drying shrinkage and may densify the ITZ, can reduce the number of visible cracks in concrete under restraint conditions. This is since it allows fine cracks around the coarse aggregate that absorb the localization of cracking.

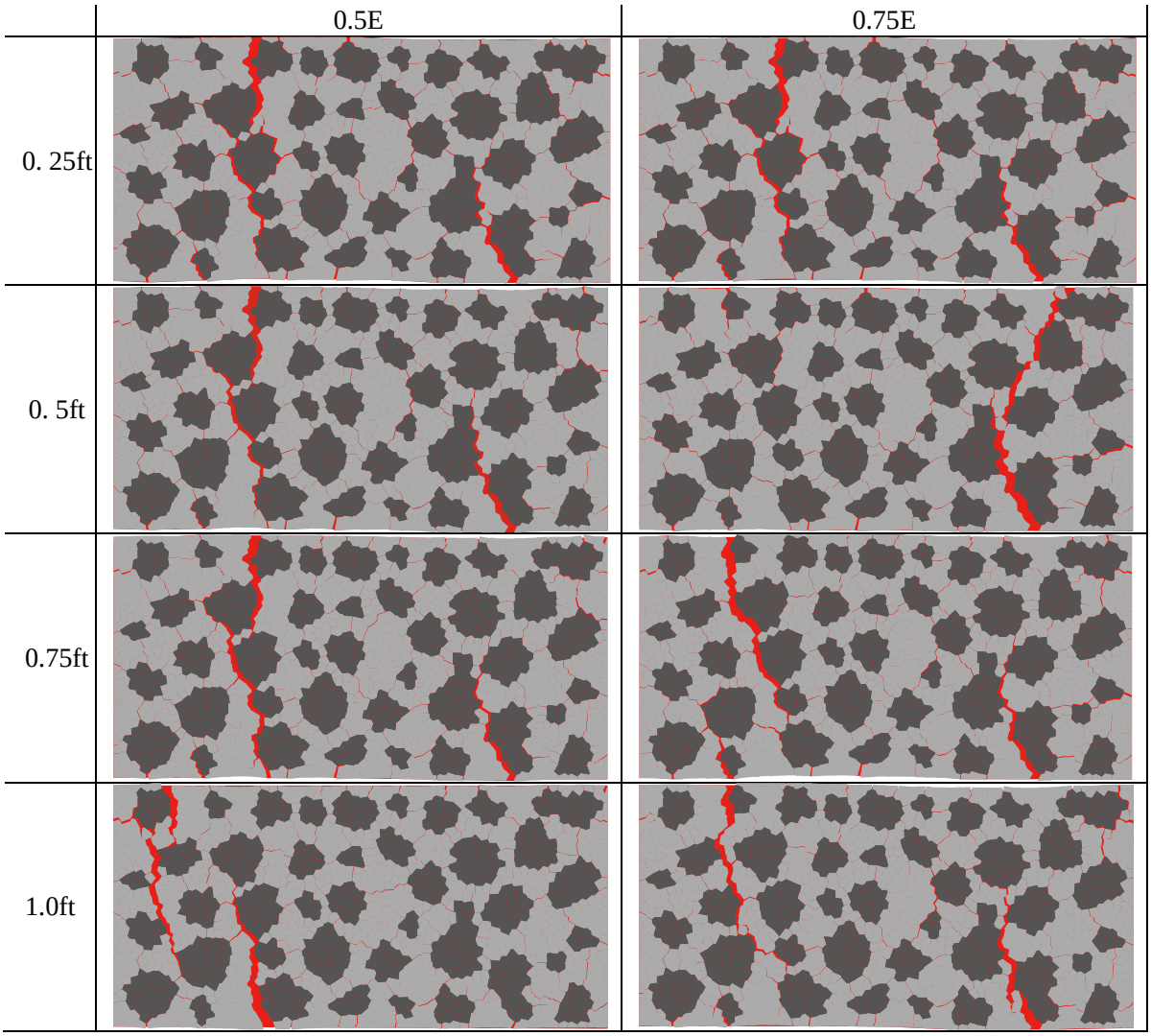

Fig. 5.24 Impact of strength and Young's modulus of the ITZ on crack patterns in concretes.
0.5*E* and 0.75*E* represent the Young's modulus of the ITZ, which equate to 0.5 and 0.75 times the Young's modulus of mortar. 0.25, 0.5f_t, 0.75 f_t, and 1.0 f_t represent the strength of the ITZ, which equate to 0.25, 0.5, 0.75, and 1.0 times the strength of mortar.

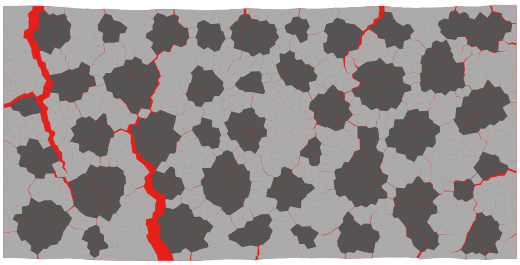

Sh0_0.1Gft

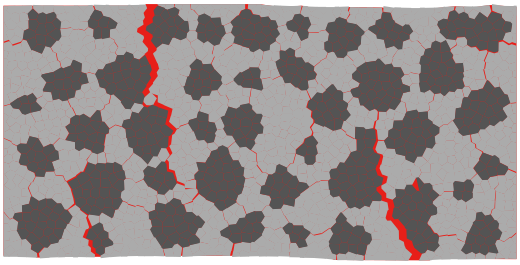

Sh0_0.2Gft

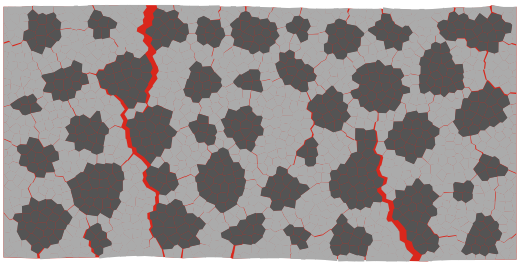

Sh0_0.4Gft

Fig. 5.25 Impact of fracture energy of ITZ on crack patterns in concretes.

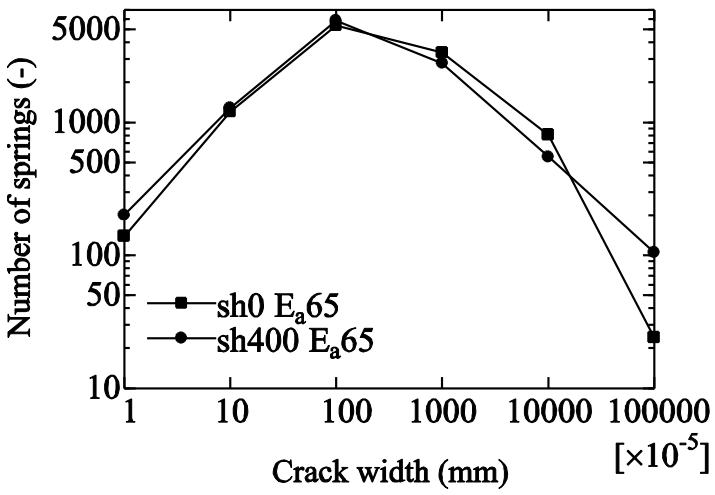

(a) Impact of aggregate shrinkage

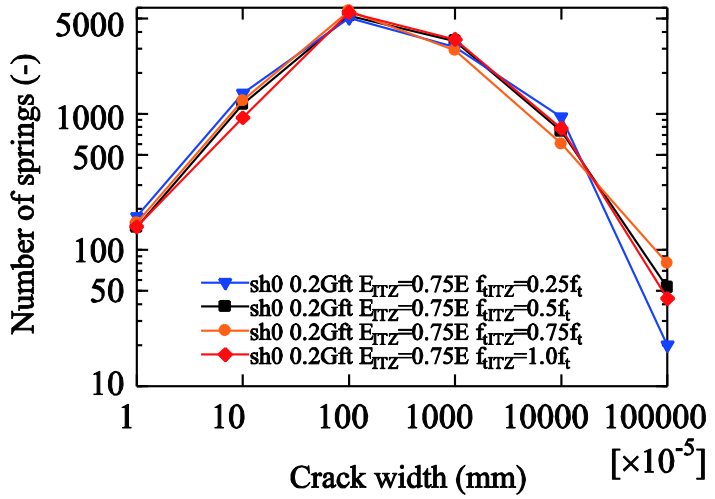

(b) Impact of strength of ITZ

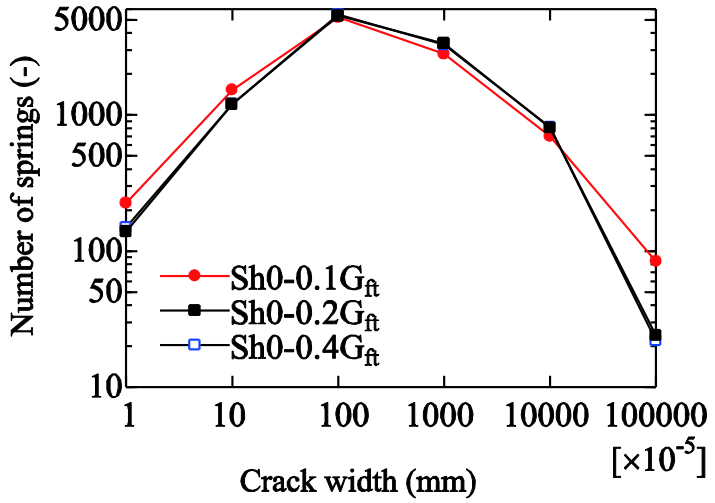

(c) Impact of fracture energy of ITZ

Fig. 5.26 Crack distribution affected by (a) aggregate shrinkage and (b) fracture energy of ITZ.

5 Summary

Concrete specimens with aggregates having different properties including drying shrinkage were prepared and a water-impermeable coating was applied to control the drying direction. Changes in the shrinkage strain distribution of the cross-section of the specimen perpendicular to the drying direction were observed with a digital image correlation method (DICM) under restricted and unrestrained conditions.

The drying shrinkage of the aggregate was found to play a dominant role in determining the drying shrinkage of concrete. Under unrestrained conditions, the DICM confirmed that when limestone aggregates with a small drying shrinkage were used, the difference in the drying shrinkage between the aggregate and the mortar caused cracks around the aggregate, forming shrinkage strain gradients from the drying surface to the inside. This tendency was small when sandstone aggregates with a large drying shrinkage were used. This was partly due to the porosity of the sandstone aggregate, which allowed it to release excessive water to suppress drying shrinkage during the early stages of drying.

Under restrained conditions, specimens with the limestone aggregate showed discontinuous fine cracks developing both at the surface and into the interiors. Meanwhile, for specimens with the sandstone aggregate, fine cracks were distributed over the surface while a single large crack extended inside with time.

With the aid of numerical analysis, parameters that could contribute to cracking behavior in concrete, such as the Young's modulus and aggregate shrinkage, strength, stiffness, and fracture energy of the ITZ, were studied. Aggregate shrinkage and the fracture energy of the ITZ were found to govern shrinkage-induced cracking of concrete under restraint conditions.

Based on both the experimental and numerical analysis results, it can be concluded that when the difference in drying shrinkage between the aggregate and mortar is considerable, or the fracture energy of the interfacial transition zone (ITZ) is very large, the distribution of fine cracks contributes to the suppression of macroscopic cracks. However, when the difference is small or the fracture energy is small, the development of a single large crack, promoted by the associated drying progression, becomes significant. This consequently leads to the formation of a localized macroscopic crack. Pure limestone, which shows smaller drying shrinkage and may densify the ITZ in concrete under restraint conditions, allows fine cracks to form around coarse aggregate particles that absorb stress and limit crack localization, and thus control macroscopic cracks.

References

1 T.C. Powers, The mechanics of shrinkage and reversible creep of hardened cement paste, in: C.a.C. Association (Ed.) International Conference on the structure of Concrete, London, 1965, pp. 319–344.

2 R.A. Helmuth, D.H. Turk, The Reversible and Irreversible Drying Shrinkage of Hardened Portland Cement and Tricalcium Silicate Pastes, Journal of the PCA Research and Development Laboratories, 9 (1967) 8 - 21.

3 R.F. Feldman, P.J. Sereda, A model for hydrated Portland cement paste as deduced from sorption-length change and mechanical properties, Mat Constr, 1 (1968) 509-520.

4 F.H. Wittmann, Surface tension skrinkage and strength of hardened cement paste, Mat Constr, 1 (1968) 547-552.

5 Z.P. Bažant, Thermodynamics of hindered adsorption and its implications for hardened cement paste and concrete, Cement and Concrete Research, 2 (1972) 1-16.

6 T. Sato, T. Goto, K. Sakai, Mechanism for reducing drying shrinkage of hardened cement by organic additives, CAJ Rev, (1983) 52-54.

7 W. Hansen, Drying Shrinkage Mechanisms in Portland Cement Paste, Journal of the American Ceramic Society, 70 (1987) 323-328.

8 J.J. Beaudoin, L. Raki, R. Alizadeh, L. Mitchell, Dimensional change and elastic behavior of layered silicates and Portland cement paste, Cement and Concrete Composites, 32 (2010) 25-33.

9 I. Maruyama, Origin of Drying Shrinkage of Hardened Cement Paste: Hydration Pressure, Journal of Advanced Concrete Technology, 8 (2010) 187-200.

10 F.M. Lea, Cement Research: Retrospect and Prospect, in: Chemistry of Cement, Proceedings of The Forth International Smposium, Washington D.C., 1962, pp. 5-8.

11 R.W. Carlson, DRYING SHRINKAGE OF CONCRETE AS AFFECTED BY MANY FACTORS, American Society Testing & Materials Proceedings, 38 (1938) 419-437.

12 G. Pickett, Effect of Aggregate on Shrinkage of Concrete and a Hypothesis Concerning Shrinkage, ACI Journal proceedings, 52 (1956) 581-590.

13 O. Ishai, Influence of Sand Concentration on Deformations of Mortar Beams Under Low Stresses, ACI Journal, 58 (1961) 611-624.

14 T.C. Hansen, K.E.C. Nielsen, Influence of Aggregate Properties on Concrete Shrinkage, ACI Journal, 62 (1965) 789-794.

15 D.W. Hobbs, Influence of Aggregate Restraint on the Shrinkage of Concrete, ACI Journal, 71 (1974) 445-450.

16 R.W. Burrows, The Visible and Invisible Cracking of Concrete, Amer Concrete Inst, Farmington Hills, Mich., 1998.

17 B. Bissonnette, P. Pierre, M. Pigeon, Influence of key parameters on drying shrinkage of cementitious materials, Cement and Concrete Research, 29 (1999) 1655-1662.

18 P. Grassl, H.S. Wong, N.R. Buenfeld, Influence of aggregate size and volume fraction on shrinkage

induced micro-cracking of concrete and mortar, Cement and Concrete Research, 40 (2010) 85-93.

19 F. Lagier, X. Jourdain, C. De Sa, F. Benboudjema, J.B. Colliat, Numerical strategies for prediction of drying cracks in heterogeneous materials: Comparison upon experimental results, Engineering Structures, 33 (2011) 920-931.

20 W. Zhang, M. Zakaria, Y. Hama, Influence of aggregate materials characteristics on the drying shrinkage properties of mortar and concrete, Construction and Building Materials, 49 (2013) 500-510.

21 R.W. Carlson, Drying Shrinkage Of Large Concrete Members, ACI Journal, 33 (1937) 327-336.

22 J.A. Almudaiheem, W. Hansen, Effect of Specimen Size and Shape on Drying Shrinkage of Concrete, ACI Materials Journal, 84 (1987) 130-135.

23 L. Granger, J.M. Torrenti, P. Acker, Thoughts about drying shrinkage: Scale effects and modelling, Mater Struct, 30 (1997) 96-105.

24 Z.P. Bažant, L.J. Najjar, Nonlinear water diffusion in nonsaturated concrete, Mat Constr, 5 (1972) 3-20.

25 L.-O. Nilsson, Hygroscopic moisture in concrete - drying, measurements & related material properties, in: TVBM 1003, Lund university, 1980.

26 K. Sakata, A study on moisture diffusion in drying and drying shrinkage of concrete, Cement and Concrete Research, 13 (1983) 216-224.

27 H. Akita, T. Fujiwara, Y. Ozaka, A practical procedure for the analysis ofmoisture transfer within concrete due to drying, Magazine of Concrete Research, 49 (1997) 129-137.

28 T. Shimomura, K. Maekawa, Analysis of the drying shrinkage behaviour of concrete using a micromechanical model based on the micropore structure of concrete*, Magazine of Concrete Research, 49 (1997) 303-322.

29 V. Baroghel-Bouny, M. Mainguy, T. Lassabatere, O. Coussy, Characterization and identification of equilibrium and transfer moisture properties for ordinary and high-performance cementitious materials, Cement and Concrete Research, 29 (1999) 1225-1238.

30 T. Ayano, F.H. Wittmann, Drying, moisture distribution, and shrinkage of cement-based materials, Mater Struct, 35 (2002) 134-140.

31 M. Azenha, K. Maekawa, T. Ishida, R. Faria, Drying induced moisture losses from mortar to the environment. Part I: experimental research, Mater Struct, 40 (2007) 801-811.

32 J. Zhang, D. Hou, Y. Gao, S. Wei, Determination of Moisture Diffusion Coefficient of Concrete at Early Age from Interior Humidity Measurements, Drying Technology, 29 (2011) 689-696.

33 Comité Euro-International du Béton, CEB-FIP Model Code 1990, in, Thomas Telford Ltd, 1993.

34 AIJ, Recommendations for Practice of Crack Control in Reinforced Concrete Buildings (Design and Construction), in, Maruzen Co. Ltd., 2006.

35 G.F. Kheder, R.S.A. Rawi, J.K.A. Dhahi, Study of the Behavior of Volume Change Cracking in Base-Restraint Concrete Walls, ACI Materials Journal, 91 (1994) 150-157.

36 H.T. See, E.K. Attiogbe, M.A. Miltenberger, Shrinkage Cracking Characteristics of Concrete Using Ring Specimens, ACI Materials Journal, 100 (2003) 239-245.

37 R.W. Carlson, T.J. Reading, Model Study of Shrinkage Cracking in Concrete Building Walls, ACI Structural Journal, 85 (1988) 395-404.

38 R. Bloom, A. Bentur, Free and Restrained Shrinkage of Normal and High-Strength Concretes, ACI Materials Journal, 92 (1995) 211-217.

39 K. Kovler, A. Bentur, Cracking Sensitivity of Normal- and High-Strength Concretes, ACI Materials Jounral, 106 (2009) 537-542.

40 S.P. Shah, C. Ouyang, S. Marikunte, W. Yang, E. Becq-Giraudon, A Method to Predict Shrinkage Cracking of Concrete, ACI Materials Journal, 95 (1998) 339-346.

41 Y. Mitani, M. Tanimura, I. Maruyama, Shrinkage cracking characteristics of concrete using shrinkage reducing agent, in: AIJ (Ed.) Summaries of technical papers of annual meeting, Sapporo, Japan, 2013, pp. 41-42.

42 Y. Mitani, Y. Ishii, M. Tanimura, I. Maruyama, Quantitative evaluation on reduction effect of drying shrinkage cracks by expansive additive, in: AIJ (Ed.) Summaries of technical papers of annual meeting, Nagoya, Japan, 2012, pp. 747-748.

43 J.-H. Moon, F. Rajabipour, B.J. Pease, J. Weiss, Autogenous shrinkage, residual stress, and cracking in cementitious composites: The influence of internal and external restraint, in: B. Persson, D. Bentz (Eds.) Fourth International Seminar on Self-desiccation and Its Importance in Concrete Technolog, Lund University, Washington D. C., USA, 2005, pp. 1-20.

44 I. Maruyama, H. Sasano, Strain and crack distribution in concrete during drying, Mater Struct, 47 (2014) 517-532.

45 A. Idiart, C. López, I. Carol, Modeling of drying shrinkage of concrete specimens at the meso-level, Mater Struct, 44 (2011) 415-435.

46 C. López, I. Carol, A. Aguado, Meso-structural study of concrete fracture using interface elements. II: compression, biaxial and Brazilian test, Mater Struct, 41 (2008) 601-620.

47 T. Kawai, New discrete models and their application to seismic response analysis of structures, Nuclear Engineering and Design, 48 (1978) 207-229.

48 J.E. Bolander Jr, S. Saito, Fracture analyses using spring networks with random geometry, Engineering Fracture Mechanics, 61 (1998) 569-591.

49 H. Nakamura, W. Srisoros, R. Yashiro, M. Kunieda, Time-Dependent Structural Analysis Considering Mass Transfer to Evaluate Deterioration Process of RC Structures, Journal of Advanced Concrete Technology, 4 (2006) 147-158.

50 I. Maruyama, H. Sasano, Y. Nishioka, G. Igarashi, Strength and Young's modulus change in concrete due to long-term drying and heating up to 90 ℃, Cement and Concrete Research, 66 (2014) 48-63.

51 G. Simmons, W.F. Brace, Comparison of static and dynamic measurements of compressibility of rocks, Journal of Geophysical Research, 70 (1965) 5649-5656.

52 C. Neubauer, H. Jennings, E. Garboczi, A three-phase model of the elastic and shrinkage properties of mortar, Advanced Cement Based Materials, 4 (1996) 6-20.

53 I. Maruyama, A. Sugie, Numerical Study on Drying Shrinkage of Concrete Affected by Aggregate

Size, Journal of Advanced Concrete Technology, 12 (2014) 279-288.

54 P. Trtik, B. Münch, W.J. Weiss, A. Kaestner, I. Jerjen, L. Josic, E. Lehmann, P. Lura, Release of internal curing water from lightweight aggregates in cement paste investigated by neutron and X-ray tomography, Nuclear Instruments and Methods in Physics Research Section A: Accelerators, Spectrometers, Detectors and Associated Equipment, 651 (2011) 244-249.

55 I. Maruyama, M. Kanematsu, T. Noguchi, H. Iikura, A. Teramoto, H. Hayano, Evaluation of water transfer from saturated lightweight aggregate to cement paste matrix by neutron radiography, Nuclear Instruments and Methods in Physics Research Section A: Accelerators, Spectrometers, Detectors and Associated Equipment, 605 (2009) 159-162.

56 X. Ping, J.J. Beaudoin, Effects of transition zone microstructure on bond strength of aggregate-portland cement paste interfaces, Cement and Concrete Research, 22 (1992) 23-26.

57 P.J.M. Monteiro, P.K. Mehta, Interaction between carbonate rock and cement paste, Cement and Concrete Research, 16 (1986) 127-134.

58 K. Rokugo, M. Iwasa, T. Suzuki, W. Koyanagi, Testing methods to determine tensile strain softening curve and fracture energy of concrete, in: Mihashi et al. (Ed.) Fracture Toughness and Fracture Energy, Balkema, The Netherlands, 1989, pp. 153-163.

59 Y. Yamamoto, H. Nakamura, I. Kuroda, N. Furuya, Analysis of compression failure of concrete by three dimensional regid body spring model, Doboku Gakkai Ronbunshuu E, 64 (2008) 612-630.

60 S. Saito, H. Hikosaka, Numerical analysis of reinforced concrete structures using spring network models, Doboku Gakkai Ronbunshu, 1999 (1999) 289-303.

61 G. Igarashi, I. Maruyama, Y. Nishioka, H. Yoshida, Influence of mineral composition of siliceous rock on its volume change, Construction and Building Materials, 94 (2015) 701-709.

62 N. Horiguchi, G. Igarashi, I. Maruyama, Fundamental study on volume change of aggregate due to loss of evaprable water (in Japanese), Proceedings of Japan Concrete Instituite, 33 (2011) 131-136.

63 J.P. Ollivier, J.C. Maso, B. Bourdette, Interfacial transition zone in concrete, Advanced Cement Based Materials, 2 (1995) 30-38.

64 K. Scrivener, A. Crumbie, P. Laugesen, The Interfacial Transition Zone (ITZ) Between Cement Paste and Aggregate in Concrete, Interface Science, 12 (2004) 411-421.

65 E. Herve, S. Care, J.P. Seguin, Influence of the porosity gradient in cement paste matrix on the mechanical behavior of mortar, Cement and Concrete Research, 40 (2010) 1060-1071.

66 A. Cwirzen, V. Penttala, Aggregate–cement paste transition zone properties affecting the salt–frost damage of high-performance concretes, Cement and Concrete Research, 35 (2005) 671-679.

67 D. Breton, A. Carles-Gibergues, G. Ballivy, J. Grandet, Contribution to the formation mechanism of the transition zone between rock-cement paste, Cement and Concrete Research, 23 (1993) 335-346.

68 K.L. Scrivener, E.M. Gartner, Microstructural Gradients in Cement Paste Around Aggregate Particles, Materials Research Society Symposium Proceedings, 114 (1988) 77-85.

69 B. Hearing, Fracture behavior of Mortar-Aggregate Interfaces in Concrete, in: Dept of Civil and Environmental Engineering, Massachusetts Institute of Technology, Boston, 1997.

70 K. Mitsui, Z. Li, D.A. Lange, S.P. Shah, Relationship Between Microstructure and Mechanical Properties of Paste-Aggregate Interface, ACI Materials Journal, 91 (1994) 30-39.

71 P. Xie, J.J. Beaudoin, R. Brousseau, Effect of aggregate size on transition zone properties at the portland cement paste interface, Cement and Concrete Research, 21 (1991) 999-1005.

72 M.G. Alexander, S. Mindess, S. Diamond, L. Qu, Properties of paste-rock interfaces and their influence on composite behaviour, Materials and Structures, 28 (1995) 497-506.

73 W.A. Tasong, C.J. Lynsdale, J.C. Cripps, Aggregate-cement paste interface: Part I. Influence of aggregate geochemistry, Cement and Concrete Research, 29 (1999) 1019-1025.

74 G.A. Rao, B.K. Raghu Prasad, Influence of type of aggregate and surface roughness on the interface fracture properties, Mater Struct, 37 (2004) 328-334.

75 J.E. Bolander Jr, S. Berton, Simulation of shrinkage induced cracking in cement composite overlays, Cement and Concrete Composites, 26 (2004) 861-871.

76 I. Maruyama, G. Igarashi, N. Kishi, Fundamental study on water transfer in portland cement paste, Journal of Structural and Construction Engineering (Transactions of AIJ), 76 (2011) 1737-1744.

77 I. Maruyama, N. Horiguchi, Tensile creep of hardened cement paste, in: J.C. Association (Ed.) 65th Annual conference on cement technology, Japan Cement Association, Tokyo, Japan, 2011, pp. 268-269.

78 J.W. Weiss, W. Yang, S. Shah., Shrinkage Cracking of Restrained Concrete Slabs, Journal of Engineering Mechanics, 124 (1998) 765-774.

Chapter 6 Conclusions

In this study, drying experiments of both mortar and concrete specimens have been done to evaluate water movement behaviour in cement based material. By comparing the results of drying experiments of mortar, concrete and cement paste specimens, one major conclusion was obtained: water diffusion coefficient is not greatly influenced by aggregate under the first drying condition. In other word, moisture transport behaviour is governed by harden cement paste. In addition to those aggregates impacts, temperature impact was also assessed. The results confirm that the temperature dependence of water diffusion coefficient is governed by power law. This work would aid the prediction of concrete properties. These key conclusions contribute to the prediction of rate of drying in concrete member. The numerical modelling which takes into account of colloidal nature of calcium silicate hydrate in Portland cement system is required.

The tensile strength of concrete, used as the cracking strength as well as to assess shear cracking strength, is one of the important parameters for aging control. This parameter is assessed by splitting tensile test. The mechanism of changes in splitting tensile strength of mortar and concrete using aggregate with different amounts of shrinkage under various drying conditions were experimentally studied. The specimens were dried until equilibrium at the constant temperature of 20 ℃ and humidity from 95% RH to 20% RH, and were also heated in a constant-temperature furnace at 40 ℃, 65 ℃, and 90 ℃, respectively. The coarse aggregate used in the experiment are limestone which is characterized by little shrinkage, and sandstone which is characterized by large shrinkage. The results elucidate that aggregate properties affect damage and strength development of concrete. Shrinkage properties of aggregate have large influence on the change of concrete properties under drying procedure. All concrete structures in ambient environment undergo drying process. Therefore, the change of concrete properties is inevitable. For long-term use of concrete structures, we have to take countermeasures to the changes of concrete properties under drying if it is required.

The alteration of concrete during drying composes of two parts. One is properties change of harden cement paste (hcp), and the other is micro-cracking caused by aggregate restraint. The changing trend of splitting tensile strength of concrete under various drying condition is strongly influenced by the strength trend of hcp. In addition to that, due to the inhomogeneous volume change of aggregate and mortar, under drying procedure, micro-cracking occurs around the aggregate. It has large influence on the change of splitting tensile strength. In the case of aggregate prone to high shrinkage with shrinkage behavior similar to that of mortar, there was less damage, and thus the decline in strength was smaller in the range from 80% RH to 20% RH. On the other hand, in the case of aggregate with low shrinkage, the decline in strength was higher in that range. Therefore, the shrinkage property of aggregate is really important for concrete. For the long time management of concrete structures, the knowledge of aggregate is needed, and then concrete properties change can be predicted afterwards.

It has been already reported that compressive strength and Young's modulus of concrete also changes under drying [1]. The mechanism of property change under drying is almost the same as that of splitting tensile strength, but the slight difference was observed with regards to compressive load-bearing pass in concrete. The micro-crack due to inhomogeneous shrinkage between aggregate and mortar cause the limitation of load-bearing pass under compressive load, especially in the range between 100% and 80% RH. And below this range, the drying has an influence on crack opening of micro-cracks around aggregates and will not change the load-bearing passes in concrete. Resultantly, change in nature of hardened cement paste directly affects on concrete property in compressive load condition, while such crack opening has large influence on stress concentration in tensile load condition. This mechanism is newly clarified in this dissertation.

When concrete shrinkage is restrained, visible or invisible cracking occurs. In this study, both experimental and numerical study of development of shrinkage-induced cracking under unrestrained and restrained condition had been done. The role of aggregate was focused on. Concrete specimens were prepared with the same mixture proportion except for their constituent coarse aggregates, namely limestone and sandstone that possess different inherent drying shrinkage values. The strain at a cross section perpendicular to the drying direction was observed using a digital image correlation method. Rigid-body-spring networks (RBSN) was applied to reproduce the trends of crack initiation and propagation behavior in order to understand the impact of aggregate properties on these processes. Truss networks model was used for moisture transfer.

The results of both experimental and numerical study on shrinkage-induced cracking in restrained concrete indicate that the fracture energy of interfacial transition zone (ITZ) has large influence on cracking behaviour. If hcp sticks strongly to the surface of aggregate, which is the case of limestone, numerous evenly distributed fine cracks on the surface of concrete are found. In the case of sandstone, there is small bonding between aggregate and mortar, namely there is smaller fracture energy of ITZ, it is easy for crack propagate on the surface of aggregate, and lead to crack opening, and it mitigate the stress accumulation in other regions. Therefore, additional cracks are not found on the surface of concrete. The shrinkage cracks are integrated and localized.

If the bonding on the interface between aggregate and hcp is strong, there are numerous minor surface cracks, and it leads to the reduction of Young's modulus of concrete. But the benefit in this case is that it reduces the possibility of occurrence of localized large cracking. This is the trade-off relationship. On the other hand, when aggregate shrink much and the surface bonding is less, there is slight smaller decrease in Young's modulus, and in restrained condition large visible cracking is found. In the case of concrete members, as cause of reduction of stiffness, the large visible cracking has larger impact than that of reduction in Young's modulus due to drying [2]. So the large shrinkage of aggregate and weak bond between aggregate and hcp is not good for structure performance. If we modify ITZ properties, we can change concrete properties as well.

The important phenomenon recently is that structure response against earthquake is changing due to drying even for nuclear power plant consisting of thick concrete walls. The stiffness decreased, then the natural frequency is also reduced during drying. The natural frequency change affects the seismic load of concrete structures. The base line trend of natural frequency is important to evaluate the damage due to seismic response. According to Ref [3], there are two possible reasons for natural frequency change of concrete structures under drying. One is decrease of Young's modulus of concrete, and the other is stiffness reduction of reinforced concrete members caused by shrinkage induced cracking. For long-term use of concrete structures, concrete properties change should be predicted. Otherwise, unexpected damage may happen under earthquake disaster.

Moisture transport is dominant phenomenon because it has large influence on the prediction of concrete properties. The results of water movement research in this study are important because it suggests how to predict the concrete structure properties change based on moisture movement. The results suggest that drying of the hardened cement paste is the key phenomenon. It is important to understand fully the drying rate of hardened cement paste. The numerical modelling which takes into accounts the obtained facts in this dissertaion will contributes to the aging management of concrete structures.

At the same time, it was found that there exist two major important aggregate properties for the change of concrete properties under drying. One is the shrinkage of aggregate, and the other is the fracture energy of ITZ. Both two properties are important for aging management of concrete structures. If such properties are obtained from existing structure, the possible degradation trend can be assessed. This new method of evaluating the existing structure is also one of the new proposals from this dissertation.

References

1 I. Maruyama, H. Sasano, Y. Nishioka and G. Igarashi. “Strength and Young's modulus change in concrete due to long-term drying and heating up to 90 ℃”, Cement and Concrete Research 66 (2014), 48-63.

2 A. Sugie, I. Maruyama and M. Teshigawara, “Numerical simulation for stiffness change of RC wall due to drying”, AIJ (Ed.) Summaries of technical papers of annual meeting, 2014, 1175-1176 (in Japanese).

3 I. Maruyama, “Multi-scale Review for Possible Mechanisms of Natural Frequency Change of Reinforced Concrete Structures under an Ordinary Drying Condition”, Journal of Advanced Concrete Technology, Vol. 14, 2016, 691-705.

Publications

Academic Publications

1) M. Lin, H. Sasano, I. Maruyama: Fundamental study on water diffusion coefficient of cement based material, Proceedings of Japan Concrete Institute, Vol. 35, No. 1, 2013, pp. 595-600

2) M. Lin, M. Itoh, I. Maruyama: Mechanism of change in splitting tensile strength of concrete during heating or drying up to 90^{o}C, Journal of Advanced Concrete Technology, Vol. 13, 2015, pp. 94-102

3) I. Maruyama, H. Sasano, M. Lin: Impact of aggregate properties on the development of shrinkage-induced cracking in concrete under restraint conditions, Cement and Concrete Research, Vol. 85, 2016, pp. 82-101

4) H. Sasano, M. Lin, I. Maruyama, Study on micro-cracking in concrete dried under high temperature, Proceedings of Japan Concrete Institute, Vol. 35, No. 1, 2013, pp. 703-708 (in Japanese).

Oral presentations

1) M. Lin, H. Sasano, I. Maruyama: Influence of curing temperature history and aggregate type on compressive strength development of concrete, AIJ (Ed.) Summaries of technical papers of annual meeting, Sapporo, Japan 2013, pp. 291-292

2) H. Sasano, M. Lin, I. Maruyama: Mechanical property of concrete under various humidity and temperature, AIJ (Ed.) Summaries of technical papers of annual meeting, Sapporo, Japan 2013, pp. 285-286 (in Japanese).

3) M. Itoh, H. Sasano, Y. Noshioka, M. Lin, I. Maruyama: Effect of cement paste strength on splitting tensile strength of concrete, AIJ (Ed.) Summaries of technical papers of annual meeting, Sapporo, Japan 2013, pp. 281-282 (in Japanese).

Acknowledgements

I would like to express my deep gratitude to my supervisor Professor MARUYAMA for his guidance on my doctoral study. He inspired me and offered me many valuable suggestions when I faced difficulties in my study. When I lost my confidence on my study, it is always him who continuously guides me to make progress in study. This work could not be accomplished without his guidance and help. I appreciate his patience, understanding and kindness. Thank you very much, MARUYAMA sensei. I will always memorize your favor for the rest of my life.

I would like to express my gratitude to Professor TESHIGAWARA and Professor MORI for their valuable suggestions and comments on my doctoral dissertation. I am also grateful to Hiroshi SASANO and Mitsuki ITOH for their assistance and helpful discussions in both my experimental and numerical work. I'd like to thank Masahiro KITAGUCHI for his introducing of experimental techniques. I also want to thank other members in Maruyama lab for providing me a good environment and a good team to work within.

Finally, my special gratitude goes to my parents. They keep supporting me, loving me, and patiently waiting for my accomplishment of doctoral study.

LIN, Mao

February, 2018